9

Computational Spectroscopy of the Transition State

DAVID C. CHATFIELD*, RONALD S. FRIEDMAN†, STEVEN L. MIELKE,
GILLIAN C. LYNCH, THOMAS C. ALLISON, and
DONALD G. TRUHLAR

University of Minnesota, Minneapolis, Minnesota

DAVID W. SCHWENKE

NASA Ames Research Center, Moffett Field, California

I. INTRODUCTION

In a typical chemical reaction the ability of the atoms to rearrange themselves is controlled by one or more dynamical bottlenecks in phase space. A dynamical bottleneck may be represented by a hypersurface in phase space dividing reactants from products, and this dividing surface is called the activated complex or the transition state (1). The allowed energy levels of the transition state are not strictly quantized because they are not bound states, but they are approximately quantized (like vibrationally predissociating states in spectroscopy (2) or like collision resonances in scattering theory (3–5)), because they are fleetingly metastable. The search for these quantized energy levels is called transition state spectroscopy. Transition state spectroscopy has proved to be extremely difficult from an experimental point of view, so much so, in fact, that the term has come to be associated with any form of spectroscopy or any spectroscopic measurement that gives information about the activated complex region of the potential energy surface, even when no hint of quantized structure is present (6,7). In recent years we have learned that this structure does exist and can be uncovered by quantum reactive scattering calculations (8–16). This chapter reviews the theory behind the phenomenon and surveys recent results from our group, some (those in Secs. IV, V, and VIII) published elsewhere (8–16) and others (extensive results in Secs. VI and VII and preliminary results in Sec. IX.D) presented for the first time in this chapter. The analysis of the O + H$_2$ system

*Current affiliation: Florida International University, Miami, Florida
†Current affiliation: Indiana University–Purdue University, Fort Wayne, Indiana

includes a contribution by Bowman (13), and our work on halogen-hydrogen halide reactions is based in part on accurate scattering calculations by Schatz (17–19). We also discuss results in computational and experimental transition state spectroscopy by other groups (references in Secs. IV–IX).

II. THEORY

We focus attention on bimolecular reactions of the form A + BC → AB + C. The canonical ensemble rate coefficient $k(T)$ in the expression

$$- \frac{d[A]}{dt} = k(T)[A][BC] \tag{1}$$

can be written in terms of the microcanonical ensemble rate constant $k(E)$, T being the temperature and E being the total energy, as (8,20)

$$k(T) = \frac{\int_0^\infty \exp(-E/k_BT)\rho^R(E)k(E) \, dE}{\Phi^R(T)} \tag{2}$$

where k_B is Boltzmann's constant, $\Phi^R(T)$ is the reactants' partition function per unit volume, and $\rho^R(E)$ is the reactants' density of states per unit volume per unit energy. An exact quantum mechanical expression for $k(E)$ is given in terms of the state-to-state reaction probabilities $P_{nn'}$ by (8,21)

$$k(E) = \frac{\Sigma_n \Sigma_{n'} \, P_{nn'}(E)}{h\rho^R(E)} \tag{3}$$

where h is Planck's constant and $n(n')$ is an index of the quantum state of the reactants (products), and we are employing the ultimate level of state specification, in which each channel is counted as a state. For an atom-diatom reaction, $n(n')$ designates the total angular momentum J, its component M_J on an arbitrary space-fixed axis, and the set of initial (final) vibrational quantum number v (v'), rotational quantum number j (j'), and orbital angular momentum quantum number l (l'). The state-to-state reaction probability can be written in terms of elements of the scattering matrix S if desired (22):

$$P_{nn'}(E) = |S_{nn'}(E)|^2 \tag{4}$$

The double sum in Eq. (3) contains all the dynamics in both $k(T)$ and $k(E)$ and is called the cumulative reaction probability (CRP) (23) and denoted $N(E)$:

$$N(E) = \sum_n \sum_{n'} P_{nn'}(E) \tag{5}$$

The dynamical structure in $k(E)$ can be brought out most clearly by calculating the energy derivative of the CRP, the density of reactive states $\rho(E)$:

$$\rho(E) = \frac{dN(E)}{dE} \tag{6}$$

Transition state theory (TST) provides a framework for understanding the CRP and its energy derivative. The transition state theory rate constant is the value that the rate constant would have if (i) all reactant states were in local Boltzmann equilibrium and (ii) the one-way flux through a hypersurface in phase space dividing reactants from products were equal to the flux from one side to the other (24–28). In a world described by classical mechanics, the latter condition would be true if all trajectories passing through the dividing surface crossed it only once. The dividing surface in phase space has one less degree of freedom than the phase space itself, and, as mentioned in the introduction, species constrained to the dividing surface are said to be in the transition state. The missing degree of freedom, which is normal to the dividing surface, is called the reaction coordinate s.

Conditions (i) and (ii), plus the usual assumption that bound degrees of freedom have quantized energy levels, lead to the familiar expression (1,29) in which the rate constant $k(T)$ becomes proportional to a "transition state partition function," $Q^{\ddagger}(T)$, which is a sum over quantized states of an activated complex:

$$k^{\ddagger}(T) = \frac{k_B T}{h} \frac{Q^{\ddagger}(T)}{\Phi^R(T)} e^{-V^{\ddagger}/k_B T} \qquad (7)$$

where $V^{\ddagger}$ is the classical potential energy at the transition state, i.e., the difference in the zeroes of energy used to compute $Q^{\ddagger}(T)$ and $\Phi^R(T)$. (Note that we take the zero of energy for partition functions to be the minimum potential energy of the species in question, *not* the lowest quantized energy level of that species.) The microcanonical ensemble version of the familiar TST expression is (30–33)

$$k^{\ddagger}(E) = \frac{N^{\ddagger}(E)}{h\rho^R(E)} \qquad (8)$$

Here $N^{\ddagger}(E)$ is the number of energy states (levels) of the activated complex with energy less than or equal to E.

If we interpret the quantization of the activated complex literally, then comparison of Eqs. (3), (5), and (8) suggests that the cumulative reaction probability will increase in steps of one at the energy levels of the transition state. However, Eq. (8) neglects quantum mechanical tunneling and nonclassical reflection (diffraction by the barrier top) at energies below and above, respectively, the reaction barrier. Furthermore, it assumes that the transition state is a perfect dynamical bottleneck in the sense that all systems crossing the transition state proceed directly from reactants to products without recrossing (24–28). Several workers have proposed generalizations of transition state theory to account for quantum tunneling and recrossing effects (21,23,34,35). For example, we can account for the breakdown of these assumptions in the simplest way by replacing Eq. (8) by

$$k^{\ddagger}(E) = \frac{\sum_{\tau} \kappa_{\tau} P_{\tau}(E)}{h\rho^T(E)} \qquad (9)$$

where τ is a level of the transition state, κ_{τ} is a transmission coefficient accounting for recrossing, and P_{τ} is a quantal or semiclassical transmission probability accounting for quantum mechanical tunneling and nonclassical reflection. The numerator still contains a sum over energy levels, but instead of increasing in steps of one at each new level of the transition state, it increases more gradually and by an amount governed by $\kappa_{\tau} P_{\tau}(E)$.

Note that if we set κ_τ equal to unity and $P_\tau(E)$ to a unit step function at transition state energy level E_τ, Eq. (9) reduces to (8).

If we assume that the reaction coordinate is separable, that there exists an effective potential curve $V_\tau(s)$ for passage through the transition state region in level τ, and that this potential has a parabolic form, we obtain $\kappa_\tau = 1$ and a simple form for $P_\tau(E)$. In particular, if $V_\tau(s)$ is given in terms of the reaction coordinate s by

$$V_\tau(s) = E_\tau + \frac{1}{2} k_\tau s^2 \tag{10}$$

with E_τ being the energy of the barrier maximum and k_τ being a negative force constant, then the quantum mechanical transmission probability is given by (36)

$$P_\tau(E) = \frac{1}{1 + \exp[(E_\tau - E)/W_\tau]} \tag{11}$$

where W_τ is a width parameter. The transmission probability $P_\tau(E)$ rises smoothly from zero to one. In Eq. (11), the width parameter W_τ is

$$W_\tau = \frac{\hbar |\omega_\tau|}{2\pi} \tag{12}$$

where $\hbar$ is Planck's constant divided by 2π, ω_τ is the imaginary frequency of the barrier

$$\omega_\tau = \sqrt{k_\tau/\mu} \tag{13}$$

and μ is the reduced mass. Because of Eqs. (12) and (13), W_τ is inversely related to the width of the effective potential barrier V_τ. Small values of W_τ correspond to wide barriers, for which tunneling and nonclassical reflection are less important. Inserting Eq. (11) into (9) leads to a generalized version of conventional transition state theory that incorporates quantum effects on reaction-coordinate motion and recrossing.

Equations (6), (8), (9), and (11) yield the following approximation to the density of reactive states:

$$\rho^\ddagger(E) = \sum_\tau \kappa_\tau \rho_\tau(E) \tag{14}$$

with

$$\rho_\tau(E) = \frac{\exp[(E_\tau - E)/W_\tau]}{W_\tau(1 + \exp[(E_\tau - E)/W_\tau])^2} \tag{15}$$

The function $\rho_\tau(E)$ is a symmetric bell-shaped curve centered at E_τ, and $\rho_\tau(E)$ is narrower when the effective potential barrier is wider. For an ideal dynamical bottleneck κ_τ is unity; deviations from unity indicate that recrossing or other multidimensional effects are important.

The density of reactive states $\rho(E)$ defined by Eq. (6) is the quantum mechanical analogue of the transition state theory $\rho^\ddagger(E)$ of Eq. (14). Transition state theory with quantum effects on the reaction coordinate motion and recrossing predicts that the CRP will increase in smooth steps of height κ_τ at each energy level of the transition state and that $\rho(E)$ will be a sum of bell-shaped curves, each centered at an energy E. We have found clear evidence for this prediction in the densities of reactive states $\rho(E)$ that we have calculated by accurate quantum dynamics.

Because the total angular momentum and its component are conserved during a collision, we can study the reaction dynamics for each value of J and M_J independently. Since the results are independent of M_J, we always set $M_J = 0$, and we will not mention it again (but the existence of the M_J quantum number is the reason for the factor of $2J + 1$ in the following sentence). In particular, we can study the J-specific contributions to the rate constant, $k^J(E)$ [with $k(E)$ of Eq. (3) being a $(2J + 1)$-weighted sum of individual $k^J(E)$], to the cumulative reaction probability, $N^J(E)$, and to the density of reactive states, $\rho^J(E)$. The influence of quantized transition states on chemical reactivity will be analyzed through studies of $k^J(E)$.

We can often understand the dynamics in greater detail by studying J-specific state-selected reaction probabilities $P_n^J(E)$, which are related to J-specific state-to-state reaction probabilities via

$$P_n^J(E) = \sum_{n'} P_{nn'}^J(E) \tag{16}$$

We also find it useful to define the corresponding densities of state-selected reaction probability $\rho_n^J(E)$:

$$\rho_n^J(E) = \frac{dP_n^J(E)}{dE} \tag{17}$$

A similar analysis can be made in terms of product states n' rather than initial states n:

$$P_{\to n'}^J(E) = \sum_{n} P_{nn'}^J(E) \tag{18}$$

$$\rho_{\to n'}^J(E) = \frac{dP_{\to n'}^J(E)}{dE} \tag{19}$$

The quantities $\rho_n^J(E)$ and $\rho_{\to n'}^J(E)$ are often helpful in discerning aspects of the reaction dynamics that are not apparent from $\rho^J(E)$.

We will also find it useful to present densities that result from taking the energy derivative of sums of other subsets of the state-to-state reaction probabilities. Parity-specific densities can be obtained from the derivative of the sum of $P_{nn'}$ having the same parity $P = (-1)^{j+l}$. (When $J = 0$, $j = l$, and so $P = +1$.) Furthermore, for atom-diatom reactions of the form $A + H_2 \to AH + H$, we can define a spatial permutation symmetry S, which equals $+1$ for *para* hydrogen and -1 for *ortho* hydrogen. Symmetry-specific densities are obtained by summing those $P_{nn'}$ with the same spatial permutation symmetry. Densities for a specific set (J, P, S) are denoted ρ^{JPS}; when these are summed over P and S, the above densities ρ^J are obtained.

For $H + H_2$ and $O + H_2$, the densities and CRPs to be presented result from treating the two hydrogen atoms in the initial molecule as distinguishable and presenting results for one of the two symmetry-related paths, for example, $A + H'H'' \to AH' + H''$. That is, we do not include the factor of 2 for the two products $AH' + H''$ and $AH'' + H'$. We do, however, sum over S, but ignoring nuclear spin. For $D + H_2$ and $F + H_2$, we present results for only a single symmetry S but count both product arrangements. In either of these cases, the CRP increases by about 1 at the nearly ideal transition states.

In order to separate contributions to the density of reactive states from events occurring on different time scales it is useful to introduce low-resolution convolutions of

the accurate density of reactive states. In particular we define

$$N^J(E; F) = \int_{E_i}^{E_f} dE' \, N^J(E') f(E, E'; F)$$ (20)

where the resolution function f is

$$f(E, E'; F) = A \, \exp\left\{ -\left[\frac{2(E - E')}{F}\right]^2 \ln 2 \right\}$$ (21)

and where the normalization factor A is determined by

$$A = \left(\int_{E_i}^{E_f} dE' \, \exp\{-[2(E - E')/F]^2 \ln 2\} \right)^{-1}$$ (22)

F is the full width at half maximum, and E_i and E_f are the lowest and highest energies in the convolution. The finite-resolution density of reactive states $\rho^J(E; F)$ is then defined by

$$\rho^J(E; F) = \frac{d}{dE} N^J(E; F)$$ (23)

Averaging over an energy width can be thought of as selecting a particular time regime for analysis. Observing the cumulative reaction probability, or any function of energy, with a finite resolution F corresponds to observing a time scale of $\Delta t = \hbar/F$ (37). In many cases, we expect total rate constants to be dominated by short-time dynamics in the vicinity of the transition state (38–42). Thus we might expect that looking at the cumulative reaction probability with a resolution broad enough to smooth over features due to longer-time dynamical effects (such as trapped-state resonances and entrance channel and exit channel couplings) will reveal broader structure due to quantized transition states.

Separating time scales in terms of energy is familiar in spectroscopy. This idea has been well expressed, for example, by Heller (43): "a spectrum taken at ultrahigh resolution (and containing long-time information) contains within it all lower-resolution information (i.e., shorter-time information). We can *choose* to examine it at lower resolution and extract the dynamics corresponding to shorter and shorter times."

III. COMPUTATIONAL METHODS

Accurate quantum mechanical cumulative reaction probabilities and densities of reactive states were obtained by carrying out converged quantum dynamics calculations for realistic potential energy surfaces. The wave function was expanded in a multiarrangement basis set (44–49), and the coefficients were found by linear algebraic methods employing a variational principle. In particular either the generalized Newton variational principle (GNVP) (50–54) or the outgoing wave variational princple (OWVP) (55–58) was used to obtain scattering matrix elements that are stationary with respect to small variations in the wave function. Full details of the basis sets and numerical methods used in these calculations are presented in previous publications from our group (53,54,58–63). One point that deserves to be emphasized though is that the method is made efficient by partitioning the Hamiltonian into distortion blocks and coupling potentials.

The reaction probabilities are well converged with respect to basis set and numerical parameters. This is extremely important since differentiation with respect to energy must yield smooth densities, and hence we give additional details of the convergence for the two new sets of calculations presented in this chapter, namely those for D + H$_2$ and those for F + H$_2$.

For the D + H$_2$ reaction, all calculations were carried out with the OWVP using techniques and parameters described previously (64). In particular, for the results presented here, we used parameter set A for $J = 12$ and 15 and parameter set B for $J = 0$–9. In both these parameter sets the basis functions are half-integrated Green's functions for open channels and $\mathscr{L}^2$ functions for closed channels. Specifically for the present chapter we repeated the calculations for $JPS = 3++$ with a parameter set in which all basis sets and numerical parameters were better converged as compared to set B. At 21 energies from 1.20–1.60 eV, the average unsigned percentage difference in the cumulative reaction probabilities from those computed with set B was <0.06%, and the maximum percentage difference was 0.18%. Furthermore the densities of reactive states, computed as derivatives of cubic spline fits, were almost indistinguishable when superimposed.

We also used the OWVP for the F + H$_2$ reaction. Two parameter sets that were used in the calculations are given in Table 1.

IV. H + H$_2$

In this section we discuss the quantized transition state spectra of H + H$_2$ with emphasis on the assignment of quantum numbers and transmission coefficients. The discussion is focused on the total CRP. Another very important aspect of the H$_3$ quantized transition states is their role in determining state-selected and state-to-state transition probabilities; we refer the reader to previous discussions (9,16) for that subject.

A. *J* = 0

The *J*-selected cumulative reaction probability $N^0(E)$ for the H + H$_2$ reaction computed (8,9) using the double many-body expansion (DMBE) potential energy surface (65) is shown versus energy as the solid line in Fig. 1a. (We will consistently use energy units of eV; 1 eV/molecule = 96.48 kJ/mol.) The CRP as a function of energy is characterized by steplike structures as predicted by transition state theory. The energy derivative of $N^0(E)$, obtained by analytically differentiating the cubic spline fit of Fig. 1a, is the density of reactive states $\rho^0(E)$, shown as the solid line in Fig. 1b. The derivative converts the steps in N^0 to peaks in ρ^0, akin to the bell-shaped curves ρ_τ of Eq. (15). The CRP reaches a value of 8.9 at 1.6 eV. Therefore, transition state theory would predict that there are nine energy levels of a quantized transition state at energies below 1.6 eV if all transmission coefficients are unity or more than nine if not all of the transition states are perfect dynamical bottlenecks. Figure 1b clearly shows seven peaks and one shoulder, and these are identified with eight transition state energy levels. The detailed analysis here suggests that there are a total of 10 quantized transition states contributing to Fig. 1b.

The density of reactive states $\rho^0(E)$ was fit by a sum of terms $\kappa_\tau \rho_\tau(E)$, as given in Eqs. (14) and (15), appropriate to scattering by parabolic potential energy barriers. (Note that the use of the parabolic barrier is the simplest barrier shape for understanding $\rho^0(E)$

Table 1 Parameter Sets for F + H$_2$ CRP Calculations for the 6SEC Surface

	Explanation	Set A		Set B	
		F + H$_2$	HF + H	F + H$_2$	HF + H
$j_{max}(\nu = 0)$	a	13	24	13	24
$j_{max}(\nu = 1)$	a	13	24	13	24
$j_{max}(\nu = 2)$	a	11	22	11	22
$j_{max}(\nu = 3)$	a	11	19	11	19
$j_{max}(\nu = 4)$	a	9	17	9	15
$j_{max}(\nu = 5)$	a	9	17	—	10
$j_\alpha^d(\nu = 0)$	b	6	13	6	13
$j_\alpha^d(\nu = 1-3)$	b	1	13	—	13
$j_\alpha^d(\nu = 4-5)$	b	1	1	—	—
$R_{\alpha 1}^G(a_0)(\nu = 0)$	c	2.85	2.4	3.85	2.94
$R_{\alpha 1}^G(a_0)(\nu = 1-3)$	c	2.85	2.4	4.2	2.94
$R_{\alpha 1}^G(a_0)(\nu \geq 4)$	c	2.85	2.4	4.2	3.3
$\Delta(a_0)(\nu = 0)$	d	0.25	0.18	0.25	0.27
$\Delta(a_0)(\nu \geq 1)$	d	0.25	0.18	0.30	0.27
$c(\nu = 0)$	e	1.25	0.63	1.0	0.864
$c(\nu \geq 1)$	e	1.25	0.63	1.2	0.864
$m^g(\nu = 0)$	f	16	18	10	8
$m^g(\nu = 1)$	f	16	18	—	8
$m^g(\nu = 2-3)$	f	16	18	—	10
$m^g(\nu \geq 4)$	f	16	18	—	—
$m^c(\nu = 0)$	g	—	—	—	—
$m^c(\nu = 1)$	g	—	—	7	—
$m^c(\nu = 2-3)$	g	—	—	7	—
$m^c(\nu \geq 4)$	g	—	—	7	8
$N_\alpha(HO)$	h	90	90	60	60
$N_{\alpha\alpha}^{QA}$	i	80	80	40	40
N_{12}^{QA}, N_{23}^{QA}	i	200	200	80	0
N_α^{QV}	j	50	50	25	25
N_α^{QSV}	j	25	25	25	25
N_α^{QGLV}	j	2	2	1	1
$r_{\alpha,min}^{QV}$	j	0.5	0.5	0.5	0.5
$r_{\alpha,max}^{QV}$	j	3.2	3.2	3.2	3.2
$N_\alpha(F)$	k	399	398	203	365
N_α^{FD}	l	13	13	13	13
$N_{\alpha,N_\alpha(F)}^{FD}$	l	8	8	8	8
$R_{\alpha 0}^F(a_0)$	m	2.3	1.5	2.3	1.5
$R_{\alpha,N_\alpha(F)+1}^F(a_0)$	m	18.0	18.0	18.0	22.0
$R_{\alpha,min}^{QR}$	n	2.3	1.5	2.8	1.75
$R_{\alpha,max}^{QR}$	n	18.0	18.0	10.0	10.0
N_α^{SD}	o	35	35	35	35
f_α^{SD}	p	0.9	0.9	0.9	0.9
n_α^{FR}	q	0	0	0	0
GSS_α	r	0	0	0	0
N_α^{QS}	s	52	33	24	30
N_α^{QGL}	s	7	11	7	11
ϵ_x	t	10^{-7}		10^{-6}	

Table 1 Continued

	Explanation	Set A		Set B	
		F + H$_2$	HF + H	F + H$_2$	HF + H
ϵ_{rad}	u	10^{-5}		10^{-100}	
ϵ_t	v	10^{-8}		10^{-8}	
ϵ_W	w	10^{-7}		10^{-7}	
ϵ_B	x	10^{-5}		10^{-5}	

[a] $j_{max}(v)$ is the maximum value of the rotational quantum number in vibrational level v included in the vibrational-rotational-orbital basis. In these calculations we did not eliminate higher values of the body-frame angular momentum projection Ω.

[b] $j_a^d(v)$ is the number of rotational states that are fully coupled in the distorted waves. Channels with $j \geq j_a^d(v)$ are treated as uncoupled in the distorted waves, as explained in Ref. 61.

[c] $R_{\alpha 1}^G$ is the value of R_α at the center of the innermost radial Gaussian function, where R_α is the mass-scaled atom-to-diatom distance defined in Ref. 58, and radial Gaussians are used both directly as outgoing wave basis functions (in the OWVP) and to generate half-integrated Green's functions (in the GNVP and OWVP).

[d] Δ is the spacing in R_α between successive radial Gaussians.

[e] c is the radial Gaussian overlap parameter, which determines the widths of the Gaussian functions, as explained in Ref. 59.

[f] m^g is the number of radial half-integrated Green's functions per channel.

[g] m^c is the number of radial Gaussians per channel used as $\mathscr{L}^2$ basis functions for the outgoing wave.

[h] $N_\alpha(HO)$ is the number of harmonic oscillator functions used to expand the diatomic adiabatic vibrational eigenfunctions, which in turn are used as vibrational basis functions for the scattering calculations.

[i] $N_{\alpha\alpha}^{QA}$ and $N_{\alpha\alpha'}^{QA}$ are the number of points in the Gauss-Legendre quadrature used in the single- and multiarrangement angular quadratures, respectively. (Note that $\alpha = 1$ is F + H$_2$, $\alpha = 2$ and 3 are HF + H.)

[j] N_α^{QV} is the total number of points in the quadratures of the interaction potential over the vibrational coordinate. In the present calculations the quadratures are carried out by dividing the mass-scaled vibrational coordinate r_α into N_α^{QVS} segments extending from $r_{\alpha,min}^{QV}$ to $r_{\alpha,max}^{QV}$. Each segment is then integrated by a N_α^{QGLV}-point Gauss-Legendre quadrature.

[k] $N_\alpha(F)$ is the total number of points in the finite difference grid used for the calculation of the regular solution of the distortion problems and the half-integrated Green's functions.

[l] N_α^{FD} and $N_{\alpha,N_\alpha(F)}^{FD}$ are the number of points used in the representation of the second derivative operator in the main body of the finite difference grid and at the last grid point respectively.

[m] $R_{\alpha 0}^F$ and $R_{\alpha,N_\alpha(F)+1}^F$ are, respectively, the location of the lower and upper finite difference boundary condition points.

[n] $R_{\alpha,min}^{QR}$ and $R_{\alpha,max}^{QR}$ are the lower and upper bounds of the region of R_α over which quadratures of the variational functional are carried out.

[o] N_α^{SD} is the number of points appended to the main part of the finite difference grid with geometrically decreasing spacing.

[p] f_α^{SD} is the step-size decrease factor for the spacing of the final finite difference grid points.

[q] n_α^{FR} is the number of extra points inserted between neighboring points in the third step of the finite difference grid generation scheme explained in Ref. 61.

[r] GSS$_\alpha$ is the grid spacing scheme for the radial quadrature grids, as explained in Ref. 61.

[s] N_α^{QS} is the number of repetitions of N_α^{QGL}-point Gaussian quadrature used in the generation of the finite difference grid and the integrations over R_α.

[t] ϵ_x is the vibrational screening parameter. (Screening parameters are explained in Ref. 57.)

[u] ϵ_{rad} is the radial screening parameter.

[v] ϵ_t is the translational basis screening parameter.

[w] ϵ_W is a screening parameter involving the matrix **W**.

[x] ϵ_B is a screening parameter involving the matrix **B**.
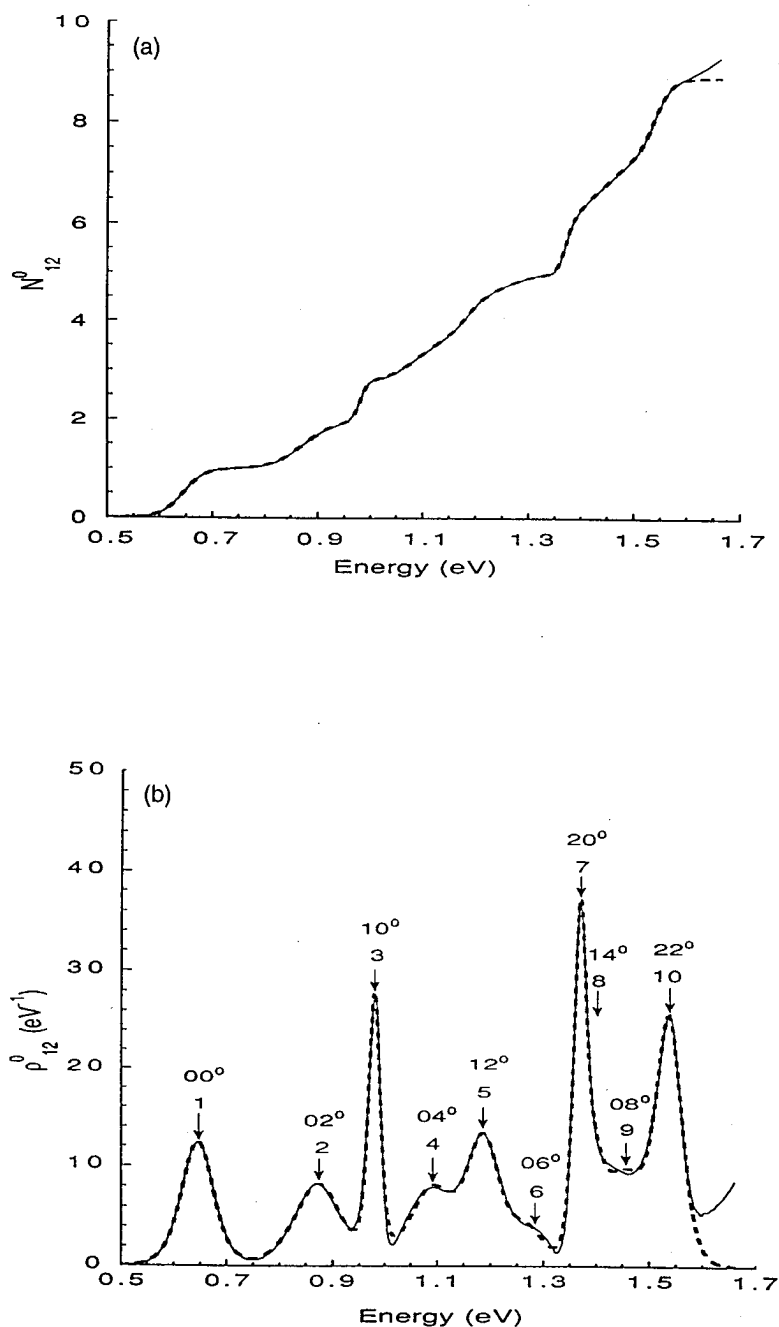
Figure 1 H + H_2, J = 0. (a) Cumulative reaction probability. The solid curve is a spline fit to the accurate quantal results, and the dashed curve was obtained by integrating the synthetic density in b. (b) Density of reactive states. The solid curve is obtained by analytically differentiating a cubic spline fit to the accurate quantum mechanical CRPs. The heavy dashed curve is the fit of Eqs. (14) and (15). The arrows are positioned at the fitted values of E_n, and the feature numbers and assignments above the arrows correspond to Table 2. (Reprinted with permission from Ref. 8, copyright 1991, American Chemical Society.)

and does not imply that the true barriers are parabolic, just as using the harmonic oscillator model to interpret ordinary spectra does not imply that the potentials are precisely quadratic.) Each term $\kappa_\tau \rho_\tau(E)$ in the sum represents the contribution of the individual energy level of the transition state. The quantities κ_τ, E_τ, and W_τ are fitting parameters.

All of the features in the quantal $\rho^0(E)$ are fit very accurately by including 10 terms in the sum. The parameters from the fit are included in Table 2. The sum of the terms $\kappa_\tau \rho_\tau$ in the fit is shown in Fig. 1b as the dashed curve, which is nearly indistinguishable from the quantal result. By integrating the fit to the quantal density of reactive states, we obtain a synthetic curve for the CRP. This is shown in Fig. 1a as a dashed curve, which to plotting accuracy is indistinguishable from the quantal result.

The excellent agreement between the quantal and synthetic densities of reactive states in Fig. 1b demonstrates that quantized transition states globally control the chemical reactivity. All of the reactive flux, up to an energy of 1.6 eV, can be attributed to contributions from the energy levels of the transition state; i.e., there is no noticeable background. Thus, this study (and ones to follow) provides a strong validation for approximate transition state theories that postulate the existence of transition states controlling the reaction dynamics.

The value of the transmission coefficient κ_τ is shown for each feature in Table 2. (The value of κ_τ for the last feature is greater than 1 because it includes contributions from higher energy transition states that have not been included in the fit.) Many of the values of the transmission coefficients are very close to unity, suggesting that these features correspond to quantized transition states that are nearly ideal dynamical bottlenecks to the reactive flux. Several of the values of κ_τ deviate from unity; this could be the result of the assumption of parabolic effective potential barriers or from recrossing or other multidimensional effects.

Each of the 10 energy levels of the H_3 quantized transition state can be associated with a set of linear-triatomic quantum numbers (66) $[\nu_1 \nu_2^K]$ where ν_1 and ν_2 are the stretch and bend quantum numbers respectively for modes orthogonal to the reaction coordinate

Table 2 Quantized Transition States for $H + H_2$, $J = 0$

Feature	E_τ (eV)	κ_τ	W_τ (10^{-2} eV)	Assignment	Adiabatic energy (eV)	$E(\nu_1 \nu_2)$ (eV)	Δt (TSRT)[a] (fs)	Δt accurate[b] (fs)
1	0.645	1.00	2.01	$[00^0]$	0.663	0.645	10	11
2	0.872	0.97	2.95	$[02^0]$	0.909	0.872	7	10
4	1.094	0.98	3.30	$[04^0]$	1.173	1.094	6	5
6	1.286	0.18	1.48	$[06^0]$	1.452	1.309	14	
9	1.494	1.01	3.02	$[08^0]$	1.754	1.517	7	
3	0.978	0.79	0.75	$[10^0]$	0.979	0.978	28	28
5	1.192	1.02	2.17	$[12^0]$	1.173	1.192	10	8
8	1.405	0.80	2.14	$[14^0]$	1.430	1.399	10	
7	1.368	1.01	0.78	$[20^0]$	1.384	1.368	27	30
10	1.538	1.15	1.40	$[22^0]$	1.513	1.567	15	12

[a]Transition state resonance theory (TSRT) results from Eq. (29) and the W_τ values given here.
[b]From Ref. 96.

and K is the vibrational angular momentum (also the magnitude of the projection of J on the molecular axis). (Here the vibrational angular momentum is denoted K rather than ℓ, which is conventional in spectroscopy (66), but which we reserve for orbital angular momentum. For $J = 0$, K must be 0 as well.) This type of assignment corresponds to the conventional picture where the one degree of freedom corresponding to unbound motion along the reaction coordinate is "missing." (By comparison, a stable triatomic molecule like CO_2 has a "full" set of quantum numbers $(v_1 v_2^K v_3)$ (66), with v_3 the asymmetric stretch quantum number. The quantum number "missing" in the transition state description will reappear when we treat the transition state as a quantum mechanical resonance.)

The lowest energy feature in $\rho^0(E)$ at 0.645 eV is easily assigned as $[00^0]$ since it is the overall reaction threshold and thus corresponds to the lowest energy level of the transition state. We are able to assign quantum numbers v_1 and v_2 to the other nine energy levels that affect the spectrum in this figure by using a variety of methods (8,9), but primarily by comparing the fitted values of E_τ with the barrier maxima of semiclassical vibrationally adiabatic potential energy curves. The vibrationally adiabatic curves are defined by (35,67–71)

$$V_a(v_1, v_2, K, J, s) = V_{MEP}(s) + \varepsilon_{int}(v_1, v_2, K, J, s) \tag{24}$$

where s is the distance along the reaction path ($s = 0$ at the saddle point), $V_{MEP}(s)$ is the Born-Oppenheimer potential energy along the reaction path, and $\varepsilon_{int}(v_1, v_2, K, J, s)$ is the vibrational-rotational energy of the stretch, bend, and rotational motions excluding motion along the reaction coordinate. The stretching motion (with quantum number v_1) of the H_3 transition state correlates adiabatically with the vibrational motion (with quantum number v) in the reactant H_2 molecule (72). The bend is doubly degenerate and— along with overall rotation—correlates to the orbital-rotational motions of the reactants (73). The vibrationally adiabatic curves (labeled by v_1, v_2, and K) were calculated in internal coordinates using the WKB method to treat the stretch anharmonicity (74) and a variation-perturbation treatment (75) of a quadratic-quartic potential (76) to treat bend anharmonicity. Coriolis interactions were neglected so the curves are independent of K. The energies of the maxima of these curves are in good agreement with the E_τ values obtained by fitting the density of reactive states (8,16). This comparison allows us to make the assignments shown in column 5 of Table 2. Energies of the maxima in $V_a(v_1, v_2, K, J, s)$ are shown as column 6 in that table. (For the more highly bend excited states, the semiclassical energies are less accurate, and other methods (8,9) were used to make more convincing assignments of these quantum numbers.) Notice that for $J = 0$ only even v_2 states appear, just as in the $J = 0$ spectra of bound linear triatomics (66).

The good agreement between the energy levels of the quantized transition state obtained from the exact quantum dynamics calculations and the maxima of vibrationally adiabatic curves strongly suggests that the reactive flux is "focused" (77) in the interaction region through dynamical bottlenecks that are locally vibrationally adiabatic. The overall chemical reaction is not globally adiabatic (8,9); for example, many state-to-state reaction probabilities with $v \neq v'$ have significant magnitudes ($> 10^{-3}$). Thus we conclude that adiabaticity is a better approximation at the transition state itself than globally and that the flux passing through a particular level of the transition state may originate from a wide set of reactant states. One way to understand this is to consider that at a barrier maximum, the motion along the reaction coordinate is classically stopped. Thus the simplest criterion for vibrational adiabaticity, that vibrational motions transverse to the

reaction coordinate be fast compared to motion along the reaction coordinate, is locally satisfied.

With all of the ν_1 and ν_2 assignments made, some interesting trends in the fitted parameters κ_τ and W_τ appear. From Table 2, we see that the significant deviations of κ_τ from unity are generally found for the highly bend excited transition state levels. Therefore, most of the breakdown of transition state theory appears to be associated with only those few levels. In addition, we see in Table 2 that W_τ becomes larger as ν_2 is increased from 0 to 2 for a given value of ν_1. This is consistent with the discussion below Eq. (13) since the vibrationally adiabatic potentials become narrower as ν_2 increases (8,16). This same trend in W_τ is even more apparent in the results discussed below for H + H_2, $J = 1$, where both even and odd values of ν_2 are allowed.

We conclude above that the $J = 0$ cumulative reaction probability is globally controlled by quantized transition states, and we have assigned stretch (ν_1) and bend (ν_2) quantum numbers for the motion orthogonal to the reaction coordinate. As discussed below, similar conclusions can be reached for the $J = 1$ and $J = 4$ cumulative reaction probabilities. We have obtained spectroscopic constants for the H_3 transition state by fitting the E_τ values of $[00^0]$, $[02^0]$, $[04^0]$, $[10^0]$, $[12^0]$, and $[20^0]$ for $J = 0$ and $[00^0]$ for $J = 4$ by (66)

$$\frac{E(\nu_1, \nu_2, J)}{hc} = \frac{E_0}{hc} + \omega_1(\nu_1 + 0.5) + \omega_2(\nu_2 + 1) + x_{11}(\nu_1 + 0.5)^2$$
$$+ x_{22}(\nu_2 + 1)^2 + x_{12}(\nu_1 + 0.5)(\nu_2 + 1) + BJ(J + 1) \tag{25}$$

where E_0 is a constant, and ω_1, ω_2, x_{11}, x_{12}, x_{22}, and B are the usual spectroscopic fitting parameters. The fit, which reproduced the energies within about 0.02 eV, yielded values (in cm^{-1}) of $E_0 = 3061$, $\omega_1 = 2295$, $\omega_2 = 972$, $x_{11} = 227$, $x_{22} = -6$, $x_{12} = -58$, and $B = 10.6$. These parameters compare favorably with the approximate values (78) obtained by a normal modes calculation at the saddle point: $E_0 = 3372$, $\omega_1 = 2067$, $\omega_2 = 899$, and $B = 9.7$.

Energy levels $E(\nu_1, \nu_2, J = 0)$ of the transition state predicted by these spectroscopic constants are shown in Table 2 to be in good agreement with the values of E_τ obtained by fitting the density of reactive states. When Eq. (25) is applied to bound states, an implicit assumption is that the quantized states have vibrational motion about the same "equilibrium" geometry. The vibrationally adiabatic curves (8,16) suggest though that the variational transition states are found at different points along the reaction coordinate and therefore different geometries. In light of this and as the values obtained with Eq. (25) are effective values since Eq. (25) is a truncation of an infinite Taylor series, the good agreement obtained with Eq. (25) is quite remarkable.

The correspondence between the energies of the quantized transition states and the maxima of vibrationally adiabatic curves, as well as the success in using a model of transmission through effective potential energy barriers to fit the density of reactive states, both suggest that detailed explorations of the nature of scattering by one-dimensional potential barriers can provide further insight. In classical mechanics, a potential maximum is associated with metastability at the energy of the maximum and with a time delay for higher energies due to the system slowing down as it crosses the top of the barrier. In quantum mechanics, barrier passage is also associated with a time delay (79–81) manifested as an increasing phase in scattering matrix elements (relative to the background phase). In model studies of quantum mchanical transmission through and over potential barriers, it has been shown that the time delays corresponding to barrier passage are

associated with poles of the scattering matrix at complex energy (82–84). Since poles of the scattering matrix represent quantum mechanical resonances (3,5,50,85,86), we have concluded that chemical reaction thresholds associated with barriers, i.e., quantized transition states, are reactive scattering resonances. These so-called barrier resonances tend to be associated with shorter time delays than conventional resonances attributed to a particle trapped in a well between barriers. However, there is no distinction in kind between these two types of poles of the scattering matrix: barrier resonances may be transformed continuously into trapped-state resonances by varying the shape of the one-dimensional potential function (83,84). In fact, in our H + H_2 work (8,9,16) as well as our one-dimensional studies (83,84) we have found that a single resonance may partake of both barrier and trapped-state resonance characters. The identification of transition states as scattering resonances has also been made by applying a complex scaling transformation to the reaction coordinate (87).

The characterization of transition states as resonances is a useful analytical tool and provides new insights into fundamental problems of chemical reactivity. It has already been used, for example, to lead to a new computational approach for the calculation of anharmonic transition state energy levels by a reformulation of variational transition state theory (88).

Semiclassical transition state theory based on second-order perturbation theory (89) provides another way to assign quantized energy levels of the transition state, and an application (90) to the H + H_2 reaction yielded encouraging results in comparison to the full quantum (8) calculations. One difference in assignments (8,90) was later explained (88), using the resonance theory reformulation of variational transition state theory, as a consequence of the inadequacy of second-order perturbation theory.

Treatment of transition states as resonances is complicated by the fact that, in many cases, barrier resonances will not be isolated or narrow and the theory of overlapping resonances (91,92) is more complicated than the theory of isolated, narrow resonances. Analyses of the poles of the scattering matrix show that even with a simple barrier, there is more than one pole (82–84,93,94) associated with barrier passage. On the other hand, our work on H + H_2 and other systems to be described shows that in many cases the transition states are resolvable and the observable structure in the dynamical $N^J(E)$ and $\rho^J(E)$ may be correlated with one or a small number of poles. This paradoxical situation is resolved by noting that, when resonances are broad and overlapping, it is the pole nearest to the real energy axis that is useful for understanding the features of the dynamical observables. In particular, for a series of poles associated with a simple (e.g., parabolic or approximately parabolic) barrier, one can assign a new quantum number v to each member of the sequence, with $v = 0$ assigned to the pole closest to the real energy axis, $v = 1$ to the next closest pole and so on. This quantum number v is associated with the "missing" degree of freedom of the quantized transition state. The $v = 0$ transition state is used for understanding the dynamics in real time, as discussed next.

Poles in the scattering matrix occur at complex resonance energies (50,85,86)

$$\overline{E} = E_{res} - \left(\frac{i}{2}\right)\Gamma \tag{26}$$

where E_{res} is the real part of the resonance energy and Γ is the real, positive resonance width, which is related to the collision lifetime Δt by (95)

$$\Delta t = \frac{2\hbar}{\Gamma} \tag{27}$$

The complex resonance energies of the poles for the parabolic barrier of Eq. (10) are (82,93)

$$E_\nu = E_\tau - i\hbar|\omega_\tau|\left(\nu + \frac{1}{2}\right) \tag{28}$$

where ν is the analogue of the "missing" quantum number ν_3. If we assume that the pole with $\nu = 0$ dominates the behavior of the quantal reaction probability (for scattering by a parabolic barrier), then using Eqs. (12) and (26)–(28) yields

$$\Delta t = \frac{\hbar}{\pi W_\tau} \tag{29}$$

Values of Δt computed from the W_τ parameters of Table 2 are also included in Table 2, labeled TSRT (transition state resonance theory). They compare favorably with Δt values obtained (96) from accurate quantum dynamical scattering matrix elements without using transition state theory or resonance theory; these latter values are given in the last column of Table 2. It is important to note that whereas the W_τ values are obtained from fits to reaction probabilities (which contain no information about the phases of the scattering matrix elements), the direct calculation (96,97) of Δt depends explicitly on phases. Thus there is no a priori reason why the Δt values must compare favorably. The fact that they do provides further evidence of the utility of treating transition states with resonance theory.

Cuccaro et al. (96) interpreted the time delays in Table 2 as resonances and assigned a value of 0 for the third quantum number ν without explanation. We identify these resonances as quantized transition states. The analysis presented above of scattering by one-dimensional barriers, with the conclusion that the $\nu = 0$ pole is the most important because it is closest to the real energy axis, supplies a justification for the assignment of the third quantum number.

The steplike CRP originally obtained (8) from quantum mechanical scattering calculations has also been reproduced by a trace formula that avoids explicit specification of asymptotic states (98,99) and by a method based on eigenvalues of a reaction probability operator (100).

B. J = 1

A similar analysis of the CRP and the density of reactive states for H + H_2 with total angular momentum J equal to 1 also shows quantized transition state control of the chemical reactivity (8,16). However, the spectra are more complicated because the number of features in $N^J(E)$ and $\rho^J(E)$ increases with J. This is because both even and odd values of ν_2 are allowed for nonzero J, and states with identical ν_1 and ν_2 but different K are allowed for $J > 1$. Note that $K \leq J$ and $K = \nu_2, \nu_2 - 2, \nu_2 - 4, \ldots, 0$ or 1. The degeneracy of a state $[\nu_1\nu_2^K]$ is 2 if K is nonzero and 1 if K is zero.

A fit of the density by a sum of terms $\kappa_\tau\rho_\tau(E)$, analogous to the fit for $J = 0$, identifies 20 features up to 1.7 eV, and 15 of these are labeled in Fig. 2. Assigning transition state quantum numbers to the fitted features was simplified by analyzing each parity block separately, as described next.

For transition states, the total parity is the product of the parities of the vibrational and rotational wave functions, and it depends on both J and K. The parity of the rotational wave function is $(-1)^J$. For $K = 0$, the vibrational wave function has even parity $(+1)$.
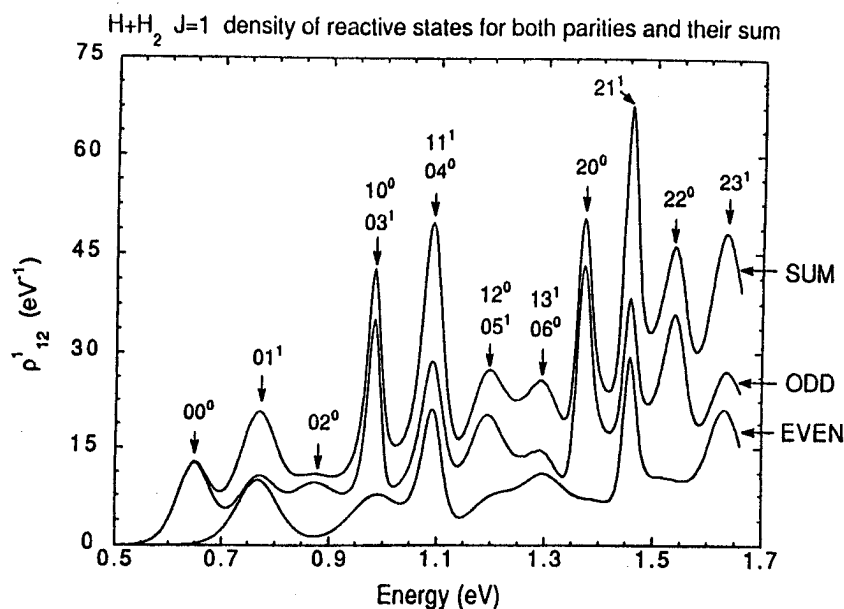
Figure 2 H + H_2, J = 1. Density of reactive states for both parities (ρ^{1-} labeled odd and ρ^{1+} labeled even) and their sum.

For $K > 0$, the bending mode is doubly degenerate and has one even-parity and one odd-parity component (66,96). For JP = 1+, then, ν_2 must be odd. Consequently, only states with K = 1, and hence odd ν_2, will appear in the density spectrum. For JP = 1−, the vibrational wave function is even, so both K = 0 and K = 1 states, and consequently both odd and even values of ν_2, are allowed. Figure 2 shows clearly that K = 0 states occur only in the odd parity block. The spectrum for JP = 1+ is similar to the spectrum for J = 0 in Fig. 1b, except that the $[\nu_1\nu_2^0]$ features in the J = 0 spectrum corresponds to $[\nu_1(\nu_2 + 1)^1]$ features in the JP = 1+ spectrum. All values of ν_2 are allowed for JP = 1−, so the spectrum for odd parity has twice as many features as that for even parity. The spectra for JP = 1+ and JP = 1− sum to give the spectrum for J = 1.

Assignments and values of E_τ, κ_τ, and W_τ from a fit by a sum of terms $\kappa_\tau\rho_\tau(E)$ are given in Table 3. The parameters E_τ, W_τ, and κ_τ for J = 1 exhibit the same trends as those for J = 0. Most of the κ_τ are close to 1, indicating that the quantized transition states are good dynamical bottlenecks. Again, most of the exceptions are highly bend excited states. The quantal and fitted densities are identical to plotting accuracy (9), indicating that quantized transition states can account for all of the chemical reactivity. Table 3 also shows that fitted energies match the predictions of Eq. (25) well with the parameters given earlier, differing by only 0.018 eV on average (the larger differences are for highly bend excited states).

It was mentioned in Sec. IV.A. that the widths of features in the density of reactive states generally increase with ν_2. The density for JP = 1− (Fig. 2) provides a striking demonstration of this. The first three peaks in Fig. 2 are due to states $[00^0]$, $[01^1]$, and $[02^0]$; the next four peaks are primarily due to states $[10^0]$, $[11^1]$, $[12^0]$, and $[13^1]$; and the last four peaks are primarily due to states $[20^0]$, $[21^1]$, $[22^0]$, and $[23^1]$. Inspection

Table 3 Quantized Transition States for $H + H_2$, $J = 1$

Assignment	$E(\nu_1, \nu_2)$ (eV)	E_τ (eV)	κ_τ $JP = 1+$	κ_τ $JP = 1-$	W_τ $(10^{-2}$ eV)
$[00^0]$	0.647	0.647		1.00	2.04
$[01^1]$	0.762	0.767	1.00	0.97	2.53
$[02^0]$	0.875	0.875		1.01	3.06
$[03^1]$	0.986	0.990	1.01	0.96	3.29
$[04^0]$	1.096	1.088		1.00	2.16
$[05^1]$	1.205	1.205	0.81	1.00	3.07
$[06^0]$	1.311	1.290		0.79	2.30
$[07^1]$	1.416	1.388	0.55	0.09	2.74
$[08^0]$	1.520	1.498		1.21	2.89
$[09^1]$	1.622	1.560	0.27	0.27	2.15
$[0\ 10^0]$	1.722	a		a	a
$[10^0]$	0.981	0.981		0.84	0.79
$[11^1]$	1.088	1.089	0.98	0.73	1.28
$[12^0]$	1.194	1.187		1.00	2.19
$[13^1]$	1.299	1.298	1.00	0.39	2.71
$[14^0]$	1.401	1.401		1.21	2.18
$[15^1]$	1.502	1.502	1.00	0.81	2.75
$[16^0]$	1.602	a		a	a
$[17^1]$	1.700	a	a	a	a
$[20^0]$	1.371	1.370		1.03	0.80
$[21^1]$	1.471	1.456	0.74	0.77	0.82
$[22^0]$	1.570	1.540		1.01	1.28
$[23^1]$	1.667	1.633,[b] 1.639[c]	1.91[b]	2.88[c]	2.34,[b] 2.73[c]

[a]This state's contribution is believed to be included in the unresolved feature nominally assigned as $[23^1]$.
[b]Values from the $JP = 1+$ fit.
[c]Values from the $JP = 1-$ fit.

of the odd-parity curve in Fig. 2 shows that the first peak of each of these three sets of peaks is the tallest and narrowest; the others become shorter and broader as energy increases. This trend is confirmed by the fit values of W_τ (9), and it is consistent with adiabatic transition state theory. As ν_2 increases for a given ν_1, peaks in vibrationally adiabatic curves become higher and narrower, causing tunneling to become significant over a wider range of energies. The related effect in the fully quantum world is that abrupt steps in $N^1(E)$ become smoothed out, and peaks in $\rho^1(E)$ become broader. The broader peaks are generally associated with shorter lifetimes, as demonstrated for $J = 0$. We also note that broader features in $\rho^1(E)$ generally have smaller peak heights because the integrated area under each is approximately the same, being one for an ideal transition state ($\kappa_\tau = 1$).

C. $J = 4$

The accurate cumulative reaction probability and density of reactive states (summed over parities) for $J = 4$ are shown in Fig. 3. The nine prominent features correspond to transition states with $\nu_2 = 0$, 1, or 2 for $\nu_1 = 0$, 1, and 2, just as in the $J = 1$ spectrum (9). States with $\nu_2 > 2$ also occur, but they are harder to identify because they are broad and

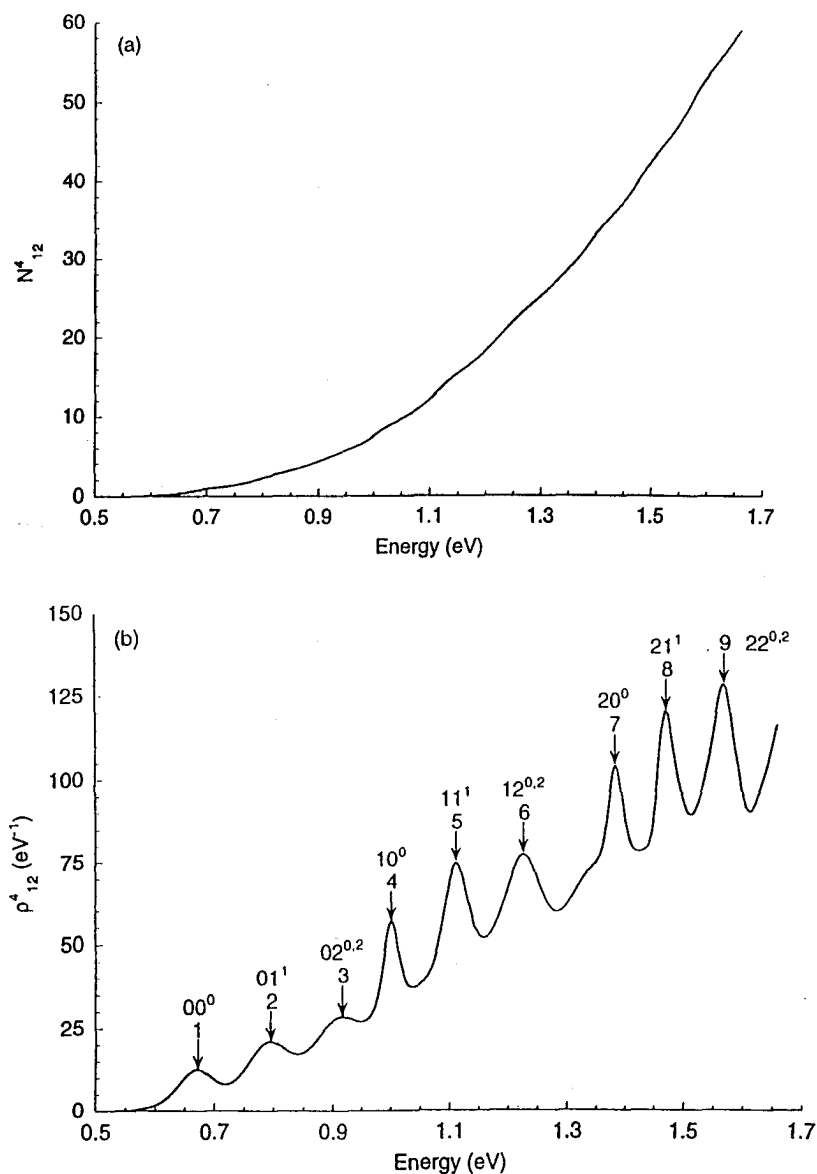**Figure 3** H + H_2, J = 4. (a) Cumulative reaction probability. (b) Density of reactive states. In part b, the peaks are labeled by feature numbers and by the assigned quantum numbers of one of the levels contributing to the peak. See Table 4 for the complete set of assignments.

overlapping. Ignoring K-splitting, transition states with nonzero values of ν_2 (less than or equal to J) have a degeneracy of $\nu_2 + 1$ (66). [The K-splitting is much smaller than the spacing of (ν_1, ν_2) levels.] The density's apparently rising baseline is due to the number of these broad, overlapping features increasing with energy; on top of this background, the prominent features due to low ν_2 can be distinguished. Table 4 shows our assignments of the first nine peaks for J = 4, which were made primarily on the basis

Table 4 Quantized Transition State Spectrum for $H + H_2$, $J = 4$

Feature	Energy (eV)	States	Sum of degeneracies of these states	Running sum	N^4
1	0.671	$[00^0]$	1	1	1
2	0.794	$[01^1]$	2	3	3
3	0.917	$[02^{0,2}]$	3	6	5½
4	1.002	$[10^0]$, $[03^{1,3}]$	5	11	9½
5	1.113	$[11^1]$, $[04^{0,2,4}]$	7	18	16
6	1.228	$[12^{0,2}]$, $[05^{1,3}]$	7	25	24
7	1.383	$[20^0]$, $[13^{1,3}]$, $[06^{0,2,4}]$	10	35	32
8	1.473	$[21^1]$, $[14^{0,2,4}]$, $[07^{1,3}]$	11	46	40
9	1.570	$[22^{0,2}]$, $[15^{1,3}]$, $[08^{0,2,4}]$	12	58	49½

of the spectroscopic constants and by comparison with the fitted quantal transition state energies E_τ for $J = 0$ and 1. This table illustrates that the running degeneracy sum reaches 25 after the first six features, as compared to 6 for $J = 0$.

The energies of the nine features in Table 4 all correspond closely to the energies of maxima in the vibrationally adiabatic potential curves (8). Table 5 illustrates the agreement between the energies predicted by the spectroscopic constants and maxima, E_{max}, in the quantal density of reactive states.

Fitting the quantal density by a sum of terms $\kappa_\tau \rho_\tau(E)$ is difficult because of the large number of transition states for $J = 4$. However, quantized transition state control of chemical reactivity can be assessed for $J = 4$ without identifying all of the individual contributions to the total density by comparing the accurate values of $N^4(E)$ with those in the next to last column of Table 4. If the transition states were ideal ($\kappa_\tau = 1$), the two numbers would be equal. Up to 1.228 eV, the energy of the sixth peak, the numbers are very close; at 1.228 eV the accurate value of $N^4(E)$ is 24. Thus, the quantized transition states up to 1.228 eV are nearly ideal dynamical bottlenecks. Above 1.228 eV the quantal $N^4(E)$ is somewhat smaller than the predicted value, but even at 1.570 eV the difference is only 15%. This difference may be due to the inaccuracy of Eq. (25) at high v_2 or to

Table 5 Assignments of Quantized Transition States for $H + H_2$, $J = 4$

Feature	$E(v_1 v_2)$ (eV)	Assignment	E_{max} (eV)
1	0.671	$[00^0]$	0.671
2	0.783	$[01^1]$	0.794
3	0.899	$[02^{0,2}]$	0.917
4	1.005	$[10^0]$	1.002
5	1.111	$[11^1]$	1.113
6	1.213	$[12^{0,2}]$	1.228
7	1.394	$[20^0]$	1.383
8	1.494	$[21^1]$	1.473
9	1.593	$[22^{0,2}]$	1.570

deviations of κ_τ from unity at high values of the total energy or of ν_2. In any case, these results show that transition state control of chemical reactivity is maintained up to high energy and that the individual transition states are relatively good bottlenecks for $J = 4$. This strongly suggests that the detailed trends identified for $J = 0$ and $J = 1$ are general and that thermal rate constants, which depend on a weighted sum of J-specific terms (see Sec. II), are determined by the energy levels of the quantized dynamical bottleneck up to high temperature (>1000 K) (101).

V. O + H₂

The $O(^3P) + H_2$ reaction was studied (12–14,102,103) with the Johnson-Winter-Schatz (JWS) London-Eyring-Polanyi-Sato-type (LEPS type) potential energy surface (104,105). This surface was originally parameterized to give reasonably accurate thermal rate constants (104), and its qualitative features are similar to later, more accurate surfaces (12,102–110). We use the JWS potential rather than the more accurate surfaces because the JWS potential has better global analytic behavior in all chemical rearrangements, which is necessary for the reactive scattering calculations reported here. The JWS surface has a collinear saddle point, and the $V_{MEP}(s)$ curve, although asymmetric by a few kcal/ mol, has roughly the same shape as that for $H + H_2$ and $D + H_2$.

A. Variational and Supernumerary Transition States

The $O(^3P) + H_2 \to OH + H$ reaction provides a further test of the generality of analyzing chemical reactivity in terms of quantized transition states. The reaction of O with H_2, like that of H with H_2, is generally free of narrow trapped-state resonances and other long-lifetime dynamical effects. However, the $O + H_2$ reaction is more complicated than the $H + H_2$ reaction in that it is asymmetric (that is, reactants and products are different chemical species), and it has nonsymmetrically related multiple-bottleneck regions. This introduces the possibility of dynamical bottlenecks with different sets of energy levels on the reactant side and on the product side of the region of high-reaction-path curvature (102,107,109,110), and it is especially interesting to see if bottlenecks in both regions, as well as those near the approximately symmetric saddle point, exert observable influence on the reaction.

Vibrationally adiabatic potentials were calculated for $O + H_2$ using the same methods (74–76) as for $H + H_2$. Examples of these curves are shown in Fig. 4. For $\nu_1 > 0$, where ν_1 is the quantum number for the stretching motion transverse to the reaction coordinate, the adiabatic curves for this reaction exhibit several local maxima. However, only the first and last local maximum of each curve are plausibly associated with dynamical bottlenecks because the vibrational coordinates do not adjust adiabatically to reaction coordinate motion in the central region due to the large reaction path curvature. (111–113). Of the local maxima in the adiabatic regions, the first one is higher. For example, for $\nu_1 = 1$, $\nu_2 = 0$, where ν_2 is again the bending quantum number, it is 0.05 eV higher, and for $\nu_1 = 2$, $\nu_2 = 0$ it is about 0.09 eV higher than the product-side maximum. The difference increases with ν_1. If the reaction were completely vibrationally adiabatic, only the higher (reactant-like) maxima would influence reactivity. Therefore we call dynamical bottlenecks with reactant-like geometries variational transition states and designate them in the usual manner, i.e., $[\nu_1 \nu_2^K]$. However, many vibrationally non-adiabatic transitions have nonnegligible reaction probabilities in the exact quantal cal-
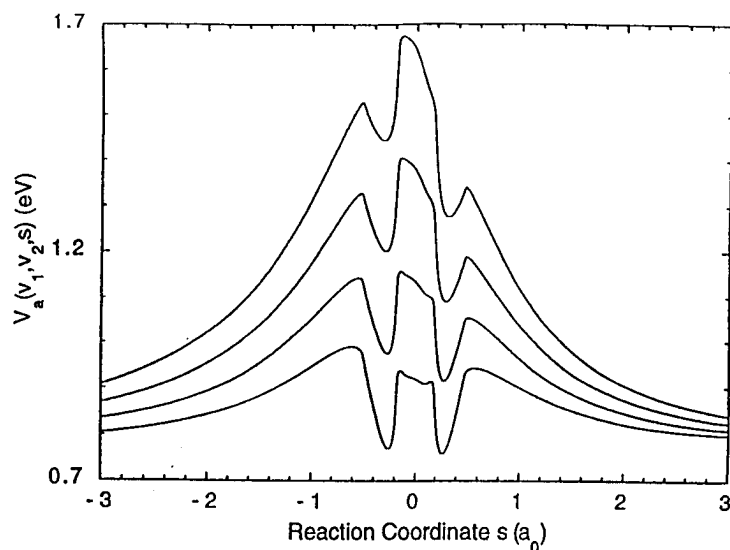
Figure 4 Vibrationally adiabatic potential curves for O + H_2 with $\nu_1 = 1$, $J = 0$, and $\nu_2 = 0, 2$, 4, and 6. From the bottom up the curves correspond to the $[10^0]$, $[12^0]$, $[14^0]$, and $[16^0]$ states. (Reprinted with permission from Ref. 14.)

culation. The possibility therefore exists that dynamical bottlenecks with product-like geometries may also have observable influence on the chemical reactivity. We call these supernumerary transition states, and we designate them with the letter S, i.e., $S[\nu_1\nu_2^K]$, to distinguish them from variational transition states with the same ν_1, ν_2, and K. We further distinguish between two kinds of supernumerary transition states: those of the first kind, whose influence on the total dynamics can be observed; and those of the second kind, whose influence on the total reactive flux is not detectable (14) but which do influence state-to-state reactivity.

B. Total Reactivity

The accurate density of reactive states O + H_2, $J = 0$ is shown in the top left panel of Fig. 5, and results of the quantized transition state theory fit are in Table 6, along with assignments discussed below. The quantal and fitted densities are indistinguishable to plotting accuracy (14), indicating that quantized transition states control the chemical reactivity. The density closely resembles that for the reaction of H with H_2 up to about 1.3 eV. Analogous features are associated with the same sets of quantum numbers through the $[06^0]$ transition state at 1.218 ev.

The fit identified 17 features up to 1.9 eV. The width parameter W_r generally scales inversely with ν_1 and directly with ν_2, as expected (14). For many of the states κ_r is very close to 1.00, and its smallest value is 0.54 (14). Thus many of the quantized transition states are nearly ideal dynamical bottlenecks, and even ones with large bend quantum numbers are quite good.

The maxima in the quantal density of reactive states and in the vibrationally adiabatic curves occur at almost the same energies. Thus, as for the H + H_2 reaction, the
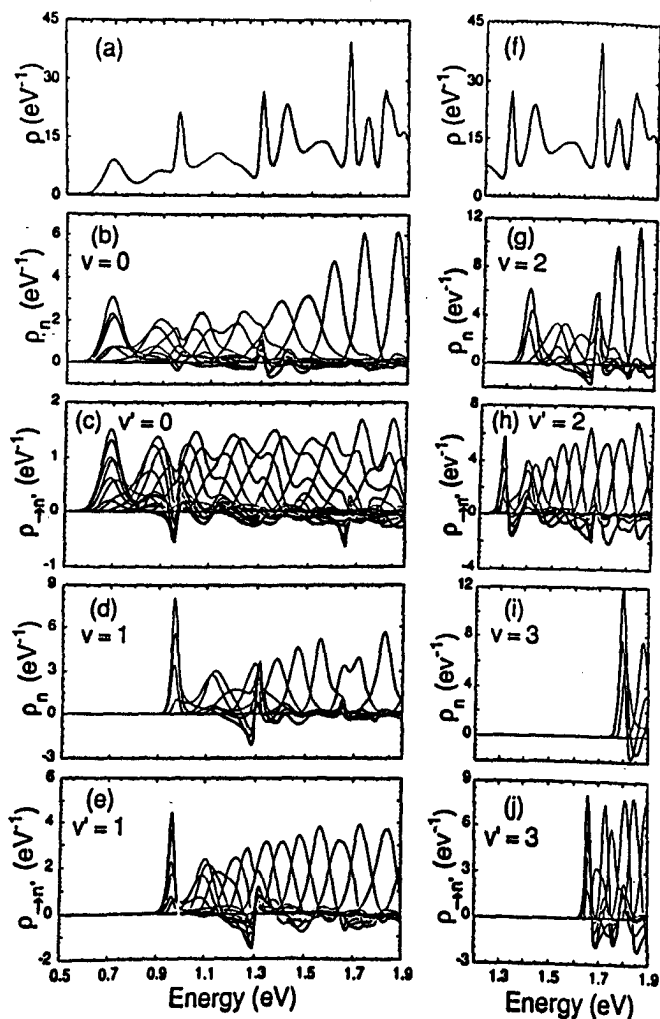
Figure 5 Total, $\rho^J(E)$, and partial, $\rho^J_{vj}(E)$ and $\rho^J_{\to v'j'}(E)$, densities of reactive states for O + H_2, $J = 0$. (a,f) Total. (b) $v = 0$, $j = 0-15$. (c) $v' = 0$, $j = 0-25$. (d) $v = 1$, $j = 0-12$. (e) $v' = 1$, $j' = 0-22$. (g) $v = 2$, $j = 0-9$. (h) $v' = 2$, $j' = 0-17$. (i) $v = 3$, $j = 0-4$. (j) $v' = 3$, $j' = 0-11$. (Reprinted with permission from Ref. 14.)

accurate quantum mechanical dynamics of O + H_2 is controlled by dynamical bottlenecks that are locally vibrationally adiabatic near quantized transition state energies. The first peak is obviously the [00°] transition state. The [02°] transition state was assigned first by Bowman (13), by analyzing our (12) cumulative reaction probabilities, which we made available to him prior to publication. The density has sharp peaks at the energies of both reactant-like and product-like maxima in the $v_1 = 2$ and $v_1 = 3$ vibrationally adiabatic curves. On this basis we identify the influence of four variational transition states, in particular [00°], [10°], [20°], and [30°], and two supernumerary transition states, in particular $S[20°]$ and $S[30°]$, on the density.

Table 6 Quantized Transition States for $O + H_2$, $J = 0$

Assignment	E_τ (eV)	κ_τ	W_τ $(10^{-2}$ eV$)$
$[00^0]$	0.695	0.96	2.62
$[02^0]$	0.877	0.89	3.82
$[10^0]$	0.969	0.62	0.92
$[04^0]$	1.040	1.00	4.16
$[12^0]$	1.133	1.00	3.03
$[06^0]$	1.218	0.54	2.62
$S[20^0]$	1.306	0.78	0.81
$[08^0]$, $[16^0]$	1.393	1.00	3.79
$[20^0]$, $S[22^0]$	1.400	1.01	1.60
$[0\ 10^0]$, $[18^0]$	1.501	1.00	3.22
$[22^0]$, $S[24^0]$	1.564	0.69	2.54
$[0\ 12^0]$, $[1\ 10^0]$	1.619	1.00	5.91
$S[30^0]$	1.662	0.96	0.68
$S[32^0]$	1.734	1.00	1.33
$[30^0]$	1.801	0.63	0.80
$S[34^0]$	1.829	0.85	1.20
$S[36^0]$	1.883	1.14	1.82

C. State-Selected Reactivity

Assignment of the remaining fitted features was made [14] largely on the basis of densities of state-selected reaction probability, ρ_n^0 and $\rho_{\rightarrow n'}^0$, presented in Fig. 5. Each of the panels (b) through (e) and (g) through (j) displays densities of state-selected reaction probability for a given value of v or v' and for each value of j or j' open up to 1.9 eV.

The first peak in each of the panels corresponds to one of the ground-bend states already identified: $[00^0]$ for $v = 0$ and $v' = 0$, $[10^0]$ for $v = 1$ and $v' = 1$, $[20^0]$ for $v = 2$, $S[20^0]$ for $v' = 2$, $[30^0]$ for $v = 3$, and $S[30^0]$ for $v' = 3$. Note that the first peak for $v' = 2$ ($v' = 3$) channels, identified with a supernumerary transition state, occurs at a lower energy than the first peak for $v = 2$ ($v = 3$) channels, just as the product-like maxima in the vibrationally adiabatic curves are lower than the reactant-like maxima.

The remaining peaks in each panel are associated primarily with bend-excited transition states in the corresponding vibrational manifold. For example, the maxima in the $v = 0$ and $v' = 0$ spectra in Figs. 5b and 5c correspond to transition states $[v_1 = 0;\ v_2 = 0, 2, 4, \ldots, 16^{K=0}]$. Several state-selected spectra, particularly those in the $v = 0$ and $v' = 0$ panels, exhibit double peaks whose maxima nearly overlap with prominent, neighboring peaks in other spectra. This is interesting for two reasons. First, overlapping maxima confirm that a quantized transition state controls reactive flux for the corresponding asymptotic states at energies near the maxima. Second, the existence of two prominent maxima for a single spectrum shows that the asymptotic state couples to two consecutive even-v_2 bend levels of the transition state. The overlapping of peaks also demonstrates that peak maxima do not locate transition state energies exactly, because the overlap is not perfect: relative to the peaks with which they overlap, the individual maxima of a double peak are shifted inward toward the average energy of the double peak.

We note that the peaks in ρ_n^0 and $\rho_{\to n'}^0$ do not correspond to the opening of asymptotic channels increasing sequentially in j (rotational thresholds). The energy spacing of rotational thresholds would increase linearly with j [the derivative of the $j(j + 1)$ quadratic energy expression is linear in j], where the peaks in Figs. 5b and 5c are evenly spaced, as are the levels of a harmonic oscillator.

The maxima in the vibrationally adiabatic curves at reactant-like and product-like geometries are nearly evenly spaced in energy for a given $\nu_1 > 0$ stretch manifold, but the latter are more closely spaced than the former (14). Likewise, prominent maxima in the $\nu = 1$ (Fig. 5d), $\nu' = 1$ (Fig. 5e), $\nu = 2$ (Fig. 5g), and $\nu' = 2$ (Fig. 5h) spectra are also nearly evenly spaced, with the spacing of peaks in the $\rho_n^0(E)$ spectra being larger than the spacing in the corresponding $\rho_{\to n'}^0$ spectra. (The $\nu = 3$ and $\nu' = 3$ spectra begin at too high an energy for the spacing to be judged.) A possible explanation is that the most prominent peaks in ρ_n^0 represent variational transition states, while the most prominent peaks in $\rho_{\to n'}^0$ represent supernumerary transition states. This would be consistent with the vibrationally adiabatic maxima at reactant-like geometries being less closely spaced than the maxima at product-like geometries (for $\nu_1 > 0$).

Figure 5 suggests that when both variational and supernumerary transition states influence state-selected dynamics, the former are observed primarily in ρ_n and the latter in $\rho_{\to n'}$. This is clearly true for the $[20^0]$, $S[20^0]$, $[30^0]$, and $S[30^0]$ transition states in Figs. 5g–j, and the spacing of features suggests that it is also true for bend-excited transition states in the stretch-excited manifolds. This trend is most easily understood by considering that, from the principle of time reversal invariance, quantum mechanical transition probabilities $P_{nn'}$ describe both forward ($n \to n'$) and reverse ($n' \to n$) reactions. Thus $\rho_{\to n'}$ describes both reaction *into* state n' for the *forward* reaction and *out of* state n' for the *reverse* reaction. To understand the state-selected dynamics, we consider the evolution of reactive flux associated with a single asymptotic state. Therefore we consider the forward reaction for ρ_n and the reverse reaction for $\rho_{\to n'}$. The quantity $\rho_{\to n'}$, then, tends to be influenced by dynamical bottlenecks for state n' that occur before the region of highly vibrationally nonadiabatic dynamics for the *reverse* reaction, i.e., supernumerary transition states. The quantity ρ_n, on the other hand, tends to be influenced by dynamical bottlenecks on the opposite side of the interaction region (variational transition states) because it describes reaction out of a particular state for the *forward* reaction.

Many but not all of the quantized transition states observed in the densities of state-selected reaction probability are observed as peaks in the total density of reactive states. Some highly bend excited states (e.g., $[0\ 12^0]$, and $[0\ 14^0]$) are observed as peaks only in the state-selected dynamics. If the closely spaced features in the stretch-excited manifolds for $\rho_{\to n'}^0$ are indicative of supernumerary transition states more closely spaced in energy than the variational transition states (which adiabatic transition state theory also suggests), then only some of the supernumerary transition states, in particular $S[20^0]$, $S[22^0]$, $S[24^0]$, $S[30^0]$, $S[32^0]$, $S[34^0]$, and $S[36^0]$, are observed in the total density, i.e., only some are of the first kind. The other supernumerary transition states identified in the state-selected dynamics are of the second kind.

The interpretation of the accurate quantal results in terms of variational and supernumerary transition states is consistent with model studies of scattering by unsymmetrical one-dimensional Eckart potentials (84). These studies show that both maxima in the unsymmetrical potentials are associated with poles of the scattering matrix, and some of these poles are associated with an increase in the transmission probability, while others are not.

D. Spectroscopic Constants

Spectroscopic constants for the variational transition states were obtained by a fit similar to that used for the $H + H_2$ reaction. In this case, noting that quantized transition states are associated with poles of the S matrix having the form

$$\overline{E}(\nu_1, \nu_2) = E_\tau(\nu_1, \nu_2) - i\pi W_\tau(\nu_1, \nu_2) \tag{30}$$

we fit both the energies and the widths of the quantized transition states. Equation (30) is equivalent to Eq. (26) except that it has been written in terms of the width parameter W_τ instead of the resonance width Γ (from Eqs. (12), (26), and (28) with ν set to zero, $\Gamma = 2\pi W_\tau$). A least-squares fit of the first six $O + H_2$ levels was made using Eqs. (25) and (30), allowing the spectroscopic parameters to be complex. We constrained x_{11} to be zero because none of the first six states involve $\nu_1 > 1$. The parameters thus obtained are compared with those obtained by adiabatic transition state theory. The latter were calculated with an analogous least-squares fit in which the real parts of the resonance energy were the maxima in the vibrationally adiabatic curves at reactant-like geometries, and the imaginary parts were obtained from tunneling probabilities for a parabolic approximation to the vibrationally adiabatic curves near their maxima (14).

Table 7 shows that the agreement between the accurate results and adiabatic-transition state theory is quite good for the real parts of E_0, ω_1, and ω_2. The imaginary parts do not match as closely, but the imaginary parts of four of the five spectroscopic constants agree in sign, and in three cases they agree within a factor of about 2.

VI. D + H_2

We have also calculated the density of reactive states for the $D + H_2$ reaction. These calculations were carried out as part of a converged calculation of the thermal rate constant for the reaction $D + H_2 \rightarrow HD + H$ over a wide range of temperatures (64). We found in these calculations that rate constants calculated using either the DMBE potential energy surface discussed above or the earlier so-called LSTH potential energy surface (114–116) were in excellent agreement with experiment. In particular the average deviation from experiment (117) over the 250–900 K range is only 5% for both surfaces, which is within the experimental error bars.

Not only the rate constants but also the densities of reactive states are very similar for these two potential energy surfaces; hence we will concentrate here on surveying the results for only one of these surfaces. We arbitrarily chose the LSTH surface for this

Table 7 Spectroscopic Constants (cm^{-1}) for $O + H_2$, $J = 0$

	Accurate	Adiabatic transition state theory
E_0/hc	$3786 - 597i$	$3945 - 971i$
ω_1	$2241 + 507i$	$2326 + 520i$
ω_2	$737 - 307i$	$929 + 75i$
x_{12}	$-45 - 89i$	$-266 - 245i$
x_{22}	$-2 + 43i$	$24 + 88i$

purpose. In the rest of this section we present an analysis of the role of quantized transition states in the accurate quantal dynamics of the D + H$_2$ reaction on this surface. We will present results for total angular momenta J = 0, 3, 9, and 15 with H$_2$ spatial permutation symmetry (S) equal to +1; we show results for parity (P) equal to +1 with J = 0 and 3 and for P = −1 with J = 3, 9, and 15.

First of all we note that the S = +1 and S = −1 symmetry blocks yield almost identical CRPs (64), and this is why we present the results only for S = +1. The density spectrum for D + H$_2$ with *JPS* = 0++ is shown as the solid curve in Fig. 6. The heavy dashed curve is the simulated spectrum obtained by fitting the quantal density by a sum of terms as in Eqs. (14) and (15), corresponding to scattering by parabolic barriers. In order to achieve a physical fit we used 13 terms and constrained five of the κ_τ to be equal unity; the resulting fit is quite good. We conclude that quantized transition states control the chemical reactivity globally. As before we label the levels of the transition state as [$v_1 v_2^K$]. For J = 0 only the even-bend states contribute to the CRP. Assignments [$v_1 v_2^K$] were made on the basis of semiclassically computed vibrationally adiabatic potential maxima and the expected uniformity of the spacings between fitted threshold energies in a given v_1 or v_2 progression. The assignments are shown also in Fig. 6. We found evidence for significant influence on the CRP by nine variational transition states and two supernumerary transition states of the first kind at energies below 1.5 eV. Supernumerary transition states in the v_1 = 2 stretch manifold influence this unsymmetric reaction, just as for O + H$_2$. The parameters obtained for D + H$_2$ are shown in Table 8 and may be compared with those for H + H$_2$ in Table 2.
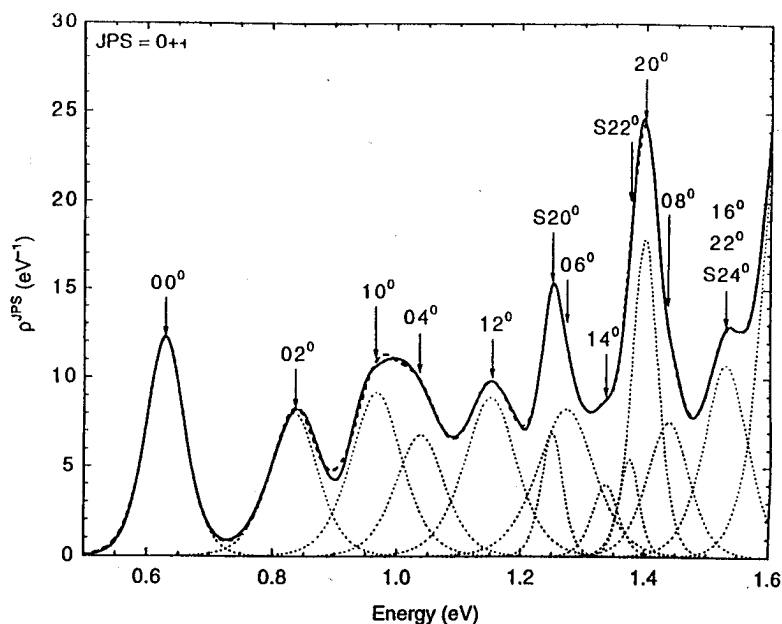
Figure 6 Density of reactive states for D + H$_2$ with *JPS* = 0++. The components of the fit are shown as dashed curves, and the assignments are shown above the peaks in the fit. The heavy dashed curve is the sum of the terms in the fit, and the solid curve is the accurate quantal density of reactive states.

Table 8   Quantized Transition States for D + H_2, $J = 0$

Assignment	E_τ (eV)	W_τ (10^{-2} eV)	κ_τ (eV)
[00°]	0.630	2.04	1.00
[02°]	0.835	2.51	0.81
[10°]	0.967	2.72	1.00[a]
[04°]	1.038	2.59	0.71
[12°]	1.150	2.81	1.00[a]
S[20°]	1.250	1.14	0.32
[06°]	1.273	3.02	1.00[a]
[14°]	1.336	1.39	0.22
S[22°]	1.375	1.05	0.23
[20°]	1.400	1.39	1.00[a]
[08°]	1.438	2.22	0.67
[16°], [22°], S[24°]	1.529	2.32	1.00[a]
S[30°]	1.627	2.17	2.84[b]

[a]Constrained to 1.00.
[b]Includes contributions from higher-energy quantized transition states.

Using the E_τ values from Table 8 for the variational transition states [00°], [02°], [04°], [10°], [12°], and [20°] with $J = 0$, and using the positions of the peak maxima for the [00°] states with $J = 3$ and 15, we obtain spectroscopic constants via fits of the threshold energies to Eq. (25), augmented by an extra term, $-DJ^2(J + 1)^2$. The spectroscopic constants obtained are given in Table 9. These constants predict threshold energies for the [06°], [08°], and [14°] transition states that differ, on average, by only 0.014 eV from the fitted values of E_τ. The value of the rotational constant B is in excellent agreement with the value of 7.04 cm^{-1} obtained from the semiclassical (76) analysis. There is also qualitative agreement between these constants and those [10,16] for H + H_2, given in Sec. IV.A, after taking into account the different reduced masses of the system.

Figure 7 shows the densities of reactive states for $JPS = 0++, 3++, 3-+, 9-+$, and $15-+$. On each plot we tabulate the energies in eV of the variational transition states predicted by the parameters in Table 9 along with the assignments; and we also list the cumulative reaction probability $N^{JPS}(E)$, summed over both HD product arrangements, at each local minimum. Transition states with $K = 0$ appear only for $(-1)^J P =$

Table 9   Accurate Spectroscopic Constants (cm^{-1}) for D + H_2 Transition States[a]

ω_1	2047
ω_2	882
x_{11}	383
x_{12}	−89
x_{22}	−2
B	7.556
D	0.002

[a]$E_0 = 0.388$ eV.
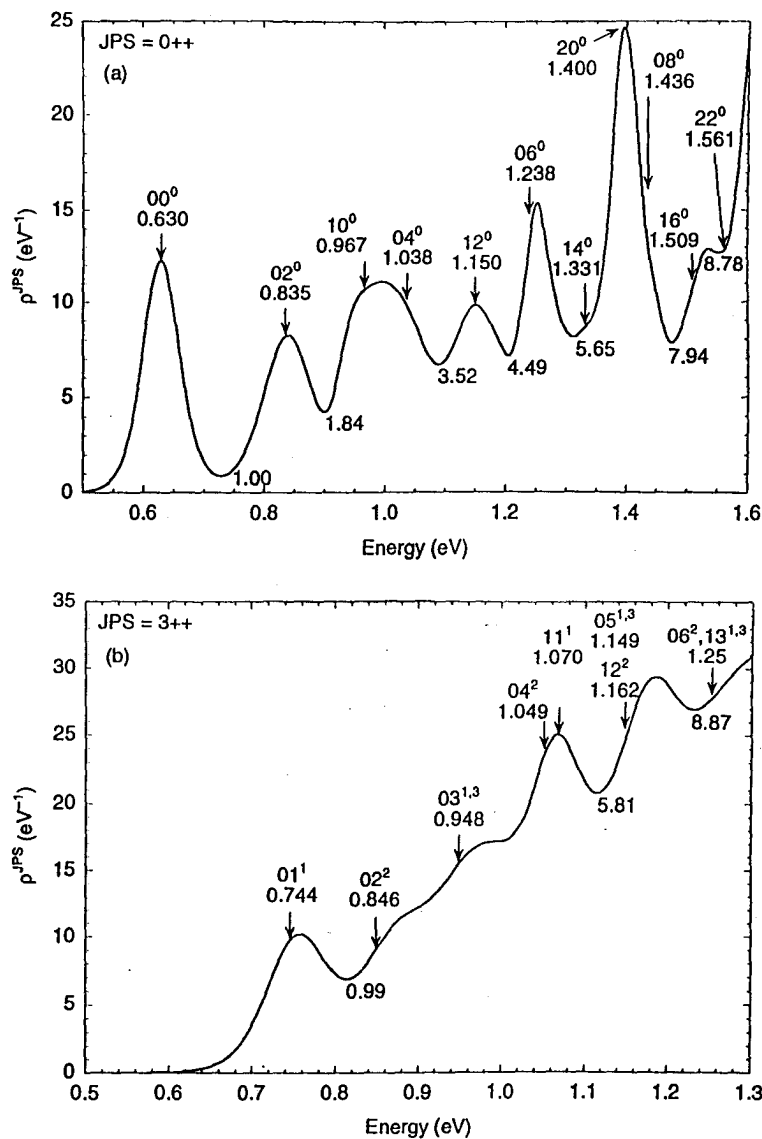
Figure 7 Densities of reactive states $\rho^{JPS}(E)$ for D + H$_2$ with $S = +1$. (a) $J = 0$, $P = +1$. (b,c) $J = 3$, $P = \pm1$. (d) $J = 9$, $P = -1$. (e) $J = 15$, $P = -1$. The positions of the variational transition states predicted by the spectroscopic fit are indicated, labeled by their assignments and by their energies in eV, and the local minima of N^{JPS} are labeled by the values of the CRP.

+1, and in particular they are not present in the *JPS* = 3++ spectrum, whereas the *JPS* = 3−+ spectrum has contributions from both zero and nonzero *K*, based on symmetry arguments given in Sec. IV.B.

The first and most important point that we wish to make on the basis of Fig. 7 is that the quantized transition state structure persists up to high *J*, despite the increasing density of states due to *K* degeneracy. This answers affirmatively the most widely asked
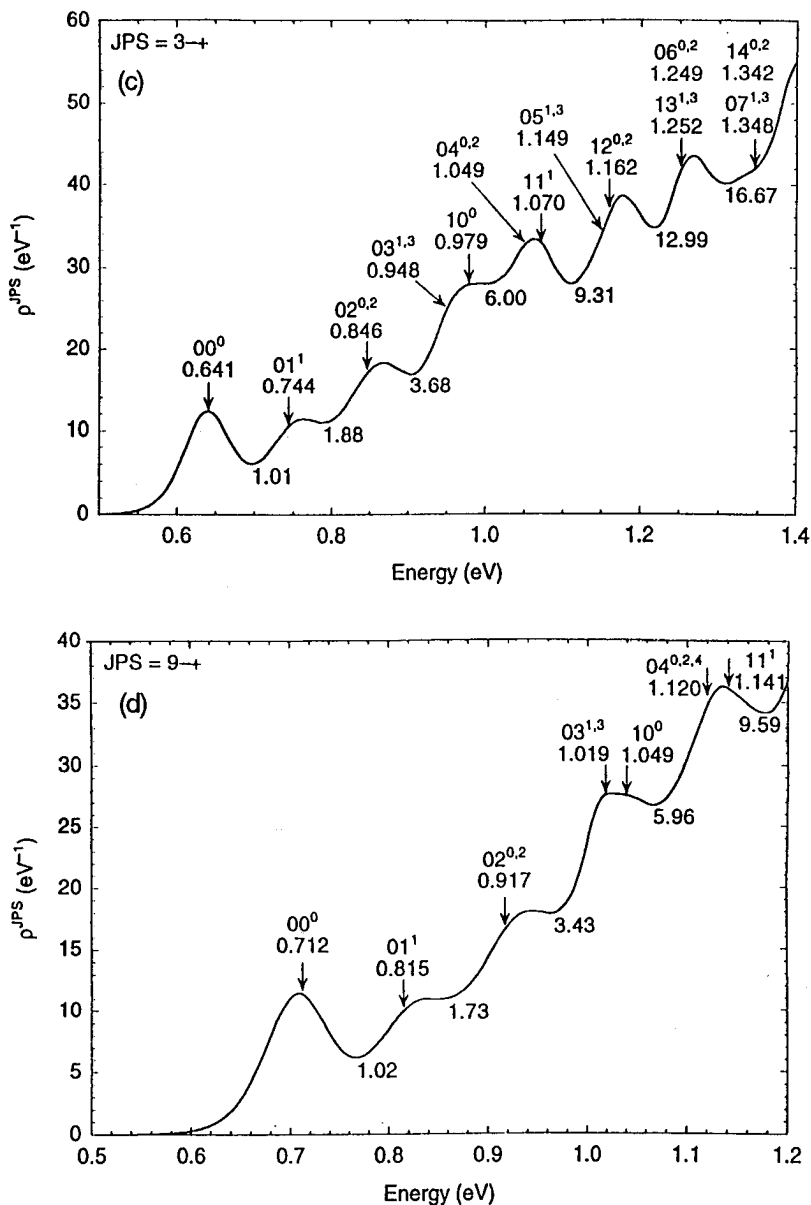
Figure 7 Continued.

question we hear at seminars if we concentrate on low-J examples, namely, can quantized transition state structure be observed at high J?

The values of the CRP at the local minima are a somewhat crude (compared to fitting with the correct line shape) way to estimate the sum of the transmission coefficients of all levels below a given local minimum. In the typical cases with $J = 0-15$, the CRP at the first local minimum is in the range $0.99-1.02$. Thus the first transition state, $[00^0]$, is almost always a nearly ideal dynamical bottleneck. The bend states are roughly equally
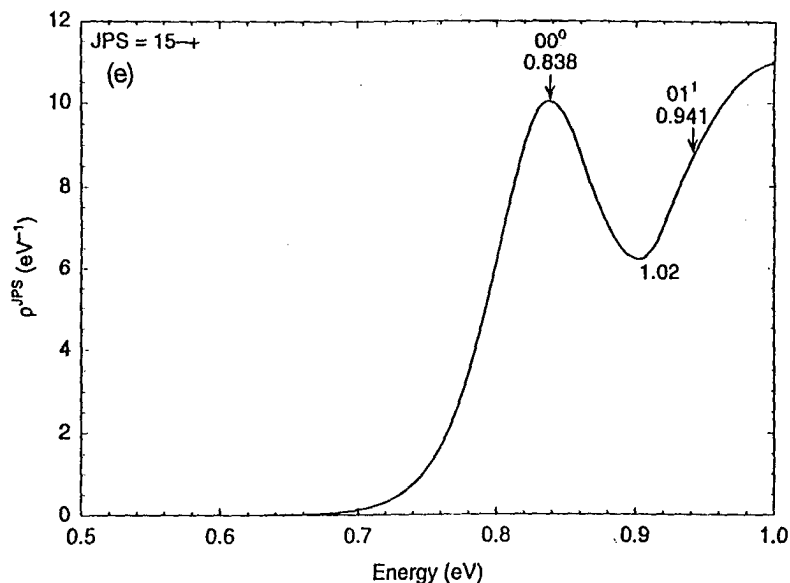
Figure 7 Continued.

spaced in energy. The quantized transition state structures at higher energy are relatively broad and tend to overlap, especially at higher values of J where the different K states can broaden the feature associated with a given v_1 and v_2.

Examination of state-selected CRPs for this system (not shown here) indicates that the various initial states can each access several transition states, although some specificity is observed. Much of the state-selected dynamics clearly correlates with the total dynamics. For example, the state-selected densities for various j with $v = 0$ have prominent peaks at 0.63, 0.84, and 1.03 eV, while those for $v = 1$ have prominent peaks at 0.96 and 1.16 eV.

VII. F + H₂

The observation of quantized transition states in H + H₂ and D + H₂, as discussed in Sec. IV and VI, builds on a long history of the development of theoretical concepts for which these reactions have provided critical early examples (118). The reaction of F with H₂ is another reaction whose detailed understanding has been the subject of many studies over a long period of time. In particular, it is a prototype exothermic chemical reaction, and it has played an important role (119–126) in our appreciation for resonance-phenomena. Although resonances were observed theoretically in the H + H₂ reaction many years ago (118), resonance effects have been hard to observe experimentally for bimolecular reactions. The F + H₂ reaction, though, showed a dependence of the angular scattering pattern on the vibrational quantum number v' of the HF product that was hard to interpret unless resonance behavior was invoked. In particular, Neumark et al. (125) concluded that "when contrasted with the strong backscattering of HF ($v' = 2$) in the reaction F + p-H₂ at 1.84 kcal/mol (0.080 eV relative translational energy, which corresponds to 0.348 eV total energy for $j = 0$) the sharp forward peak of the $v' = 3$ product

is the most compelling evidence to date for quantum mechanical dynamical resonance effects in reactive scattering. The shape of the distribution is what one expects when collisions at relatively high impact parameters contribute to the formation of a quasi-bound state followed by selective decay to $v' = 3$ products.'' Early attempts to explain the phenomenon were hindered by incomplete knowledge of the potential energy surface and an inability to perform converged quantum dynamical calculations.

One of the major impediments to understanding the dynamics has been the lack of an accurate potential energy surface, and in fact even the barrier height and saddle point geometry, which are two of the most basic properties of a potential energy surface for a reactive system, have been controversial. Recently, though, three quite different sets of electronic structure calculations (127–131) have converged on similar results for these properties. Furthermore both sets of calculations predict that the bending potential for the saddle point is very soft, and the saddle point may even be (probably is) nonlinear. A global potential energy surface that embodies these new predictions was created and fine tuned by an iterative process involving repeated converged quantum dynamics calculations (126). The new surface is called 6SEC.

Well-converged quantum dynamics calculations were first reported for the $F + H_2$ reaction (for $J = 0$ on an inacccurate potential surface) in 1989 (132), and a combination of large-basis-set electronic structure calculations (127–129), variational transition state theory calculations (126,129), and modifications based on accurate quantum scattering calculations (126) with $J = 0–18$ were used in 1993 to calibrate the 6SEC (126) potential energy surface. Accurate quantum dynamics calculations with $J = 0–21$ (126) give a remarkably realistic reproduction of the energy-dependent experimental (125) angular scattering patterns for the $F + H_2$ reaction for both $v' = 2$ and $v' = 3$, whereas calculations based on intermediate surfaces in the iterative surface fitting process often were very inaccurate for these features due to their inaccurate prediction of high-J resonances ($J \cong$ 12–17), which are sensitive tests of surface quality.

Interest in this system is further heightened by photoelectron spectra of FH_2^- in which the final state is a neutral FH_2 system in the transition state region (133–135). The original interpretation (133) of these spectra was that the system made transitions to a resonance state at an energy just below a product asymptote and to continuum states in which probability density accumulated near classical turning points by Franck-Condon transitions to ''scattering wave functions with nearly zero momentum in the Franck-Condon region along the dissociation coordinate.'' The latter were called ''direct'' transitions to emphasize the nonresonant interpretation. The relationship of the observed spectrum to quantized transition states was brought out later though in the work of Kress and Hayes (136), who pointed out the similarity of the observed spectrum to the density of reactive states for the 5SEC (129) potential surface. The 6SEC surface, which is qualitatively similar to (and based on) the 5SEC one in the transition state region, also leads to qualitative agreement with experimental (133) spacings. Werner and co-workers (135), using a surface similar to 6SEC but based on ab initio electronic structure calculations, have carried out a successful direct simulation of the photoelectron spectrum (direct simulations using presumably less accurate surfaces were reported earlier (134)). In light of these results it is of great interest to present the density of reactive states for the $F + H_2$ reaction on the 6SEC surface, which reproduces the state- and energy-dependent angular distributions so well.

For $F + H_2$, we consider both symmetries S (they are calculated separately, taking advantage of the fact that S is a conserved quantum number), and we count both product

arrangements. The resulting cumulative reaction probabilities and densities of reactive states for various sets of the conserved quantum numbers J, P, and S are given in Fig. 8. The curves are labeled similarly to those for D + H_2 except that in the regions between prominent peaks and after the final prominent peak we mark the value of the CRP only at the first local minimum, not at all local minima. The obvious separation of the quantized transition states in both the CRP and density plots is very striking. The energies at the local maxima in the density plot provide a first approximation to the transition state energy levels E_τ, and, for nondegenerate levels, the differences between $N^{JPS}(E)$ at the successive local minima provide a first approximation to the transmission coefficients κ_τ. In some cases these differences are closer to 2 or 3 than to unity, and this indicates a degenerate level or a near degeneracy. In such cases the difference is an approximation to the product of the degeneracy and the average transmission coefficient of the states comprising the degenerate or near-degenerate manifold. (The energies at the local maxima in the CRP plot have no obvious meaning, and in fact it is not even clear why there are local maxima after every rise, but we labeled them for the convenience of the reader.)

The F + H_2 system is characterized by an early, loose transition state whose lowest-frequency motion is best modeled as an internal rotation, in contrast to the tight, linear transition states of the H + H_2, D + H_2, and O + H_2 reactions discussed above, whose low-frequency motion is well modeled as an anharmonic bending vibration. The lowest-energy saddle point on the 6SEC surface is bent, although it is only 0.022 eV lower in energy than the collinear transition state. The marked difference in the character of tight and loose transition states results in striking differences in the corresponding transition state spectra. The hindered-rotor transition-state levels may be labeled by the diatomic reactant's vibrational and rotational quantum numbers, denoted v and j respectively, as well as the magnitude, K, of the projection of J on the atom-to-diatom axis. The projection quantum number is constrained such that (63)

$$[1 - (-1)^j P]/2 \leq K \leq \min(j, J) \tag{31}$$

This may be called a body-frame label set. Alternatively one may use the space-frame labels v, j, and l of the initial collision pair, where l is the orbital angular momentum quantum number of the relative translational motion of FF with respect to H_2. The quantum number l is constrained by (137)

$$|j - J| \leq l \leq |j + J| \tag{32}$$

and

$$(-1)^l = P(-1)^j \tag{33}$$

Neither the (v, j, K) nor the (v, j, l) set of quantum numbers fully separates the motion at the transition state, but these representations provide a basis for discussion.

The asymptotic H_2 eigenstate energies for the 6SEC potential energy surface are given in Table 10, and they illustrate the well-known fact that the energies of pure rotor states are approximately equal to $Bj(j + 1)$, where B is the rotational constant in energy units. Examination of the peak positions in Fig. 8 shows that they fall into clusters whose mean energies are also approximately proportional to $j(j + 1)$, and we present them organized this way in Table 11. The penultimate column of Table 11 displays the internal rotational excitation energies of the extreme energies of each cluster, and we see that they differ from the rotational excitation energies of H_2 in Table 10 by 25–36% for $j = 1$, 13–14% for $j = 2$, and less than or equal to 4% for $j = 3$ and 4. We conclude that
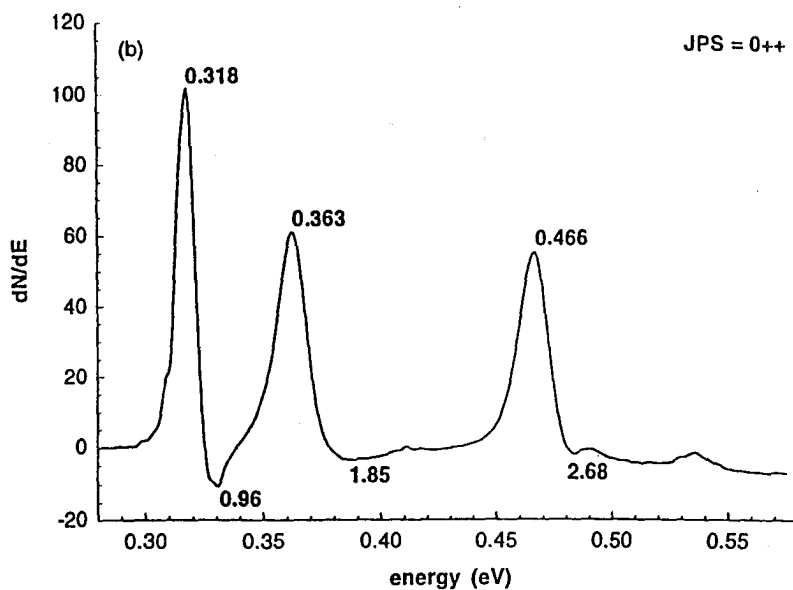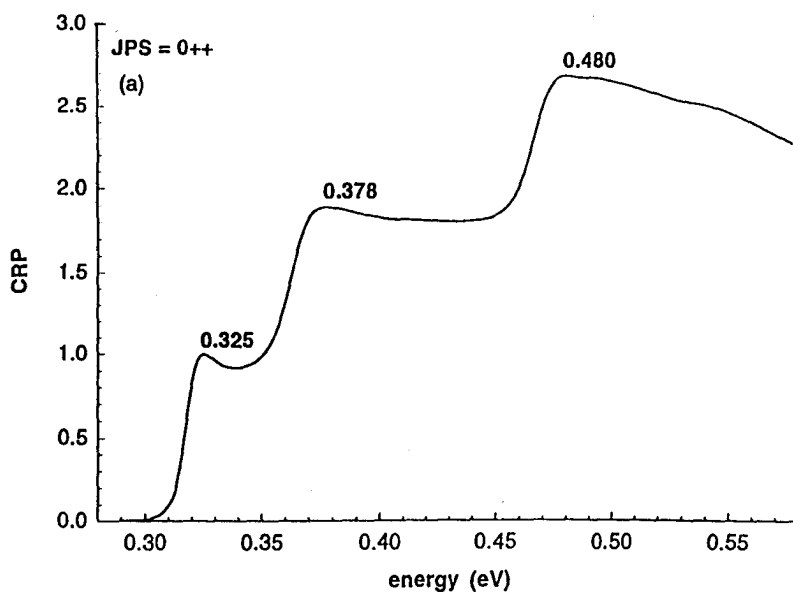
Figure 8 Cumulative reaction probabilities, $N^{JPS}(E)$, and densities of reactive states, $\rho^{JPS}(E)$ in eV^{-1}, for F + H$_2$ as functions of total energy E. *JPS*: (a,b) 0++, (c,d) 0+−, (e,f) 1−+, (g,h) 1−−, (i,j) 1+−, (k,l) 1++, (m,n) 2++, (o,p) 2+−, (q,r) 2−−, (s,t) 2−+. The energies of maxima and the value of N^{JPS} at selected minima are shown.
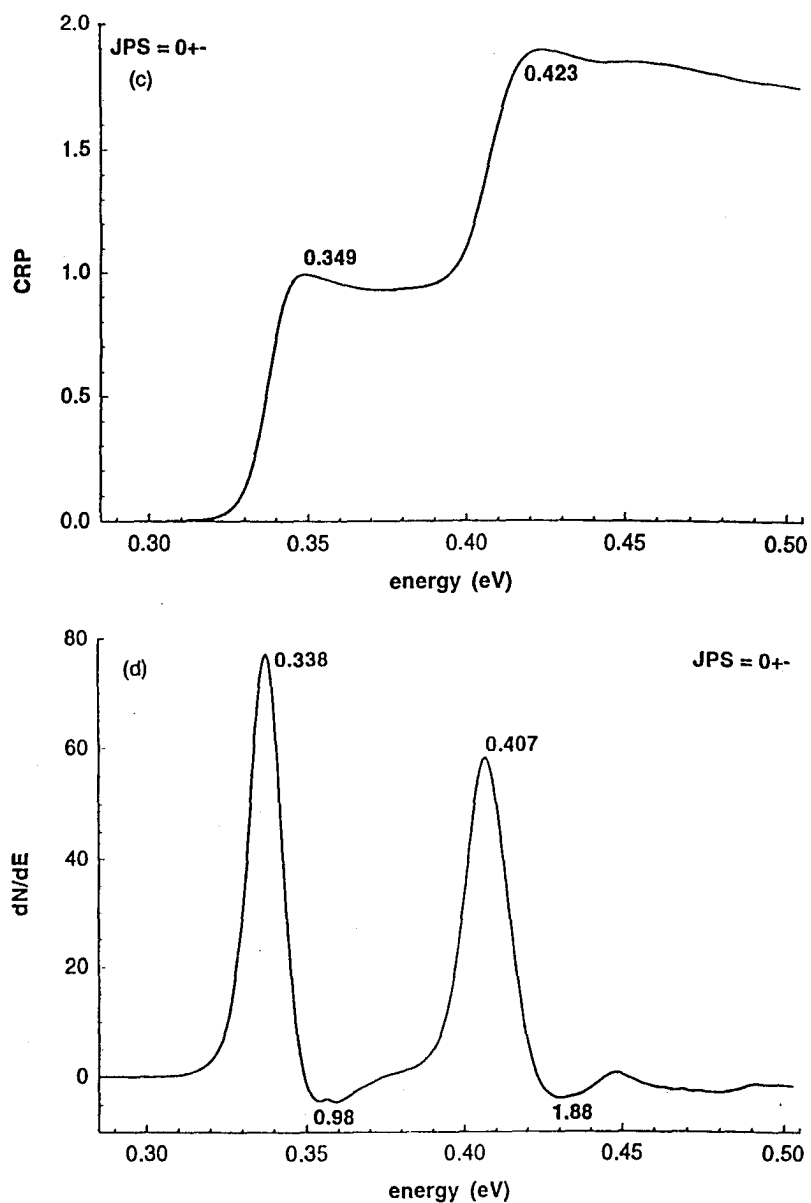
Figure 8 Continued.

because the transition states are so early, j is approximately adiabatic in the region between reactants and transition state. This allows j to be assigned as a good transition state quantum number, similar to the assignment of quantum numbers for some van der Waals complexes (138–140). Table 10 for H_2 and Table 11 for the FH_2 transition state both show the $j(j + 1)$ quadratic dependence on j. Table 10 yields $B \cong 0.0073$ eV for overall rotation of H_2, and Table 11 yields about the same value of B for internal rotation of H_2 in the FH_2 transition state.
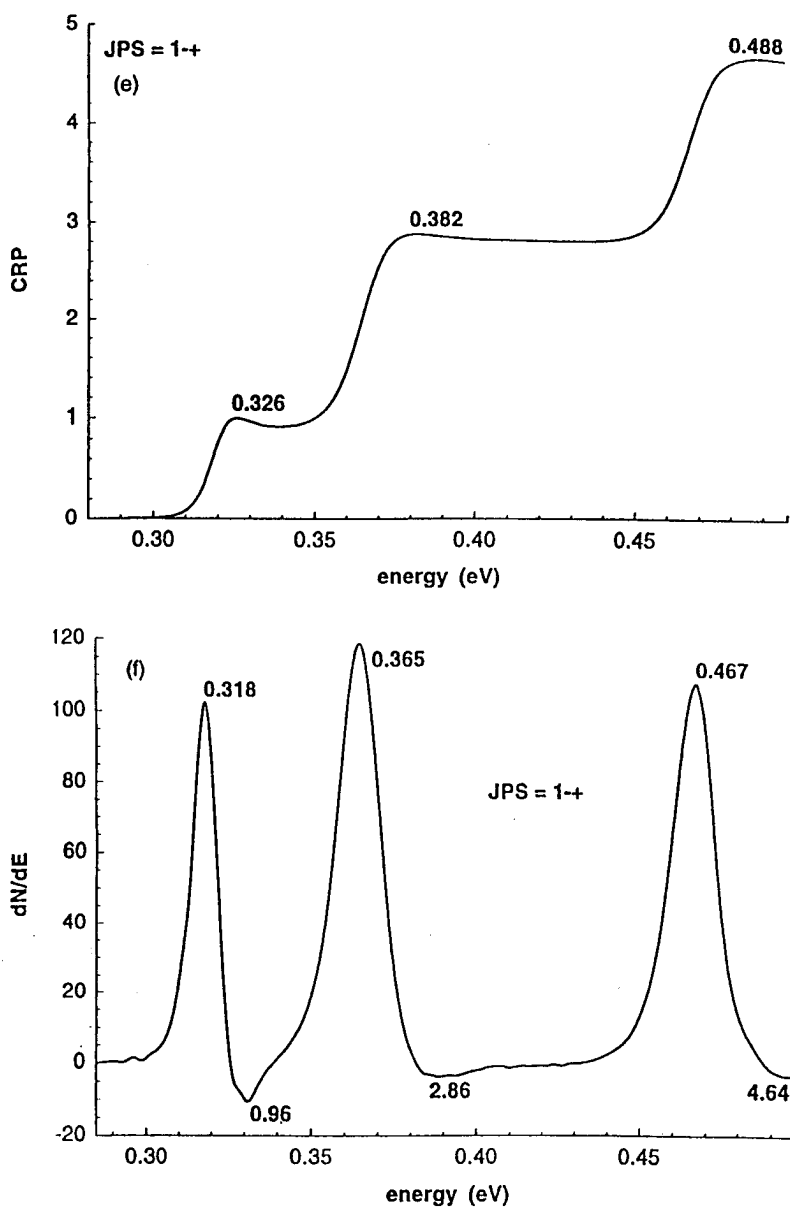
Figure 8 Continued.

In order to further categorize the transition states, we carried out eigenvalue calculations, using a method described elsewhere (141), in which we reduced the dimensionality by fixing the H—H distance at $1.44a_0$ and the F—H_2 distance at $3.17a_0$, approximately the collinear saddle point values. The eigenvalue calculations were carried out with a body-frame basis, first assuming the Hamiltonian is block diagonal in K, then coupling the K blocks. We performed such calculations with $J = 0, 1, 2, P = \pm 1$, and $S = -1$. When K was assumed to be a good quantum number, a single basis vector had
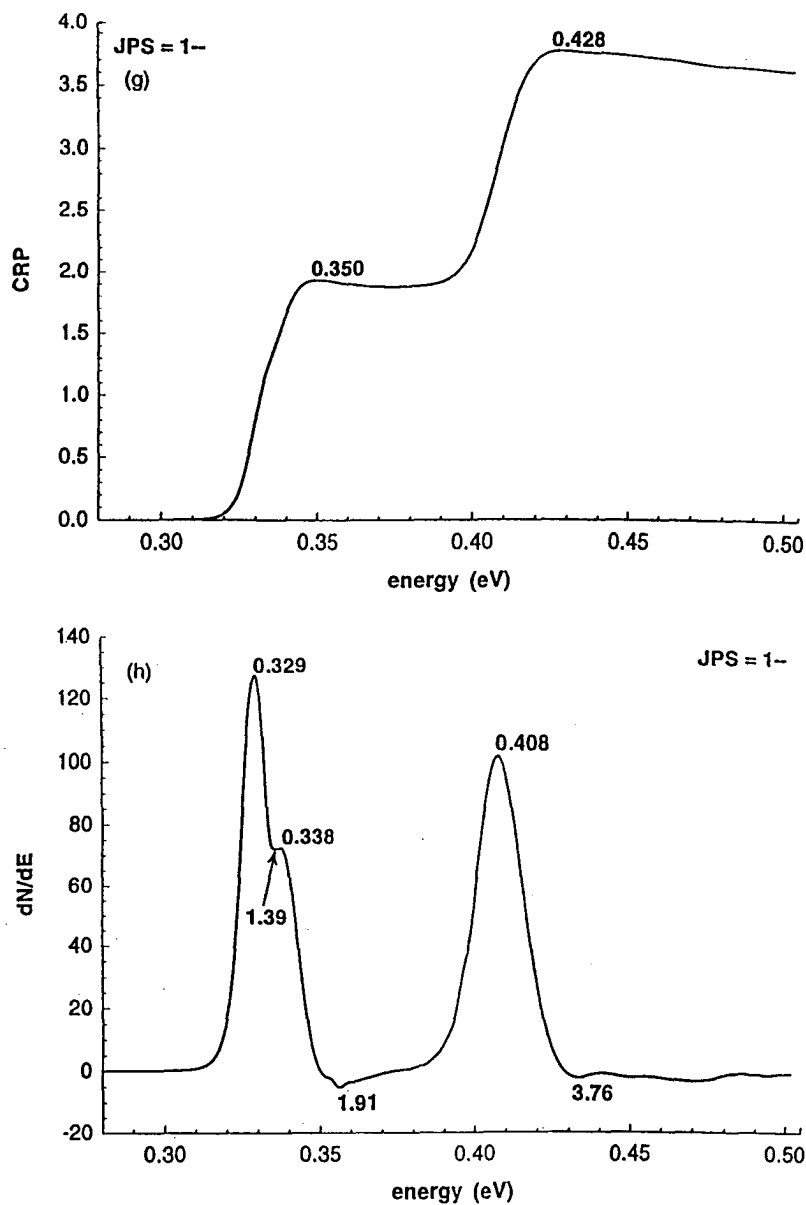
Figure 8 Continued.

a coefficient in the eigenvector greater than or equal to 0.993 in all cases, and for *JPS* = 0+− and 1+−, for which there is only one *K* value, the internal rotational excitation energies of such eigenvalue calculations agree with those in Table 11 within 1 and 5 meV. These results confirm that *j* is a good quantum number.

For *JPS* sets with more than one *K*, we then allowed the *K* blocks to couple. The coupled-*K* internal-rotation excitation energies agree with those in Table 11 with an average absolute deviation of only 7 meV, but the largest coefficient of the uncoupled eigen-
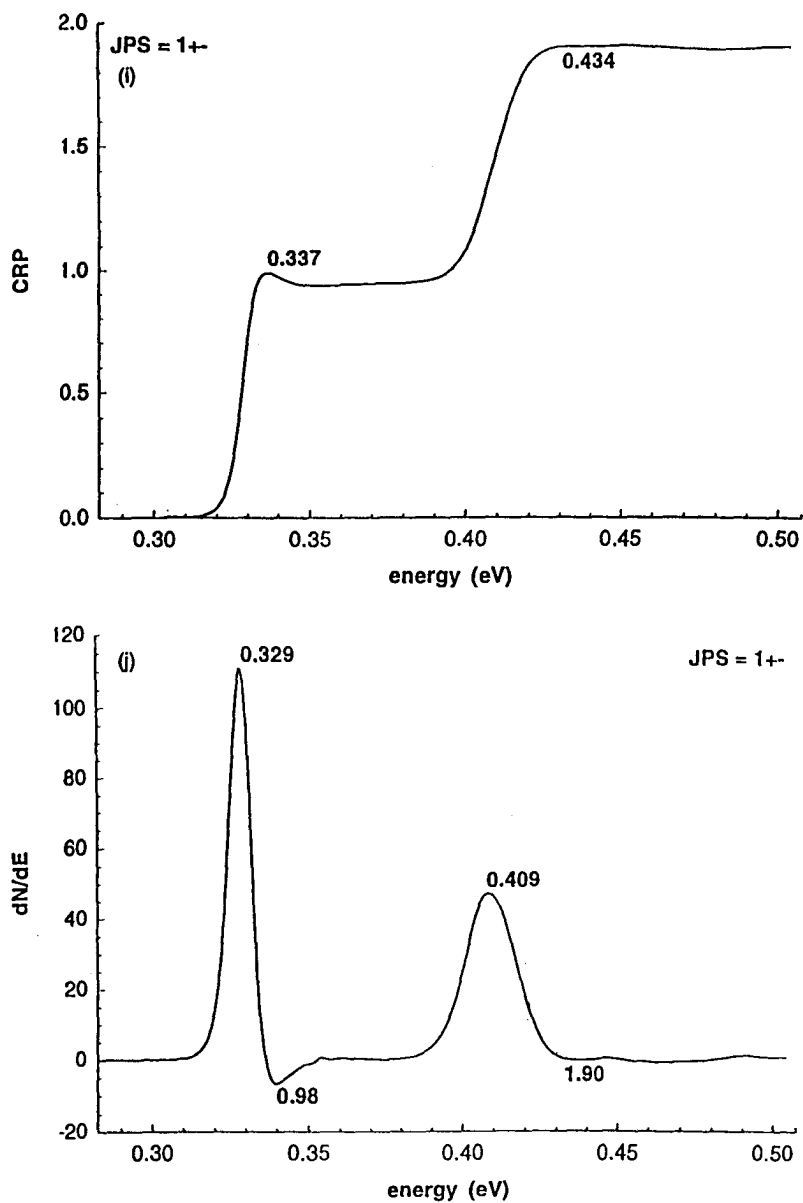
Figure 8 Continued.

states in the various coupled eigenvectors varied from 0.725 to 1.00, with an average value being 0.898, corresponding to a squared coefficient (fractional weight of the basis function in the eigenvector) equal to only 0.806 (i.e., about 81%). Thus, in general K is not a good quantum number, although for the lowest-energy state of each *JPS* block, the largest coefficient in the eigenvector is always at least 0.996. The transition state assignments resulting from this analysis are given in Table 12 (where in this case, we quote
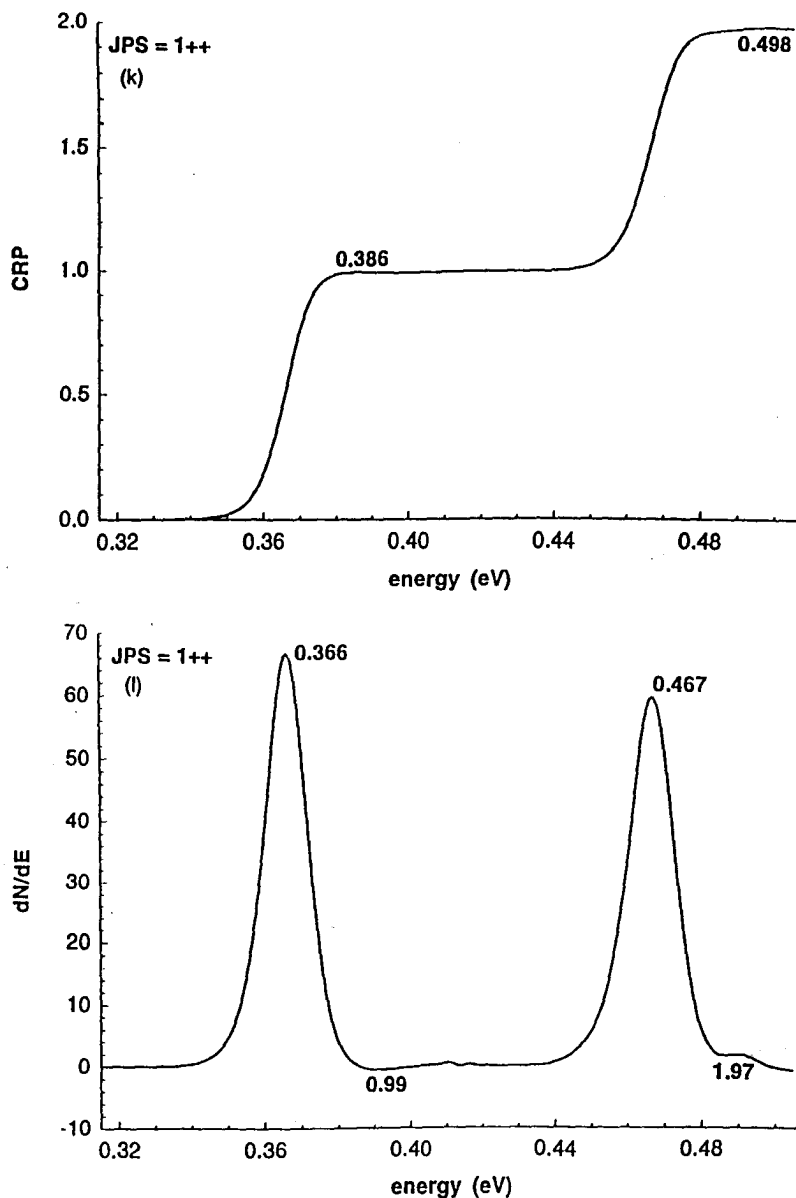
Figure 8 Continued.

the contribution in terms of primitive basis functions rather than uncoupled eigenstates), and these results confirm the j assignments of Table 11.

The levels differing only in K are typically not resolved. However, we can get an idea of the K splitting in two ways. First is the K splitting predicted by the reduced-dimensionality calculations, which is 14–15 meV for $j = 1$ and 4–11 meV for $j = 3$. Second is to look at differences in the energies at which peaks occur in the state-selected
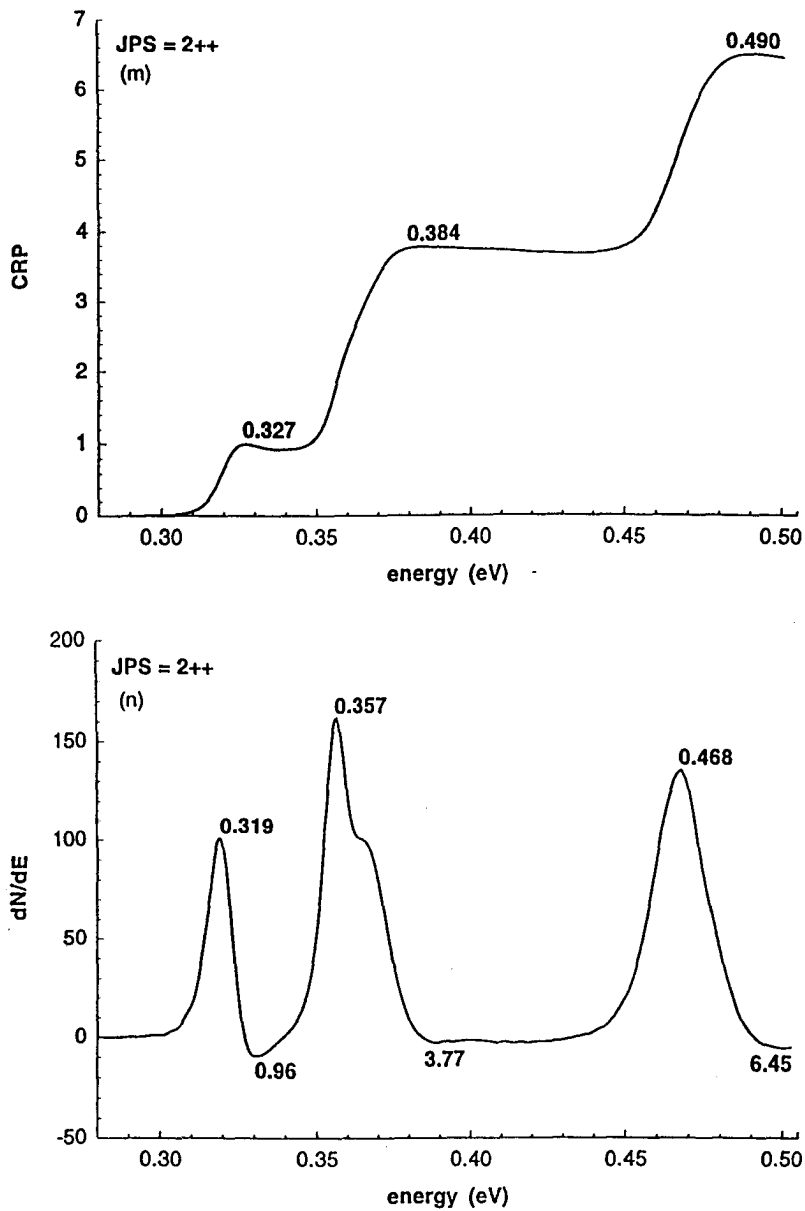
Figure 8 Continued.

densities of reactive states in the body-frame representation. The second method yields ~2–12 meV, depending on the values of J, P, S, and j, which is reasonably consistent with the first method. Since most of the peaks are broader than the estimated splittings, it is not too surprising that the K splittings are not resolved.

The transmission coefficients in the last column of Table 11 are amazing! The average deviation from unity, over 23 values, is only 5%. This is especially striking since
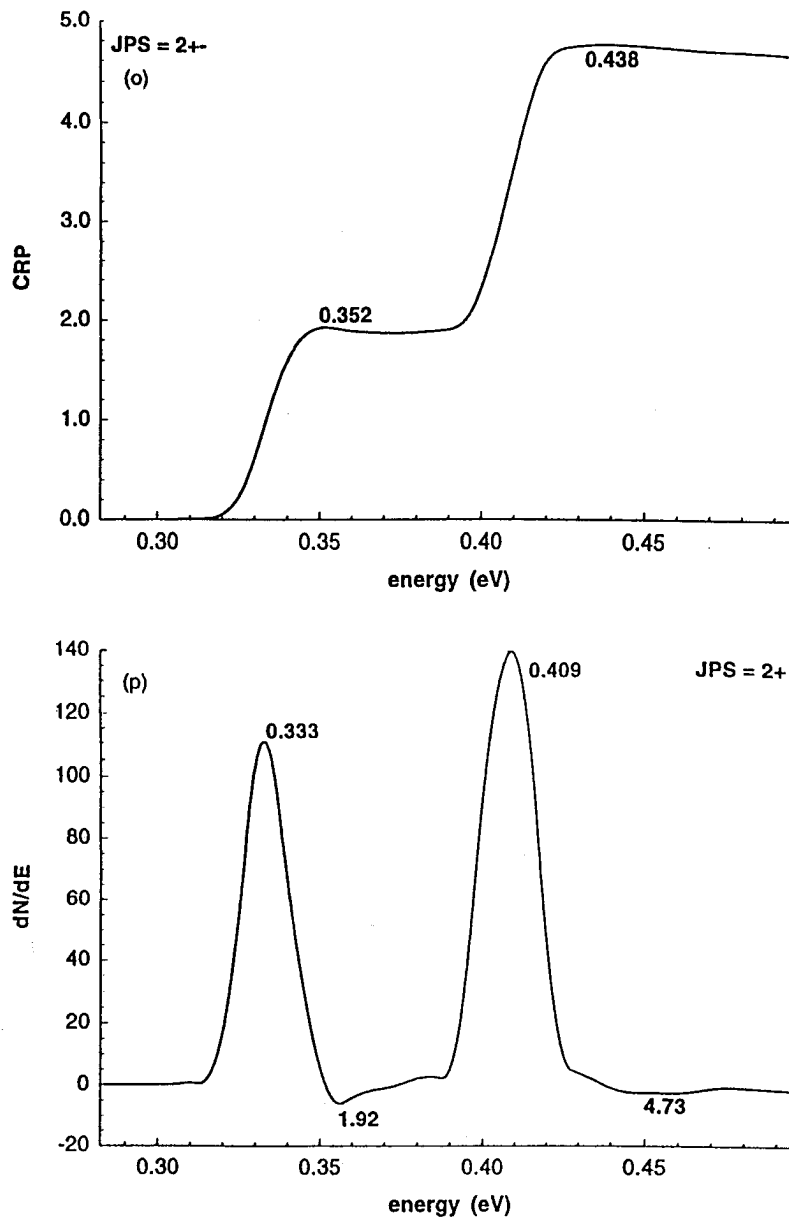
Figure 8 Continued.

the collinear $F + H_2$ reaction shows a transmission coefficient of about 0.55 averaged over a Boltzmann distribution at 300 K (142), which is by far the largest breakdown of the unit transmission coefficient assumption of any reaction studied to date, out of over 40 cases (143–146). Clearly the mechanism leading to trajectory recrossing (147) in a collinear world is not very significant in the full 3-D world.
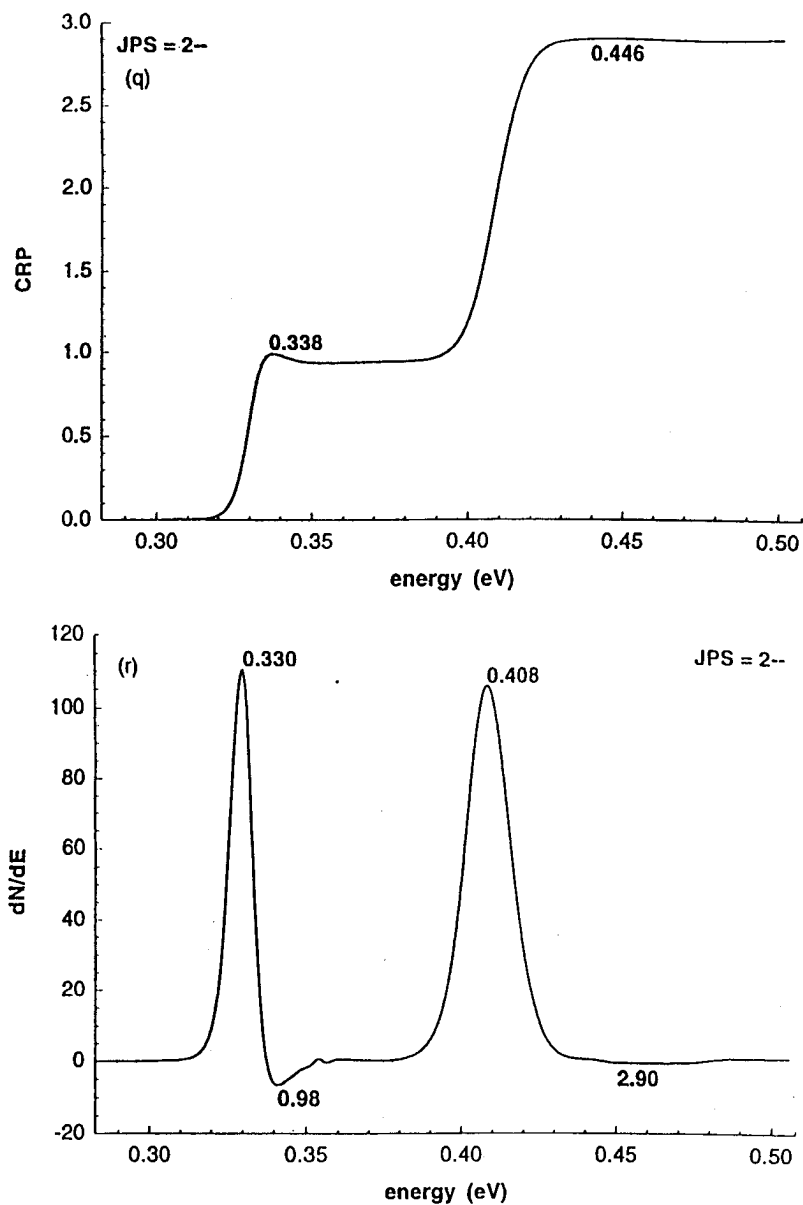
Figure 8 Continued.

VIII. HALOGEN-HYDROGEN HALIDE SYSTEMS

The hydrogen transfer reactions Cl + HCl, I + HI, and I + DI present a more difficult test of quantized transition state control of chemical reactivity. In contrast to the H + H_2, D + H_2, O + H_2, and F + H_2 reactions, the quantized transition state structure in the accurate dynamics of these reactions is almost completely obscured by features that have been attributed to trapped-state resonances and rotational thresholds (17–19). Al-
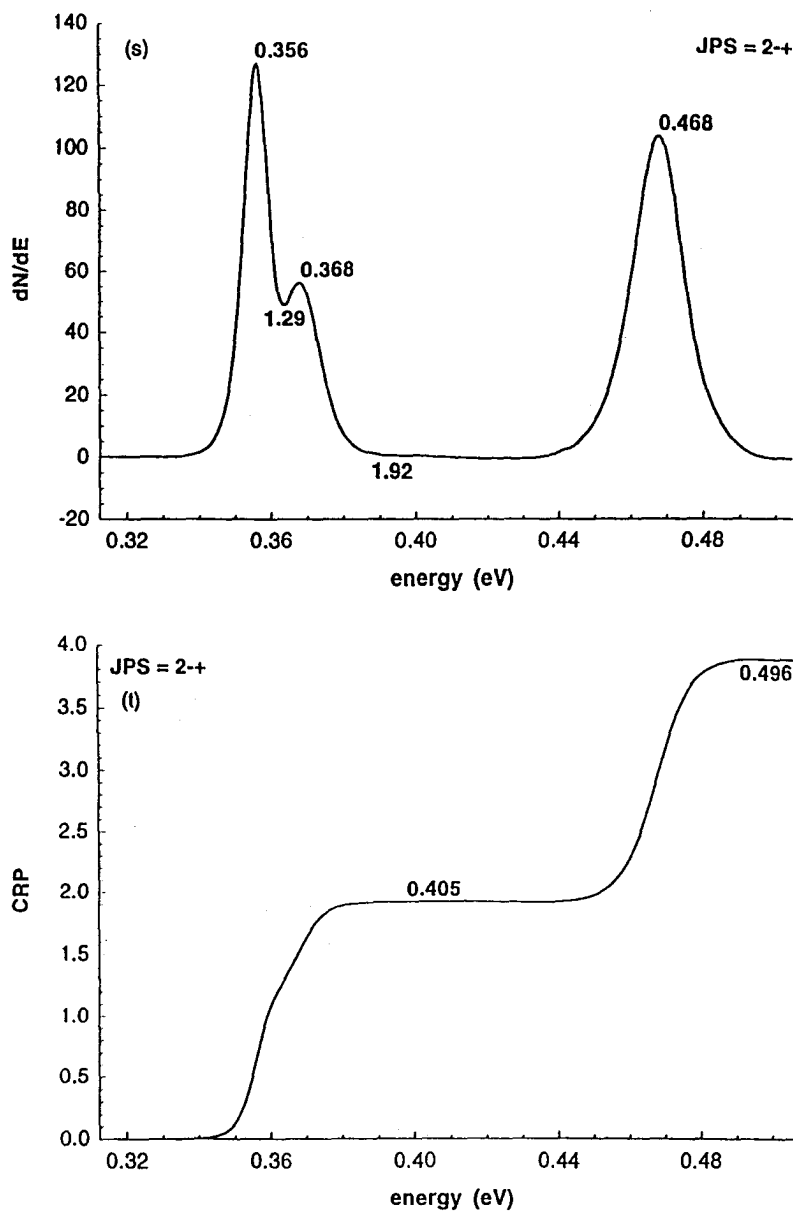
Figure 8 Continued.

though quasibound resonance features and other complicated dependencies of state-to-state reaction probabilities on energy and initial and final states are observable for the reactions discussed above, the cumulative reaction probability for these reactions is remarkably free of such structures and, as discussed above, clearly exhibits the influence of quantized transition states. This is not the case for the halogen-hydrogen halide reactions. However, as we discuss below, the influence of quantized transition states un-

Table 10 Asymptotic H_2 Eigenenergies for the 6SEC Potential Energy Surface for the FH_2 System

j	E_j (eV)	$E_j - E_0$ (meV)	$(E_j - E_0)/j(j + 1)$ (meV)
0	0.2687	0.0	—
1	0.2834	14.7	7.4
2	0.3126	43.9	7.3
3	0.3561	87.4	7.3
4	0.4135	144.8	7.2
5	0.4843	215.6	7.2
6	0.5679	299.2	7.1

Table 11 Transition State Level Assignments and Transmission Coefficients for $F + H_2$ on the 6SEC Surface

j	J	P	S	Contributing channels[a] ℓ	K	E_τ (eV)	$E_\tau - 318$ (meV)	κ_τ,b
0	0	+	+	0	0	0.318		0.96
	1	−	+	1	0	0.318		0.96
	2	+	+	2	0	0.319	0–1	0.96
1	0	+	−	1	0	0.338		0.98
	1	−	−	0,2	0,1	0.329, 0.338		0.95
	1	+	−	1	1	0.329		0.98
	2	+	−	1,3	0,1	0.333, 0.333		0.94
	2	−	−	2	1	0.330	11–20	0.98
2	0	+	+	2	0	0.363		0.89
	1	−	+	1,3	0,1	0.365, 0.365		0.95
	1	+	+	2	1	0.366		0.99
	2	+	+	0,2,4	0,1,2	0.356, 0.356, 0.363		0.92
	2	−	+	1,3	1,2	0.356, 0.368	38–50	0.96
3	0	+	−	3	0	0.407		0.90
	1	−	−	2,4	0,1	0.408, 0.408		0.93
	1	+	−	3	1	0.409		0.92
	2	+	−	1,3,5	0,1,2	0.409, 0.409, 0.409		0.94
	2	−	−	2,4	1,2	0.408, 0.408	89–91	0.96
4	0	+	+	4	0	0.466		0.83
	1	−	+	3,5	0,1	0.467, 0.467		0.89
	1	+	+	4	1	0.467		0.98
	2	+	+	2,4,6	0,1,2	0.468, 0.468, 0.468		0.89
	2	−	+	3,5	1,2	0.468, 0.468	148–150	0.98

[a]We give the labels of the contributing channels using both the space-frame and body-frame representations.
[b]For degenerate or near-degenerate clusters, κ_τ is the average transmission coefficient.

Table 12 Assignments of FH_2 Quantized Transition States[a]

			E_τ	Maximum contributor		
J	P	S	(eV)	j	K	Fraction
0	+	−	0.338	1	0	0.990
			0.407	3	0	0.988
1	+	−	0.329	1	1	0.990
			0.409	3	1	0.986
1	−	−	0.329	1	1	0.988
			0.338	1	0	0.988
			0.408	3	0	0.532
			0.408	3	1	0.531
2	−	−	0.330	1	1	0.990
			0.408	3	2	0.928
			0.408	3	1	0.918
2	+	−	0.333	1	1	0.982
			0.333	1	0	0.982
			0.409	3	2	0.854
			0.409	3	0	0.519
			0.409	3	1	0.530

[a]E_τ values from Table 11; assignments and fractional contributions based on reduced-dimensionality eigenvalue calculations.

derlies the relatively narrow structures that, at first view, are most prominent in the cumulative reaction probabilities for these reactions.

There has been considerable interest by other workers in the resonance structure of reactions of the type X + HX. Many calculations have been performed for such reactions, and it is beyond the scope of this chapter to review them all. We refer the interested reader to other sources (10,11,17–19,148–159) and mention only a few calculations in particular. Quasibound states for collinear reactions of the type X + HX were predicted on the basis of quantum mechanical scattering calculations as early as 1981 (148,150,152), and these states were related to wells in one-dimensional model potentials (148,152). Approximate three-dimensional calculations (156) employing LEPS-type potential energy surfaces (150,152) for ClHCl, IHI, and IDI also located quasibound states, which further model calculations (152,158) were useful in understanding. Accurate three-dimensional quantum mechanical scattering calculations for Cl + HCl (17), I + HI (18), and I + DI (19) were reported by Schatz in 1989. He too employed LEPS-type potential energy surfaces (150,152). The calculated CRPs exhibit an overall increase with energy, on which narrow oscillations are superimposed. The CRP for Cl + HCl exhibits a sharp feature at 0.641 eV that has been interpreted as a trapped-state resonance (17), just below the threshold for reaction of $v = 1$ vibrationally excited reactants. The I + HI and I + DI calculated CRPs also exhibit trapped-state resonance features, in both cases just below the overall threshold to reaction (18,19). On the basis of oscillations in state-selected reaction probabilities, Schatz associated the other oscillations, which occur with roughly the rotational spacing of the reactant diatom, with rotational thresholds for hindered rotor states (17–19).

Experimental evidence for the vibrational structure of XHX transition states has been provided by photoelectron spectroscopy of XHX^- anions with X = Cl, Br, and I (134,160–163). This technique, by inducing photodetachment of an electron from the XHX^- anions, probes the Franck-Condon region, which is believed for these systems to include geometries in the vicinity of the transition state region for the neutral systems. Spectral bands have been interpreted as evidence for trapped-state resonances associated with asymmetric stretch-excited levels of the transition state (160–163), and they are in general agreement with synthetic photoelectron spectra calculated from the scattering computations of Schatz (17–19). In recent experimental spectra (158,162), more closely spaced oscillations have been observed; these are apparently related to rotational thresholds as described by Schatz.

In the rest of this section we discuss our analysis (10,11) of the accurate cumulative reaction probabilities for the halogen-hydrogen halide systems that were published by Schatz (17–19). The CRPs were digitized with an optical scanner, which introduces negligible error. The accurate $N^0(E)$ was fit with cubic splines and convoluted using Eq. (20). Our analysis is based on the observation that the calculated CRPs of Schatz for Cl + HCl, I + HI, and I + DI appeared to have an overall steplike structure reminiscent of that associated with quantized transition states, underlying the narrower features associated with trapped-state resonances and rotational thresholds. Our conclusion that quantized transition states exert broad control of the chemical reactivity for these reactions is not inconsistent with Schatz's description of the narrow trapped-state resonance and rotational threshold features. These different sorts of dynamical features represent different time scales, with the shorter-time (broader) features being more closely related to the traditional concern of chemical kinetics, i.e., reactivity, as discussed below Eq. (23). The relationship of features in the CRP to features in the photoelectron spectrum is not fully worked out yet.

In 1992, Darakjian et al. (164) reported quantum dynamics calculations for the reaction He + H_2^+ → HeH^+ + H with JPS = 0++. Like the halogen-hydrogen halide reactions, this reaction exhibits a cumulative reaction probability with many narrow resonance structures, spaced about 0.005–0.01 eV apart over the entire energy range. However, it appears that these narrow structures were superimposed on a more coarsely grained, broader structure reminiscent of the steps in the cumulative reaction probability identified with quantized transition states in the H + H_2 reaction. Darakjian and co-workers (164) therefore applied an averaging procedure (165,166) to the raw cumulative reaction probability to bring out the quantized transition state structure. When they averaged over an interval of 0.01 eV, the underlying structure appeared with surprising clarity, revealing quantized transition states spaced about 0.07 eV apart. A similar treatment has identified quantized transition state influence of the reaction of Ne with H_2^+ (167–169).

The finite-resolution density of reactive states introduced in Sec. II is especially useful for analyzing the halogen-hydrogen halide reactions because, as stated above, the features due to quantized transition states are partially obscured in these systems by a number of narrow resonances associated with other regions of the potential energy surfaces. Therefore the accurate cumulative reaction probabilities $N^0(E)$ were convoluted with a Gaussian function of variable width F to obtain finite-resolution cumulative reaction probabilities $N^0(E; F)$. Analysis of $dN^0(E; F)/dE$ reveals the influence of quantized transition states underlying the narrower dynamical features of $N^0(E)$.

A. Cl + HCl

Finite-resolution ρ^0 are shown for Cl + HCl in Fig. 9. The value of F was chosen to optimize the separation of scales, smoothing over narrow features while leaving broader structure intact.

The raw $\rho^0(E)$ has many rapid oscillations that are very difficult to interpret. Convolution of $N^0(E)$ for Cl + HCl with a Gaussian having a width parameter F of 0.027 eV (corresponding to Δt = 24 fs) produces a finite-resolution CRP increasing almost monotonically with energy (11) and having clearly recognizable steplike features reminiscent of the H + H_2 and O + H_2 reactions. The corresponding density in Fig. 9 has seven well-defined features and one noticeable shoulder.

Structures suggestive of quantized transition states are discernible even in the unconvoluted $N^0(E)$. The initial rise between 0.40 and 0.45 eV is quite marked, so we assign this feature as [00°]. Since $N^0(E)$ reaches about 1 by 0.45 eV, the feature corresponds to a nearly ideal dynamical bottleneck. The rapid rise at 0.66–0.67 eV has been shown to be due to a dynamical threshold for formation of vibrationally excited v' = 1 products (157), so we assign it as [10°]. Other features in $N^0(E)$, however, are associated with different kinds of dynamical effects. For example, the sharp peak at 0.647 eV has been identified previously as a trapped-state resonance, and the broader features between 0.5 and 0.6 eV have been associated with rotational thresholds of the asymptotic diatom (17).

The influence of the remaining quantized transition states is identified on the basis of the features in the finite-resolution density $\rho^0(E;0.027)$ in Fig. 9 and the incremental
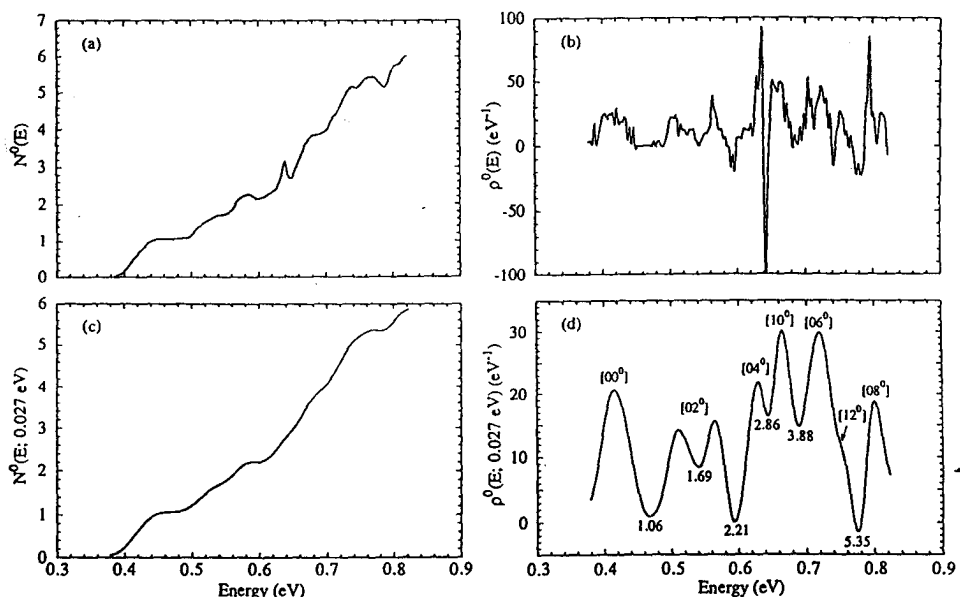

Figure 9 Original and finite-resolution densities of reactive states for the Cl + HCl reaction with J = 0. (a) $N^0(E)$. (b) $\rho^0(E)$. (c) $N^0(E$; 0.027 eV). (d) $\rho^0(E$; 0.027 eV). The value of $N^0(E; F)$ is indicated at each minimum in $\rho^0(E; F)$. (Reprinted with permission from Ref. 11, copyright 1992, American Chemical Society.)

rise in $N^0(E;0.027)$ (between the energies of minima between peaks in $\rho^0(E;0.027)$). The first peak corresponds to the initial step in $N^0(E)$ already identified as $[00^0]$; $N^0(E;0.027)$ reaches 1.06 at the minimum following it (0.416 eV). The next two peaks near 0.5 and 0.6 eV are traceable to the rotational thresholds identified in $N^0(E)$. Since $N^0(E;0.027)$ reaches 2.21 at the minimum following them (at 0.594 eV), we conclude that a single quantized transition state is predominantly responsible for the increase in reactive flux over this energy range, and so we assign both of these features as $[02^0]$. One interpretation of the fact that this transition state leads to two peaks rather than one is that there is some intermediate-time structure that is not totally removed by the 0.027-eV-wide averaging procedure. The tail of the next higher feature also contributes to the value of $N^0(E;0.027)$ at 0.594 eV.

Between 0.594 eV and the minimum at 0.775 eV, $\rho^0(E;0.027)$ exhibits three peaks and one shoulder. The peak at 0.665 eV is associated with the rapid rise in $N^0(E)$ already identified as $[10^0]$. Between the minima on either side of this peak, $N^0(E;0.027)$ rises by close to unity (from 2.86 to 3.88). The preceding peak is identified as $[04^0]$, the next even-ν_2 bend state in the ground-stretch manifold. The peak and shoulder following the $[10^0]$ feature are assigned as $[06^0]$ and $[12^0]$, respectively, on the basis of the energy spacing of bend states in the ground-stretch manifold.

Up to 0.735 eV, then, we assign six quantized transition states, and $N^0(E;0.027)$ reaches 5.35. This is in accord with the quantized transition states being good dynamical bottlenecks and exerting predominant control of the chemical reactivity. If our assignments are correct, the average transmission coefficient κ_τ for the six states up to 0.735 eV is 0.89, or 89% of its ideal value.

The remaining feature in the finite-resolution spectrum, at 0.800 eV, is more difficult to assign. On the basis of energy spacings it appears to be $[08^0]$.

It is especially interesting to note that the short- and long-time dynamics of Cl + HCl are sufficiently separated in time scale that an energy resolution of 0.027 eV washes out almost all features due to the latter in $N^0(E)$ and $\rho^0(E)$. The trapped-state resonance responsible for the 0.66–0.67 eV peak in $N^0(E)$ and the rapid oscillation in $\rho^0(E)$ is not discernible in the finite-resolution spectra. Only the broader rotational thresholds near 0.5 and 0.6 eV survive the averaging procedure. These occur on a time scale similar to that of the quantized transition states and cannot as easily be separated.

B. I + HI and I + DI

Raw and finite-resolution spectra for the I + HI reaction are shown in Fig. 10. The method of analysis (11) is similar to that used for Cl + HCl.

The raw $N^0(E)$ exhibits steplike features suggestive of quantized transition states (11). Superimposed on these are wide oscillations which have been identified with rotational thresholds. The corresponding derivative curve shows many rapid oscillations that are difficult to interpret.

In the finite-resolution spectra with a resolution function of 0.027 eV, the rapid oscillations are washed out, as illustrated in Fig. 10. The difference in time scale between the rotational thresholds and the quantized transition states for I + HI is sufficient to separate them with an appropriate resolution function. A vibrationally adiabatic analysis of I + HI predicts the $[10^0]$ threshold at 0.422 eV, which is beyond the energy scale of Fig. 10. Therefore we assign all the features in the finite-resolution density in Fig. 10 to the ground-stretch manifold. By the minimum of $\rho^0(E;0.027)$ at 0.357 eV, $N^0(E;0.027)$
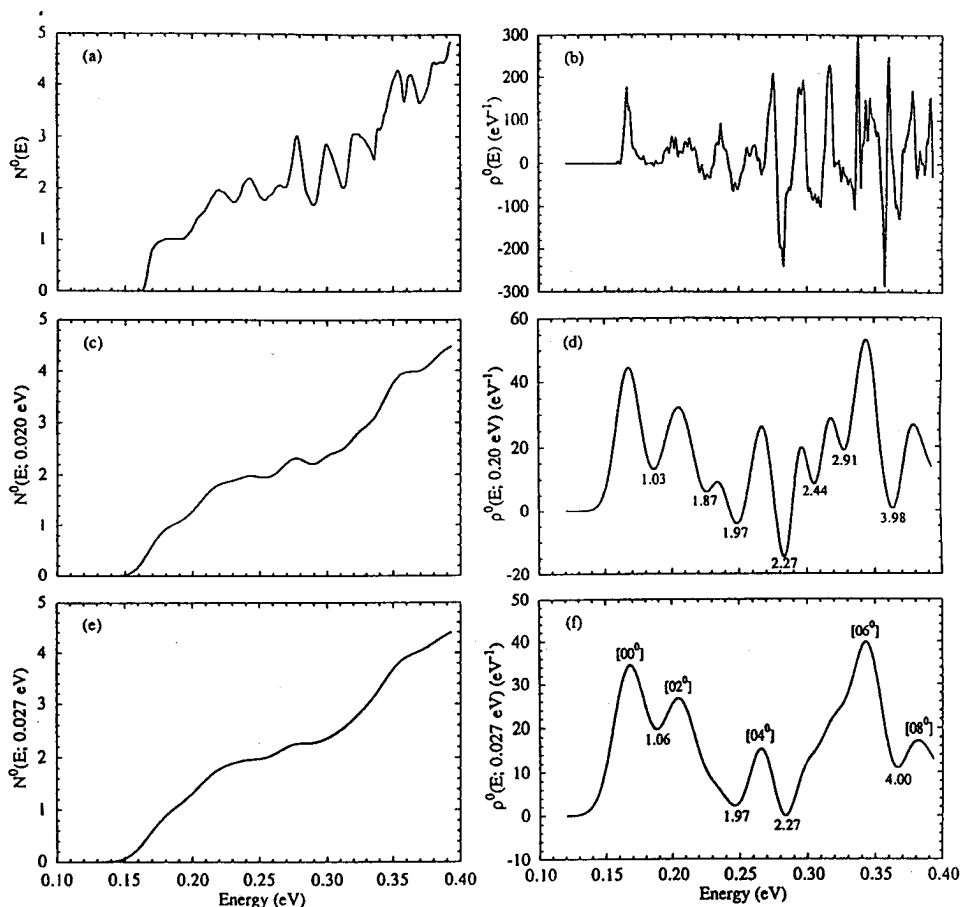
Figure 10 Original and finite-resolution densities of reactive states for the I + HI reaction with $J = 0$. (a) $N^0(E)$. (b) $\rho^0(E)$. (c) $N^0(E; 0.020 \text{ eV})$. (d) $\rho^0(E; 0.020 \text{ eV})$. (e) $N^0(E; 0.027 \text{ eV})$. (f) $\rho^0(E; 0.027 \text{ eV})$. The value of $N^0(E; F)$ is indicated at each minimum in $\rho^0(E; F)$. (Reprinted with permission from Ref. 11, copyright 1992, American Chemical Society.)

reaches 4.00. We identify four quantized transition states ([00^0], [02^0], [04^0], and [06^0]) with the four peaks in this range. Thus the four lowest-energy quantized transition states for this reaction gate the flux with apparent unit efficiently (i.e., $\kappa_\tau = 1$), exerting dominant control of the dynamics.

The analysis for I + DI is very similar to that for I + HI and Cl + HCl. With an energy resolution of 0.025 eV, seven quantized transition states were identified up to 0.42 eV, and the average value of κ_τ was 0.8 (11).

C. Spectroscopic Constants for Halogen-Hydrogen Halide Systems

Quantal spectroscopic constants, as defined in Eq. (25), were calculated for the three reactions from fits to assigned peak energies in the finite-resolution density. Vibrationally adiabatic thresholds (the maxima in vibrationally adiabatic curves calculated using the procedure described for H + H$_2$) were also least-squares fit with Eq. (25). Results are

Table 13 Spectroscopic Constants of ClHCl, IHI, and IDI Quantized Transition States

	E_0 (eV)	ω_1 (cm^{-1})	ω_2 (cm^{-1})	x_{22} (cm^{-1})	x_{12} (cm^{-1})
ClHCl					
quantal	0.231	2010	497	−11.2	
adiabatic	0.271	1920	671	17.4	−269
IHI					
quantal	a	a	235		
adiabatic	6.65(−3)[b]	2200	253	26.8	−154
IDI					
quantal	8.80(−3)	1560	230		
adiabatic	1.72(−2)	1450	192	14.2	−78.5

[a] $E_0 + 0.5hc\omega_1 = 0.139$ eV $= 1124$ cm^{-1}.
[b] (-3) indicates 10^{-3}.

in Table 13. In general, the quantal and adiabatic values for ω_1 and ω_2 are in good agreement. They differ by 5% (ω_1) and 30% (ω_2) for Cl + HCl, 8% (ω_2) for I + HI, and 7% (ω_1) and 17% (ω_2) for I + DI. (We did not obtain a value for ω_1 for I + HI.) The good agreement of the accurate and adiabatic values supports the quantized transition state assignments for features in the finite-resolution density.

We note that vibrationally adiabatic treatment yields a large magnitude of x_{12} for Cl + HCl, in particular, $x_{12} = -269$ cm^{-1}. This is a consequence of the transition state geometries. The ground-stretch thresholds are at the symmetric saddle point, but the stretch-excited thresholds are displaced toward the asymptotic species. The bending frequencies for these different structures are expected to be quite different, resulting in a large magnitude for x_{12}.

The Cl + HCl quantized transition states have also been studied by Cohen et al. (159), using semiclassical transition state theory based on second-order perturbation theory for cubic force constants and first-order perturbation theory for quartic ones. Their treatment yielded $\omega_1 = 339$ cm^{-1} and $\omega_2 = 508$ cm^{-1}. The former is considerably lower than the values extracted from finite-resolution quantal densities of reactive states and from vibrationally adiabatic analysis, 2010 and 1920 cm^{-1} respectively (11), but the bend frequency ω_2 is in good agreement with the previous (11) values, 497 and 691 cm^{-1} from quantum scattering and vibrationally adiabatic analyses respectively. The discrepancy in the stretching frequency is a consequence of Cohen et al. using second-order perturbation theory in the vicinity of the saddle point rather than the variational transition state. As discussed elsewhere (88), second-order perturbation theory is inadequate to capture large deviations in position of the variational transition state from the saddle point.

IX. OTHER SYSTEMS

A. Rare Gas + H$_2^+$: Theory

Darakjian et al. (164) computed accurate densities of reactive states for He + H$_2^+$ → HeH$^+$ + H with $J = 0$. The raw CRP exhibited many rapid oscillations, indicative of narrow trapped-state resonances. By averaging the cumulative reaction probability for

the even spatial permutation symmetry block over a range of 0.02 eV, they obtained a cumulative reaction probability exhibiting four steplike features up to 1.30 eV that were interpreted as quantized transition states. Each of these steps was approximately unity, suggesting that quantized transition states functioning as good dynamical bottlenecks underlie the narrow, trapped-state resonances. Further analysis was provided by Klippenstein and Kress (165); and their density of reactive states (a derivative of an averaged CRP), summed over both symmetry blocks, also shows four clear peaks up to 1.30 eV, and seven peaks (and three shoulders) up to 1.50 eV. The variational transition states in this system are far out in the exit valley, and, as a result, the energy spacings of the steps correlate with product rotational energy spacings.

Kress (167) reported the first converged quantum results for the reaction Ne + $H_2^+ \rightarrow NeH^+$ + H with $J = 0$. He observed six steps in an averaged cumulative reaction probability and six peaks in the density of reactive states. The spacing is fairly constant and is the range 0.05–0.08 eV. In a follow-up paper (168), Kress and Klippenstein assigned all six states and discussed statistical corrections to variational transition state theory associated with supernumerary transition states. Further analysis and discussion was provided by Kress et al. (169).

B. H + O_2: Theory

Pack and co-workers (166,170) calculated cumulative reaction probabilities for the combustion reaction H + $O_2 \rightarrow$ OH + O with zero total angular momentum. The raw CRP has many narrow resonance features. When the CRP was convoluted with Gaussians, however, the resonance features were sufficiently smoothed that the resulting CRP shows steplike features that the authors interpreted as possibly representing quantized transition states. They noted in particular that the positions and spacings of the steps correspond well with some effective potential barriers in the exit valley. Further calculations on this system were reported by Leforestier and Miller (171). Their CRP curve agrees qualitatively with that of Pack and co-workers, but the energy grid is less fine and the CRP does not display narrow resonance features until after the first two steplike increases in the CRP, from 0 to 1 and from 1 to 2, each of which is quite clean.

C. Li + HF: Theory

Another system where accurate microcanonical rate constants have been calculated is Li + HF $\rightarrow$ LiF + H with $J = 0$ (172). This reaction has variational transition states in the exit valley. Variational transition state theory agrees very well with accurate quantum dynamical calculations up to about 0.15 eV above threshold. After that, deviations are observed, increasing to about a factor of 2 about 0.3 eV above threshold. These deviations were attributed to effective barriers in the entrance valley; these are supernumerary transition states. After Gaussian convolution of the accurate results, only a hint of step structure due to the variational transition states remains. Densities of reactive states, which would make the transition state spectrum more visible, were not published (172).

D. Cl + H_2: Theory

We have also carried out accurate quantum scattering calculations for the reaction Cl + $H_2 \rightarrow$ HCl + H, which is about 0.13 eV endothermic in a Born-Oppenheimer sense and about 0.05 eV endothermic when zero-point energy is included. We used the G3 potential

energy surface (173) on which the Born-Oppenheimer barrier height is about 0.34 eV. Thus this is another nearly thermoneutral system of the $A + H_2$ type, with, however, a barrier height somewhat smaller than that for $D + H_2$ and $O + H_2$. For $JPS = 0++$, the CRP rises monotonically and the density of reactive states shows several clearly resolved quantized transition states. The lowest state, $[00^0]$, leads to a well-resolved plateau in the CRP at ~1.0, which is similar to the behavior seen above for $H + H_2$, $D + H_2$, and $O + H_2$. The next two peaks may be assigned to $[02^0]$ and a supernumerary transition state of the first kind with quantum numbers $[10^0]$. The value of the CRP at the local minimum following the third peak in the density is only about 1.8, though. The mere fact that the $[10^0]$ supernumerary transition state is one of the first kind indicates that the fundamental no-recrossing assumption of transition state theory is less valid for this system than for the other $A + H_2$ systems, and a value of only 1.8 for the CRP at the local minimum preceding the third variational transition state further illustrates the nonideal nature of the dynamics in this system, which will provide an interesting case for further analysis.

E. Experiment

Experimental detection of quantized transition states has been impeded by the difficulty of carrying out experiments in which only one or a few values of the total angular momentum J contribute to the signal. Otherwise the smearing effect of many values of J will tend to hide structure due to quantized transition states. Nevertheless, in the past five years, sophisticated measurements have supplied evidence for the influence of quantized transition states on a number of reactions.

We have already mentioned the interpretation of photodetachment spectra of FH_2^- and XHX^- (X = Cl, Br, I), in terms of quantized transition state resonances. Similar experiments have been carried out for IDI^-, OHF^-, $OHCl^-$, $OHOH^-$, and $HOHOH^-$ (174–177), and these experiments have been interpreted in terms of resonances and other types of vibration-rotation energy level structure associated with the transition state species of the neutral product (10,11,17–19,162,163,174–178). The FH_2^- and FD_2^- photodetachment experiments provide a particularly striking example of the observation of quantized transition states in experimental spectra (133–135). In theoretical work carried out to analyze recent experimental work on photodetachment, in particular for $OHCl^-$ (176), the calculated cumulative reaction probability for the $O + HCl$ reaction showed steps at quantized hindered rotor energies (as well as sharper resonances due to trapped states), but the steps had transmission coefficients considerably smaller than unity.

Photodissociation experiments provide one route to observing the dynamics associated with a single value of J, and as such would be expected (179) to be a good place to look for quantized transition state structure. For the photodissociation of triplet ketene, Lovejoy et al. (180) reported direct observation of a step in the microcanonical rate constant associated with a vibrationally excited transition state, and they interpreted their results using a theoretical framework similar to that used in Sec. IV. Further analysis was provided in later papers (181–183), including a discussion of subthreshold transmission resonances such as have also been predicted theoretically (184,185). The most recent paper from the Moore group (183) exhibits approximately three distinct steps each for photodissociation of CH_2CO and CD_2CO with further structure presumably corresponding to unresolved steps at higher energies. For CH_2CO the first peak was assigned to a

C—C—O bend, and another peak was assigned as a combination of the C—C—O bend with one quantum of hindered rotation.

Another experimental system where steplike structure possibly related to quantized transition states was observed is the work of Wittig and co-workers (186–188) on NO_2 dissociation; these experiments have been further analyzed by Klippenstein and Radivoyevitch (189) and Katagiri and Kato (190), both of whose studies indicate that the interpretation may be more complicated. Wittig and co-workers concluded (187) that the steps observed in the experimental microcanonical rate constants may correspond to overlapping of vibrationally adiabatic thresholds.

Choi et al. measured the *cis-trans* isomerization rate of *trans,trans*-1,3,5,7-octatetraene by exciting its vibronic bands in a supersonic jet and observing fluorescence decay (191). Choi et al. noticed a stepwise increase in the isomerization rate with energy, which they attributed to quantization of the vibrational levels of the transition state for *cis-trans* isomerization of a double bond. This study is especially noteworthy because quantization is observed in a molecule with 48 degrees of freedom. The energy spacing of 80 ± 10 cm^{-1} between the first two steps was tentatively assigned to an in-plane bending vibration of the transition state.

X. CONCLUDING REMARKS

In transition state theory it is assumed that a dynamical bottleneck in the interaction region controls chemical reactivity. Transition state theory relates the rate of a chemical reaction in a microcanonical ensemble to the number of energetically accessible vibrational-rotational levels of the interacting particles at the dynamical bottleneck. In spite of the success of transition state theory, direct evidence for a quantized spectrum of the transition state has been found only recently, and this evidence was found first in accurate quantum mechanical reactive scattering calculations. Quantized transition states have now been identified in accurate three-dimensional quantal calculations for 12 reactive atomdiatom systems. The systems are H + H_2, D + H_2, O + H_2, Cl + H_2, H + O_2, F + H_2, Cl + HCl, I + HI, I + DI, He + H_2^+, Ne + H_2^+, and O + HCl.

In this chapter we reviewed the evidence for the quantized nature of the spectrum of the transition state based on exact quantum mechanical reactive scattering calculations. We discussed fitting the accurate computational results by a model with level-dependent transmission probabilities that include recrossing effects and that account for tunneling and nonclassical reflection based on parabolic effective barriers. We discussed global control of reactivity for both zero and nonzero total angular momentum, and we also discussed the degree of ideality of the individual dynamical bottlenecks. We assigned quantum numbers to individual transition state levels by comparison of the results with maxima in vibrationally adiabatic potential curves. We discussed the relevance of the concept of vibrational adiabaticity for the accurate dynamics. We obtained spectroscopic constants for the quantized transition state by fitting to a truncated Taylor series in the vibrational quantum numbers. We also drew an explicit connection between quantized transition states and quantum mechanical quasibound states, both of which are related to poles of the scattering matrix. In this connection we discussed the relationship of thresholds and resonances. We derived transition state lifetimes for the H + H_2 transition states by identifying the lifetimes with the imaginary parts of the resonance energies and relating those imaginary energies to the effective parabolic potentials implied by the fit.

We also noted the reformulation of variational transition state theory in terms of quantum mechanical resonance theory.

We discussed the implications of the $O + H_2$ reaction's multiple bottleneck regions in terms of variational and supernumerary transition states. We related the observed features to the scattering results for asymmetrical Eckart potentials. We emphasized that global control is maintained to very high energy (1.9 eV) and very high levels of ν_2. We demonstrated the influence of quantized transition states at the level of state-selected reaction probability for this reaction.

Next, using $D + H_2$ as an example, we showed that quantized transition state spectra can be observed and analyzed even for very high total angular momenta, up to 15.

Using $F + H_2$ as an example, we discussed the correspondence of peaks in the photoelectron spectrum of the negative ion of the transition state with individual quantized transition states for $J = 0-2$. This system is very interesting in that the quantized energy levels show an internal rotation progression, and the average transmission coefficient is 0.95, with all transmission coefficients in the range 0.83–0.98. The ability to assign transmission coefficients to individual levels of the quantized transition state is one of the most remarkable developments of the theoretical analysis of accurate quantal reaction probabilities to date.

We also presented an analysis of halogen-hydrogen halide calculations. We discussed a formalism for probing the reaction at a finite time resolution by convoluting the exact results with a Gaussian function. We demonstrated that quantized transition states dominate the short time dynamics.

Accurate quantal dynamics calculations play important roles in predicting experimentally observable rates, cross sections, and transition probabilities, in elucidating and uncovering quantal phenomena, and in testing approximate dynamics calculations and models. The implementation of quantum mechanical scattering theory for quantal dynamics calculations on bimolecular collisions has become increasingly practical in recent years, especially for reactive collisions (8,12,77,96,101,102,164,166,167,192–220). The use of accurate quantum calculations for transition state spectroscopy, as reviewed in this chapter, provides an especially clear-cut example of where the calculations help us uncover fundamental quantum structures in nature that have a very significant impact even on highly averaged rate phenomena.

ACKNOWLEDGMENTS

REFERENCES

1. M. M. Kreevoy and D. G. Truhlar, Transition state theory, *Investigation of Rates and Mechanisms of Reactions* (C. F. Bernasconi, ed.) [*Techniques of Chemistry*, 4th ed., A. Weissberger (ed.)], John Wiley & Sons, New York, 1986, Part I, pp. 13–95.

2. G. Herzberg, *Electronic Spectra and Electronic Structure of Polyatomic Molecules* [*Molecular Spectra and Molecular Structure*, Vol. III], Van Nostrand Reinhold, New York, 1966, pp.. 458ff.

3. A. Bohm, *Quantum Mechanics*, 3rd ed., Springer-Verlag, New York, 1993, pp. 452–569.

4. J. Simons, Roles played by metastable states in chemisry, *ACS Symp. Ser. 263*: 3 (1984).

5. *Resonances*, E. Brändas and N. Elander (eds.) [*Lecture Notes in Physics*, Vol. 325], Springer-Verlag, Berlin, 1989.

6. P. D. Kleiber, A. M. Lyyra, K. M. Sando, V. Zafiropulos, and W. C. Stwalley, Reactive collision dynamics by far wing laser scattering: Mg + H_2, *J. Chem. Phys. 85*: 5493 (1986).

7. J. C. Polanyi, M. G. Prisant, and J. S. Wright, Spectroscopy of the transition state (theory). 4. Absorption by $HFH^{\ddagger}$ in H + FH' → $HFH^{\ddagger}$ → HF + H', *J. Phys. Chem. 91*: 4727 (1987).

8. D. C. Chatfield, R. S. Friedman, D. G. Truhlar, B. C. Garrett, and D. W. Schwenke, Global control of suprathreshold reactivity by quantized transition states, *J. Am. Chem. Soc. 113*: 486 (1991).

9. D. C. Chatfield, R. S. Friedman, D. G. Truhlar, and D. W. Schwenke, Quantum-dynamical characterization of reactive transition states, *Faraday Discuss. Chem. Soc. 91*: 289 (1991).

10. D. C. Chatfield, R. S. Friedman, G. C. Lynch, and D. G. Truhlar, Discussion remarks, *Faraday Discuss. Chem. Soc. 91*: 398 (1991).

11. D. C. Chatfield, R. S. Friedman, G. C. Lynch, and D. G. Truhlar, Quantized transition-state structure in the cumulative reaction probabilities for the Cl + HCl, I + HI and I + DI reactions, *J. Phys. Chem. 96*: 57 (1992).

12. K. Haug, D. W. Schwenke, D. G. Truhlar, Y. Zhang, J. Z. H. Zhang, and D. J. Kouri, Accurate quantum mechanical reaction probabilities for the reaction O + H_2 → OH + H, *J. Chem. Phys. 87*: 1892 (1987).

13. J. M. Bowman, Comparison of reduced dimensionality and accurate cumulative reaction probabilities for $O(^3P)$ + H_2 (v = 0, 1), *Chem. Phys. Lett. 141*: 545 (1987).

14. D. C. Chatfield, R. S. Friedman, G. C. Lynch, D. G. Truhlar, and D. W. Schwenke, The nature and role of quantized transition states in the accurate quantum dynamics of the reaction O + H_2 → OH + H, *J. Chem. Phys. 98*: 342 (1993).

15. G. C. Lynch, P. Halvick, M. Zhao, D. G. Truhlar, C.-H. Yu, D. J. Kouri, and D. W. Schwenke, Converged three-dimensional quantum mechanical reaction probabilities for the F + H_2 reaction on a potential energy surface with realistic entrance and exit channels and comparisons to results for three other surfaces, *J. Chem. Phys. 94*: 7150 (1991).

16. D. C. Chatfield, R. S. Friedman, D. W. Schwenke, and D. G. Truhlar, Control of chemical reactivity of quantized transition states, *J. Phys. Chem. 96*: 2414 (1992).

17. G. C. Schatz, A three dimensional reactive scattering study of the photodetachment spectrum of $ClHCl^-$, *J. Chem. Phys. 90*: 3582 (1989).

18. G. C. Schatz, A three-dimensional quantum reactive scattering study of the I + HI reaction and of the IHI^- photodetachment spectrum, *J. Chem. Phys. 90*: 4847 (1989).

19. G. C. Schatz, A three-dimensional quantum reactive scattering study of the I + DI reaction and of the IDI^- photodetachment spectrum, *J. Chem. Soc. Faraday Trans. 86*: 1729 (1990).

20. B. C. Garrett and D. G. Truhlar, Generalized transition state theory. Classical mechanical theory and applications to collinear reactions of hydrogen molecules, *J. Phys. Chem. 83*: 1052 (1979). Errata: *83*: 3058 (1979): *87*: 4553 (1983).

21. R. A. Marcus, Chemical-reaction cross sections, quasiequilibrium, and generalized activated complexes, *J. Chem. Phys. 45*: 2138 (1966).

22. F. T. Smith, Scattering matrix and chemical reaction rates, *J. Chem. Phys. 36*: 248 (1962).

23. W. H. Miller, Semiclassical limit of quantum mechanical transition state theory for nonseparable systems, *J. Chem. Phys. 62*: 1899 (1975).

24. E. Wigner, Calculation of the rate of elementary association reactions, *J. Chem. Phys. 5*: 720 (1937).

25. J. Horiuti, On the statistical mechanical treatment of the absolute rate of chemical reaction, *Bull. Chem. Soc. Japan 13*: 210 (1938).
26. J. C. Keck, Variational theory of reaction rates, *Adv. Chem. Phys. 13*: 85 (1967).
27. D. G. Truhlar and B. C. Garrett, Variational transition state theory, *Annu. Rev. Phys. Chem. 35*: 159 (1984).
28. S. C. Tucker and D. G. Truhlar, Dynamical formulation of transition state theory: Variational transition states and semiclassical tunneling, *New Theoretical Concepts for Understanding Organic Reactions* (J. Bertrán and I. G. Csizmadia, Eds.), Kluwer, Dordrecht, 1989, p. 291.
29. H. Eyring, The activated complex in chemical reactions, *J. Chem. Phys. 3*: 107 (1935).
30. R. A. Marcus and O. K. Rice, The kinetics of the recombination of methyl radicals and iodine atoms, *J. Phys. Colloid Chem. 55*: 894 (1951).
31. R. A. Marcus, Unimolecular dissociations and free radical recombination reactions, *J. Chem. Phys. 20*: 359 (1952).
32. H. M. Rosenstock, M. B. Wallenstein, A. L. Wahrhaftig, and H. Eyring, Absolute rate theory for isolated systems and the mass spectra of polyatomic molecules, *Proc. Natl. Acad. Sci. USA 38*: 667 (1952).
33. J. L. Magee, Theory of the chemical reaction rate constant, *Proc. Natl. Acad. Sci. U.S.A. 38*: 764 (1952).
34. B. C. Garrett and D. G. Truhlar, Generalized transition state theory. Quantum effects for collinear reactions of hydrogen molecules and isotopically substituted hydrogen molecules, *J. Phys. Chem. 83*: 1079 (1979); Errata: *84*: 682 (1980); *87*: 4553 (1983).
35. D. G. Truhlar, A. D. Isaacson, and B. C. Garrett, Generalized transition state theory, *Theory of Chemical Reaction Dynamics* (M. Baer, ed.), CRC Press, Boca Raton, FL, 1985, Vol. 4, p. 65.
36. E. C. Kemble, *The Fundamental Principles of Quantum Mechanics with Elementary Applications*, Dover, New York, 1958, p. 109.
37. J. J. Sakurai, *Modern Quantum Mechanics*, Addison-Wesley, Redwood City, CA, 1985, pp. 78–80.
38. W. H. Miller, Quantum mechanical transition state theory and a new semiclassical model for reaction rate constants, *J. Chem. Phys. 61*: 1823 (1974).
39. J. W. Tromp and W. H. Miller, New approach to quantum mechanical transition-state theory, *J. Phys. Chem. 90*: 3482 (1986).
40. J. W. Tromp and W. H. Miller, The reactive flux correlation function for collision reactions H + H$_2$, Cl + HCl, and F + H$_2$, *Faraday Discuss. Chem. Soc. 84*: 441 (1987).
41. P. N. Day and D. G. Truhlar, Benchmark calculation of thermal reaction rates. II. Direct calculation of the flux autocorrelation function for a canonical ensemble, *J. Chem. Phys. 94*: 2045 (1991).
42. P. N. Day and D. G. Truhlar, Calculation of thermal rate coefficients from the quantum flux autocorrelation function: Converged results and variational quantum transition state theory for O + HD → OD + H and O + HD → OH + D, *J. Chem. Phys. 95*: 5097 (1991).
43. E. J. Heller, Potential surfaces properties and dynamics from molecular spectra: A time-dependent picture, *Potential Energy Surfaces and Dynamics Calculations* (D. G. Truhlar, ed.), Plenum Press, New York, 1981, p. 103.
44. M. J. Seaton, The Hartree-Fock equations for continuous states with applications to electron excitation of the ground configuration terms of O$_1$, *Philos, Trans. Roy. Soc. London A 245*: 469 (1953).
45. H. S. W. Massey, Theory of the scattering of slow electrons, *Rev. Mod. Phys. 28*: 199 (1956).
46. D. A. Micha, A quantum mechanical model for simple molecular reactions, *Arkiv. Fys. 30*: 411 (1965).
47. W. H. Miller, Coupled equations and the minimum principle for collisions of an atom and a diatomic molecule, including rearrangements, *J. Chem. Phys. 50*: 407 (1969).

48. D. G. Truhlar, J. Abdallah, Jr., and R. L. Smith, Algebraic variational methods in scattering theory, *Adv. Chem. Phys. 25*: 211 (1974).

49. D. G. Truhlar and J. Abdallah, Jr., New methods for calculating scattering cross sections for rearrangement collisions, *Phys. Rev. A 9*: 297 (1974).

50. R. G. Newton, *Scattering Theory of Particles and Waves*, 2nd ed., Springer-Verlag, New York, 1982 (Section 11.3, variational principles; Section 11.2, resonances as poles of the S matrix).

51. G. Staszewska and D. G. Truhlar, Convergence of $\mathscr{L}^2$ methods for scattering problems, *J. Chem. Phys. 86*: 2793 (1987).

52. D. W. Schwenke, K. Haug, D. G. Truhlar, Y. Sun, J. Z. H. Zhang, and D. J. Kouri, Variational basis-set calculations of accurate quantum mechanical reaction probabilities, *J. Phys. Chem. 91*: 6080 (1987).

53. D. W. Schwenke, K. Haug, M. Zhao, D. G. Truhlar, Y. Sun, J. Z. H. Zhang, and D. J. Kouri, Quantum mechanical algebraic variational methods for inelastic and reactive molecular collisions, *J. Phys. Chem. 92*: 3202 (1988).

54. D. W. Schwenke, M. Mladenovic, M. Zhao, D. G. Truhlar, Y. Sun, and D. J. Kouri, Computational strategies and improvements in the linear algebraic variational approach to rearrangement scattering, *Supercomputer Algorithms for Reactivity Dynamics and Kinetics of Small Molecules* (A. Laganà, ed.), Kluwer, Dordrecht, 1989, p. 131.

55. L. Schlessinger, Use of analyticity in the calculation of nonrelativistic scattering amplitudes, *Phys. Rev. 167*: 1411 (1968).

56. Y. Sun, D. J. Kouri, D. G. Truhlar, and D. W. Schwenke, Dynamical basis sets for algebraic variational calculations in quantum-mechanical scattering theory, *Phys. Rev. A 41*: 4857 (1990).

57. Y. Sun, D. J. Kouri, and D. G. Truhlar, A comparative analysis of variational methods for inelastic and reactive scattering, *Nucl. Phys. A508*: 41c (1990).

58. D. W. Schwenke, S. L. Mielke, and D. G. Truhlar, Variational reactive scattering calculations: computational optimization strategies, *Theor. Chim. Acta 79*: 241 (1991).

59. J. Z. H. Zhang, D. J. Kouri, K. Haug, D. W. Schwenke, Y. Shima, and D. G. Truhlar, $\mathscr{L}^2$ amplitude density method for multichannel inelastic and rearrangement collisions, *J. Chem. Phys. 88*: 2492 (1988).

60. D. W. Schwenke and D. G. Truhlar, Localized basis functions and other computational improvements in variational nonorthogonal basis function methods for quantum mechanical scattering problems involving chemical reactions, *Computing Methods in Applied Sciences and Engineering* (R. Glowinski and A. Lichnewsky, Eds.), SIAM, Philadelphia, 1990, p. 291.

61. S. L. Mielke, D. G. Truhlar, and D. W. Schwenke, Improved techniques for outgoing wave variational principle calculations of converged state-to-state transition probabilities for chemical reactions, *J. Chem. Phys. 95*: 5930 (1991).

62. G. J. Tawa, S. L. Mielke, D. G. Truhlar, and D. W. Schwenke, Algebraic variational and propagation formalisms for quantal dynamics calculations of electronic-to-vibrational, rotational energy transfer and application to the quenching of the 3p state of sodium by hydrogen molecules, *J. Chem. Phys. 100*: 5751 (1994).

63. G. J. Tawa, S. L. Mielke, D. G. Truhlar, and D. W. Schwenke, Linear algebraic formulation of reactive scattering with general basis functions, *Advances in Molecular Vibrations and Collision Dynamics*, Vol. 2B (J. M. Bowman, ed.), JAI, Greenwich, CT, 1994, p. 45.

64. S. L. Mielke, G. C. Lynch, D. G. Truhlar, and D. W. Schwenke, Ab initio chemical kinetics: Converged quantal rate constants for the D + H_2 systems, *J. Phys. Chem. 98*: 8000 (1994).

65. A. J. C. Varandas, F. B. Brown, C. A. Mead, D. G. Truhlar, and N. C. Blais, A double many-body expansion of the two lowest-energy potential surfaces and nonadiabatic coupling for H_3, *J. Chem. Phys. 86*: 6258 (1987).

66. G. Herzberg, *Infrared and Raman Spectra of Polyatomic Molecules* [*Molecular Spectra and Molecular Structure*, Vol. II], Van Nostrand Reinhold, New York, 1945, pp. 15, 75, 205.

67. M. A. Eliason and J. O. Hirschfelder, General collision theory treatment for the rate of gas phase reactions, *J. Chem. Phys. 30*: 1426 (1959).

68. L. Hofacker, Quantentheorie chemischer Reaktionen, *Z. Naturforsch. 18a*: 607 (1963).

69. D. G. Truhlar, The adiabatic theory of chemical reactions, *J. Chem. Phys. 53*: 2041 (1970).

70. D. G. Truhlar and A. Kuppermann, Exact tunneling calculations, *J. Amer. Chem. Soc. 93*: 1840 (1971).

71. B. C. Garrett, D. G. Truhlar, R. S. Grev, and A. W. Magnuson, Improved treatment of threshold contributions in variational transition-state theory, *J. Phys. Chem. 84*: 1730 (1980). Erratum: *87*: 4554 (1983).

72. R. A. Marcus, On the analytical mechanics of chemical reactions. Quantum mechanics of linear collisions, *J. Chem. Phys. 45*: 4493 (1965).

73. R. A. Marcus, Analytical mechanics and almost vibrationally-adiabatic chemical reactions, *Discussions Faraday Soc. 44*: 7 (1967).

74. B. C. Garrett and D. G. Truhlar, WKB approximation for the reaction-path Hamiltonian: Application to variational transition state theory, vibrationally adiabatic excited-state barrier heights, and resonance calculations, *J. Chem. Phys. 81*: 309 (1984).

75. D. G. Truhlar, Oscillators with quartic anharmonicity: Approximate energy levels, *J. Molec. Spec. 38*: 4151 (1971).

76. B. C. Garrett and D. G. Truhlar, Generalized transition state theory calculations for the reactions $D + H_2$ and $H + D_2$ using an accurate potential energy surface: Explanation of the kinetic isotope effect, *J. Chem. Phys. 72*: 3460 (1980).

77. G. C. Lynch, P. Halvick, D. G. Truhlar, B. C. Garrett, D. W. Schwenke, and D. J. Kouri, Semiclassical and quantum mechanical calculations of isotopic kinetic branching ratios for the reaction of $O(^3P)$ with HD, *Zeitschrift für Naturforschung 44a*: 427 (1989).

78. B. C. Garrett, D. G. Truhlar, A. J. C. Varandas, and N. C. Blais, Semiclassical variational transition state calculations for the reactions of H and D with thermal and vibrationally excited H_2, *Int. J. Chem. Kin. 18*: 1065 (1986).

79. R. D. Levine and S.-F. Wu, Resonances in reactive collisions: Computational study of the $H + H_2$ collision, *Chem. Phys. Lett. 11*: 557 (1971).

80. N. Abu-Salbi, D. J. Kouri, M. Baer, and E. Pollak, A study of the quantal time delay matrix in collinear reactive scattering, *J. Chem. Phys. 82*: 4500 (1985).

81. E. Pollak, Periodic orbit analysis of bend level structure of resonances in 3D $H + H_2$ reactive scattering, *Chem. Phys. Lett. 137*: 171 (1987).

82. O. Atabek, R. Lefebvre, M. Garcia Sucre, J. Gomez-Llorente, and H. Taylor, Quantum localizations over a potential barrier, *Int. J. Quant. Chem. 40*: 211 (1991).

83. R. S. Friedman and D. G. Truhlar, Chemical reaction thresholds are resonances, *Chem. Phys. Lett. 183*: 539 (1991).

84. R. S. Friedman, V. D. Hullinger, and D. G. Truhlar, Quantum mechanical threshold resonances for unsymmetric potential energy barriers, *J. Phys. Chem. 99*: 3184 (1995).

85. A. J. F. Siegert, On the derivation of the dispersion formula for nuclear reactions, *Phys. Rev. 56*: 750 (1939).

86. J. R. Taylor, *Scattering Theory: The Quantum Theory of Nonrelativistic Collisions*, Krieger, Malabar, Florida, 1983, p. 407.

87. M. Zhao and S. A. Rice, Resonance state approach to quantum transition state theory, *J. Phys. Chem. 98*: 3444 (1994).

88. D. G. Truhlar and B. C. Garrett, Resonance state approach to quantum mechanical variational transition state theory, *J. Phys. Chem. 96*: 6515 (1992).

89. W. H. Miller, R. Hernandez, N. C. Handy, D. Jayatilaka, and A. Willetts, *Ab initio* calculation of anharmonic constants for a transition state, with application to semiclassical transition state tunneling probabilities, *Chem. Phys. Lett. 172*: 62 (1990).

90. M. J. Cohen, N. C. Handy, R. Hernandez, and W. H. Miller, Cumulative reaction probabilities for H + H_2 → H_2 + H from a knowledge of the anharmonic force field, *Chem. Phys. Lett.* **192**: 407 (1992).

91. H. Feshbach, The unified theory of nuclear reactions. III. Overlapping resonances, *Ann. Phys. (N.Y.)* **43**: 410 (1967).

92. H. Feshbach, *Theoretical Nuclear Physics: Nuclear Reactions*, John Wiley & Sons, New York, 1992, pp. 164–169, 211–213, 248–249.

93. T. Siedeman and W. H. Miller, Transition state theory, Siegert eigenstates, and quantum mechanical rates, *J. Chem. Phys.* **95**: 1768 (1991).

94. V. Ryaboy and N. Moiseyev, Cumulative reaction probability from Siegert eigenvalues: Model Studies, *J. Chem. Phys.* **98**: 9618 (1993).

95. A. Kuppermann, Reactive scattering resonances and their physical interpretation: The vibrational structure of the transition state, *Potential Energy Surfaces and Dynamics Calculations* (D. G. Truhlar, ed.), Plenum, New York, 1981, p. 375.

96. S. A. Cuccaro, P. G. Hipes, and A. Kuppermann, Symmetry analysis of accurate H + H_2 resonances for low partial waves, *Chem. Phys. Lett.* **157**: 440 (1989).

97. F. T. Smith, Lifetime matrix in collision theory, *Phys. Rev.* **118**: 349 (1960).

98. T. Seideman and W. H. Miller, Quantum mechanical reaction probabilities via a discrete variable representation-absorbing boundary condition Green's function, *J. Chem. Phys.* **97**: 2499 (1992).

99. W. H. Miller, Beyond transition-state theory: A rigorous quantum theory of chemical reaction rates, *Acc. Chem. Res.* **26**: 174 (1993).

100. U. Manthe and W. H. Miller, The cumulative reaction probability as eigenvalue problem, *J. Chem. Phys.* **99**: 3411 (1993).

101. D. C. Chatfield, D. G. Truhlar, and D. W. Schwenke, Benchmark calculations of thermal reaction rates. I. Quantal scattering theory, *J. Chem. Phys.* **94**: 2040 (1991).

102. J. Z. H. Zhang, Y. Zhang, D. J. Kouri, B. C. Garrett, K. Haug, D. W. Schwenke, and D. G. Truhlar, $\mathscr{L}^2$ Calculations of accurate quantal-dynamical reactive scattering transition probabilities and their use to test semiclassical applications, *Faraday Discuss. Chem. Soc.* **84**: 3711 (1987).

103. Y. Sun, C. h. Yu, D. J. Kouri, D. W. Schwenke, P. Halvick, M. Mladenovic, and D. G. Truhlar, Direct calculation of the reactive transition matrix by $\mathscr{L}^2$ quantum mechanical variational methods with complex boundary conditions, *J. Chem. Phys.* **91**: 1643 (1989).

104. B. R. Johnson and N. W. Winter, Classical trajectory study of the effect of vibrational energy on the reaction of molecular hydrogen with atomic oxygen, *J. Chem. Phys.* **66**: 4116 (1977).

105. G. C. Schatz, A coupled states distorted wave study of the $O(^3P)$ + $H_2(D_2, HD, DH)$ reaction, *J. Chem. Phys.* **83**: 5677 (1985).

106. D. G. Truhlar, K. Runge, and B. C. Garrett, Variational transition state theory and tunneling calculations of potential energy surface effects on the reaction of $O(^3P)$ with H_2, *Twentieth Symposium (International) on Combustion*, Combustion Institute, Pittsburgh, 1984, p. 585.

107. B. C. Garrett and D. G. Truhlar, Thermal and state-selected rate constant calculations for $O(^3P)$ + H_2 → OH + H and isotopic analogs, *Int. J. Quantum Chem.* **29**: 1463 (1986).

108. T. Joseph, D. G. Truhlar, and B. C. Garrett, Improved potential energy surfaces for the reaction $O(^3P)$ + H_2 → OH + H, *J. Chem. Phys.* **88**: 6982 (1988).

109. J. M. Bowman and A. F. Wagner, Reduced dimensionality theories of Quantum reactive scattering: Applications to Mu + H_2, H + H_2, $O(^3P)$ + H_2, D_2, and HD, *The Theory of Chemical Reaction Dynamics* (D. C. Clary, ed.), Reidel, Dordrecht, 1986, p. 47.

110. B. C. Garrett, D. G. Truhlar, J. M. Bowman, and A. F. Wagner, Evaluation of dynamical approximations for calculating the effect of vibrational excitation on reaction rates. O + H_2 ($n = 0, 1$) ↔ OH + H, *J. Phys. Chem.* **90**: 4305 (1986).

111. R. D. Levine, Radiationless transitions and population inversions: Two examples of internal conversions, *Chem. Phys. Lett.* **10**: 510 (1971).

112. J. W. Duff and D. G. Truhlar, Effect of curvature of the reaction path on dynamic effects in endothermic reactions and product energies in exothermic reactions, *J. Chem. Phys. 62*: 2477 (1975).

113. D. G. Truhlar and D. A. Dixon, Direct-mode chemical reactions: Classical theories, *Atom-Molecule Collision Theory* (R. B. Bernstein, ed.), Plenum, New York, 1979, p. 595.

114. B. Liu, *Ab initio* potential energy surface for linear H_3, *J. Chem. Phys. 58*: 1925 (1973).

115. P. Siegbahn and B. Liu, An accurate three-dimensional potential energy surface for H_3, *J. Chem. Phys. 68*: 2457 (1978).

116. D. G. Truhlar and C. J. Horowitz, Functional representation of Liu and Siegbahn's *ab initio* potential energy calculations for $H + H_2$, *J. Chem. Phys. 68*: 2466 (1978). Erratum: *71*: 1514 (1979).

117. J. V. Michael and J. R. Fisher, Rate constants for the reaction $D + H_2 \rightarrow HD + H$ over the temperature range 655–1979 K, by the flash photolysis-shock tube technique, *J. Phys. Chem. 94*: 3318 (1990) and references therein.

118. D. G. Truhlar and R. E. Wyatt, History of H_3 kinetics, *Annu. Rev. Phys. Chem. 27*: 1 (1976).

119. S.-F. Wu, B. R. Johnson, and R. D. Levine, Quantum mechanical computational studies of chemical reactions: III. Collinear $A + BC$ reaction with some model potential energy surfaces, *Mol. Phys. 25*: 839 (1973).

120. T. C. Thompson and D. G. Truhlar, Stabilization calculations and probability densities for the well-studied collisional resonances in collinear $F + H_2$, $F + HD$, and $F + D_2$, *J. Phys. Chem. 88*: 210 (1984).

121. C. C. Marston and R. E. Wyatt, Resonant quasi-periodic and periodic orbits for the three-dimensional reaction of fluorine atoms with hydrogen molecules, *ACS Symp. Ser. 263*: 441 (1984).

122. Z. H. Zhang, N. Abusalbi, M. Baer, D. J. Kouri, and J. Jellinek, Resonance phenomena in quantal reactive infinite-order sudden calculations, *ACS Symp. Ser. 263*: 457 (1984).

123. D. M. Neumark, A. M. Wodtke, G. N. Robinson, C. C. Hayden, and Y. T. Lee, Dynamic resonances in the reaction of fluorine atoms with hydrogen molecules, *ACS Symp. Ser. 263*: 479 (1984).

124. E. F. Hayes and R. B. Walker, Reactive resonances and angular distributions in the rotating linear model, *ACS Symp. Ser. 263*: 493 (1984).

125. D. M. Neumark, A. M. Wodtke, G. N. Robinson, C. C. Hayden, and Y. T. Lee, Molecular beam studies of the $F + H_2$ reaction, *J. Chem. Phys. 82*, 3045 (1985).

126. S. L. Mielke, G. C. Lynch, D. G. Truhlar, and D. W. Schwenke, A more accurate potential energy surface and quantum mechanical cross section calculations for the $F + H_2$ reaction, *Chem. Phys. Lett. 213*: 10 (1993). Erratum: *217*: 173 (1994).

127. R. Steckler, D. W. Schwenke, F. B. Brown, and D. G. Truhlar, An improved calculation of the transition state for the $F + H_2$ reaction, *Chem. Phys. Lett. 121*: 475 (1985).

128. D. W. Schwenke, R. Steckler, F. B. Brown, and D. G. Truhlar, The potential energy surface for the $F + H_2$ reaction as a function of bond angle in the saddle point vicinity, *J. Chem. Phys. 84*: 5706 (1986).

129. G. C. Lynch, R. Steckler, D. W. Schwenke, A. J. C. Varandas, D. G. Truhlar, and B. C. Garrett, Use of scaled external correlation, a double many-body expansion, and variational transition state theory to calibrate a potential energy surface for FH_2, *J. Chem. Phys. 94*: 7136 (1991).

130. C. W. Bauschlicher, S. P. Walch, S. R. Langhoff, P. R. Taylor, and R. L. Jaffe, Theoretical studies of the potential surface for the $F + H_2 \rightarrow HF + H$ reaction, *J. Chem. Phys. 88*: 1743 (1988).

131. P. J. Knowles, K. Stark, and H. J. Werner, A full-CI study of the energetics of the reaction $F + H_2 \rightarrow HF + H$, *Chem. Phys. Lett. 185*: 555 (1991).

132. C. h. Yu, Y. Sun, D. J. Kouri, P. Halvick, D. G. Truhlar, and D. W. Schwenke, Converged quantum dynamics calculations for the $F + H_2$ reaction on the well-studied M5 potential-energy surface, *J. Chem. Phys. 90*: 7608 (1989).

133. A. Weaver and D. M. Neumark, Negative-ion photodetachment as a probe of bimolecular transition states: The F + H_2 reaction, *Faraday Discuss. Chem. Soc. 91*: 5 (1991).

134. S. E. Bradforth, D. W. Arnold, D. M. Neumark, and D. E. Manolopoulos, Experimental and theoretical studies of the F + H_2 transition state region via photoelectron spectroscopy of FH_2^-, *J. Chem. Phys. 99*: 6345 (1993).

135. D. E. Manolopoulos, K. Stark, H. J. Werner, D. W. Arnold, S. E. Bradforth, and D. M. Neumark, The transition state of the F + H_2 reaction, *Science 262*: 1852 (1993).

136. J. D. Kress and E. F. Hayes, Assignment of peaks in photodetachment spectra using predicted densities of reactive states: Applications to H_2F^- and D_2F^-, *J. Chem. Phys. 97*: 4881 (1992).

137. A. M. Arthurs and A. Dalgarno, The theory of scattering by a rigid rotator, *Proc. Roy. Soc. Lond. A156*: 540 (1960).

138. S. Bratož and M. L. Martin, Infrared spectra of highly compressed gas mixtures of the type HCl + X. A theoretical study, *J. Chem. Phys. 42*: 1051 (1965).

139. S. V. O'Neil, D. J. Nesbitt, P. Rosmus, H. J. Werner, and D. C. Clary, Weakly bound NeHF, *J. Chem. Phys. 91*: 711 (1989).

140. D. J. Nesbitt, C. M. Lovejoy, T. G. Lindeman, S. V. O'Neil, and D. C. Clary, Slit jet infrared spectroscopy of NeHF complexes: Internal rotor and *J*-dependent predissociation dynamics, *J. Chem. Phys. 91*: 722 (1989).

141. D. W. Schwenke, On the computational of ro-vibrational energy levels of triatomic molecules, *Comp. Phys. Commun. 70*: 1 (1992).

142. B. C. Garrett, D. G. Truhlar, R. S. Grev, A. W. Magnuson, and J. N. L. Connor, Variational transition state theory, vibrationally adiabatic transmission coefficients, and the unified statistical model tested against accurate quantal rate constants for collinear F + H_2, H + F_2, and isotopic analogs, *J. Chem. Phys. 73*: 1721 (1980).

143. D. G. Truhlar, W. L. Hase, and J. T. Hynes, Current status of transition-state theory, *J. Phys. Chem. 87*: 2664 (1983). Additions and corrections: *87*: 5523 (1983).

144. D. G. Truhlar and B. C. Garrett, Dynamical bottlenecks and semiclassical tunneling paths for chemical reactions, *J. Chim. Phys. 84*: 365 (1987).

145. G. C. Lynch, D. G. Truhlar, and B. C. Garrett, Test of the accuracy of small–curvature and minimum–energy reference paths for parameterizing the search for least–action tunneling paths: (H,D) + H'Br → (H,D)Br + H', *J. Chem. Phy. 90*: 3102 (1989). Erratum: *91*: 3280 (1989).

146. B. C. Garrett and D. G. Truhlar, Critical tests of variational transition state theory and semiclassical tunneling methods for hydrogen and deuterium atom transfer reactions and use of the semiclassical calculations to interpret the overbarrier and tunneling dynamics, *J. Phys. Chem. 95*: 10374 (1991).

147. D. G. Truhlar and B. C. Garrett, General discussion, *Faraday Discuss. Chem. Soc. 84*: 465 (1987).

148. J. A. Kaye and A. Kuppermann, Collinear quantum mechanical properties for the I + HI → IH + H reaction using hyperspherical coordinates, *Chem. Phys. Lett. 77*: 573 (1981).

149. V. K. Babamov and R. A. Marcus, Dynamics of hydrogen atom and proton transfer reaction. Symmetric case, *J. Chem. Phys. 74*: 1790 (1981).

150. J. Manz and J. Römelt, On the collinear I + HI and I + MuI reactions, *Chem. Phys. Lett. 81*: 179 (1981).

151. D. K. Bondi, J. N. L. Connor, B. C. Garrett, and D. G. Truhlar, Test of variational transition state theory with a large-curvature tunneling approximation against accurate quantal reaction probabilities and rate coefficients for three collinear reactions with large reaction–path curvature: Cl + HCl, Cl + DCl, and Cl + MuCl, *J. Chem. Phys. 78*: 5981 (1983).

152. D. K. Bondi, J. N. L. Connor, J. Manz, and J. Römelt, Exact quantum and vibrationally adiabatic quantum semiclassical and quasiclassical study of the collinear reactions Cl + MuCl, Cl + HCl, Cl + DCl, *Mol. Phys. 50*: 467 (1983).

153. D. G. Truhlar, B. C. Garrett, P. G. Hipes, and A. Kuppermann, Test of variational transition state theory against accurate quantal results for a reaction with very large reaction–path curvature and a low barrier, *J. Chem. Phys. 81*: 3542 (1984).

154. J. Manz, Molecular dynamics along hyperspherical coordinates, *Comm. At. Mol. Phys. 17*: 91 (1985).

155. J. Römelt, Calculations on collinear reactions using hyperspherical coordinates, *Theory of Chemical Reaction Dynamics* (D. C. Clary, ed.), Reidel, Dordrecht, 1986, p. 77.

156. J. M. Bowman and B. Gazdy, A reduced dimensionality $\mathscr{L}^2$ simulation of the photodetachment spectra of $ClHCl^-$ and IHI^-, *J. Phys. Chem. 93*: 5129 (1989).

157. G. C. Schatz, D. Sokolovski, and J. N. L. Connor, Influence of transition state resonances on integral cross sections and product rovibrational distributions for the $Cl + HCl \rightarrow ClH + Cl$ reaction, *J. Chem. Phys. 94*: 4311 (1991).

158. R. B. Metz and D. M. Neumark, Adiabatic three-dimensional simulations of the IHI^-, $BrHI^-$, and $BrHBr^-$ photoelectron spectra, *J. Chem. Phys. 97*: 962 (1992).

159. M. J. Cohen, A. Willetts, and N. C. Handy, Cumulative reaction probabilities for $OH + H_2 \rightarrow H_2O + H$ and $ClH + Cl \rightarrow Cl + HCl$ from a knowledge of the anharmonic force field, *J. Chem. Phys. 99*: 5885 (1993).

160. A. Weaver, R. B. Metz, S. E. Bradforth, and D. M. Neumark, Spectroscopy of the $I + HI$ transition-state region by photodetachment of IHI^-, *J. Phys. Chem. 92*: 5558 (1988).

161. R. B. Metz, T. Kitsopoulos, A. Weaver, and D. M. Neumark, Study of the transition state region in the $Cl + HCl$ reaction by photoelectron spectroscopy of $ClHCl^-$, *J. Chem. Phys. 88*: 1463 (1988).

162. R. B. Metz, A. Weaver, S. E. Bradforth, T. N. Kitsopoulos, and D. M. Neumark, Probing the transition state with negative ion photodetachment: The $Cl + HCl$ and $Br + HBr$ reactions, *J. Phys. Chem. 94*: 1377 (1990).

163. S. E. Bradforth, D. W. Arnold, R. B. Metz, A. Weaver, and D. M. Neumark, Spectroscopy of the transition state: Hydrogen abstraction reactions of fluorine, *J. Phys. Chem. 95*: 8066 (1991).

164. Z. Darakjian, E. F. Hayes, G. A. Parker, E. A. Butcher, and J. D. Kress, Direct calculation of collisional properties that require energy derivatives of the S matrix: Results for the reaction $He + H_2^+ \rightarrow HeH^+ + H$, *J. Chem. Phys. 95*: 2516 (1991). Erratum: *101*: 9203 (1994).

165. S. K. Klippenstein and J. D. Kress, Comparison of variational Rice-Ramsperger-Kassel-Marcus theory with quantum scattering theory for the $He + H_2^+ \rightarrow HeH^+ + H$ reaction, *J. Chem. Phys. 96*: 8164 (1992).

166. R. T Pack, E. A. Butcher, and G. A. Parker, Accurate quantum probabilities and threshold behavior of the $H + O_2$ combustion reaction, *J. Chem. Phys. 99*: 9310 (1993).

167. J. D. Kress, Accurate three-dimensional quantum cumulative reaction probabilities for $Ne + H_2^+ \rightarrow NeH^+ + H$, *J. Chem. Phys. 95*: 8673 (1991).

168. J. D. Kress and S. J. Klippenstein, Comparison of variational RRKM theory with quantum scattering theory for the $Ne + H_2^+ \rightarrow NeH^+ + H$ reaction, *Chem. Phys. Lett. 195*: 513 (1992).

169. J. D. Kress, R. B. Walker, E. F. Hayes, and P. Pendergast, Quantum scattering studies of long-lived resonances for the $Ne + H_2^+ \rightarrow NeH^+ + H$ reaction, *J. Chem. Phys. 100*: 2728 (1994).

170. R. T Pack, E. A. Butcher, and G. A. Parker, Accurate three-dimensional quantum properties and collision lifetimes of the $H + O_2$ combustion reaction, *J. Chem. Phys. 102*: 5998 (1995).

171. C. Leforestier and W. H. Miller, Quantum mechanical calculation of the rate constant for the reaction $H + O_2 \rightarrow OH + O$, *J. Chem. Phys. 100*: 733 (1994).

172. C. Y. Yang, S. J. Klippenstein, J. D. Kress, R. T Pack, G. A. Parker, and A. Laganà, Comparison of transition state theory with quantum scattering theory for the reaction $Li + HF \rightarrow LiF + H$, *J. Chem. Phys. 100*: 4917 (1994).

173. T. C. Allison, S. L. Mielke, G. C. Lynch, D. G. Truhlar, and M. S. Gordon, An improved potential energy surface for the H_2Cl system and its use for calculations of rate constants and kinetic isotope effects, manuscript in preparation.

174. R. B. Metz, S. E. Bradforth, and D. M. Neumark, Transition state spectroscopy of bimolecular reactions using negative ion photodetachment, *Adv. Chem. Phys. 81*: 1 (1992).

175. D. M. Neumark, Transition state spectroscopy of bimolecular chemical reactions, *Annu. Rev. Phys. Chem. 43*: 153 (1992).

176. M. J. Davis, H. Koizumi, G. C. Schatz, S. E. Bradforth, and D. M. Neumark, Experimental and theoretical study of the O + HCl transition state region by photodetachment of $OHCl^-$, *J. Chem. Phys. 101*: 4708 (1994).

177. D. W. Arnold, C. Xu, and D. M. Neumark, Spectroscopy of the transition state: Elementary reactions of the hydroxyl radical studied by photoelectron spectroscopy of $O^-(H_2O)$ and $H_3O_2^-$, *J. Chem. Phys. 102*: 6088 (1995).

178. G. C. Schatz, Quantum theory of photodetachment spectra of transition states, *J. Phys. Chem. 94*: 6157 (1990).

179. D. G. Truhlar, General discussion, *Faraday Discuss. Chem. Soc. 91*: 395 (1991).

180. E. R. Lovejoy, S. K. Kim, and C. B. Moore, Observation of transition-state vibrational thresholds in the rate of dissociation of ketene, *Science 256*: 1541 (1992).

181. W. H. Green, Jr., C. B. Moore, and W. F. Polik, Transition states and rate constants for unimolecular reactions, *Annu. Rev. Phys. Chem. 43*: 591 (1992).

182. E. R. Lovejoy and C. B. Moore, Structures in the energy dependence of the rate constant of ketene isomerization, *J. Chem. Phys. 98*: 7846 (1993).

183. S. K. Kim, E. R. Lovejoy, and C. B. Moore, Transition state vibrational level thresholds for the dissociation of triplet ketene, *J. Chem. Phys. 102*: 3202 (1995).

184. M. S. Child, Measurable consequences of a dip in the activation barrier for an adiabatic chemical reaction, *Mol. Phys. 12*: 401 (1967).

185. B. C. Garrett, D. G. Truhlar, R. S. Grev, G. C. Schatz, and R. B. Walker, Reaction probabilities, resonances, and thermal rate constants for the collinear reactions H + FH and D + FD on a low-barrier surface: Close-coupling and tunneling calculations, variational transition-state theory, and the unified statistical model, *J. Phys. Chem. 85*: 3806 (1981).

186. G. A. Brucker, S. I. Ionov, Y. Chen, and C. Wittig, Time-resolved studies of NO_2 photoinitiated unimolecular decomposition: step-like variation of $k_{uni}(E)$, *Chem. Phys. Lett. 194*: 301 (1992).

187. S. I. Ionov, G. A. Brucker, C. Jaques, Y. Chen, and C. Wittig, Probing the $NO_2 \to NO + O$ transition state via time resolved unimolecular decomposition, *J. Chem. Phys. 99*: 3420 (1993).

188. S. I. Ionov, H. F. Davis, K. Mikhaylichenko, L. Valachovic, R. A. Beaudet, and C. Wittig, The density of reactive levels in NO_2 unimolecular decomposition, *J. Chem. Phys. 101*: 4809 (1994).

189. S. J. Klippenstein and T. Radivoyevitch, A theoretical study of the dissociation of NO_2, *J. Chem. Phys. 99*: 3644 (1993).

190. H. Katagiri and S. Kato, The spin-orbit effect on potential surfaces of NO_2 photodissociation, *J. Chem. Phys. 99*: 8805 (1993).

191. Y. S. Choi, T. S. Kim, H. Petek, K. Yoshihara, and R. L. Christensen, Evidence for quantization of the transition state for *cis-trans* isomerization, *J. Chem. Phys. 100*: 9269 (1994).

192. K. Haug, D. W. Schwenke, Y. Shima, D. G. Truhlar, J. Zhang, and D. J. Kouri, $\mathcal{L}^2$ solution of the quantum mechanical reactive scattering problem. The threshold energy for D + $H_2(v = 1) \to HD + H$, *J. Phys. Chem. 90*: 6757 (1986).

193. Y. C. Zhang, J. Z. H. Zhang, D. J. Kouri, K. Haug, D. W. Schwenke, and D. G. Truhlar, Quantum mechanical calculations of vibrational population inversion in chemical reactions: Numerically exact $\mathcal{L}^2$-amplitude-density study of the H_2Br reactive system, *Phys. Rev. Lett. 60*: 2367 (1988).

194. M. Mladenovic, M. Zhao, D. G. Truhlar, D. W. Schwenke, Y. Sun, and D. J. Kouri, Effect of orbital and rotational angular momentum averaging on branching ratios of dynamical resonances in the reaction H + p-H_2 → o-H_2 + H, *Chem. Phys. Lett. 146*: 358 (1988).

195. M. Mladenovic, M. Zhao, D. G. Truhlar, D. W. Schwenke, Y. Sun, and D. J. Kouri, Converged quantum mechanical calculation of the product vibration-rotation state distribution of the H + p-H_2 reaction, *J. Phys. Chem. 92*: 7035 (1988).

196. M. Zhao, M. Mladenovic, D. G. Truhlar, D. W. Schwenke, O. Sharafeddin, Y. Sun, and D. J. Kouri, Spectroscopic analysis of transition state energy levels: Bending-rotational spectrum and lifetime analysis of H_3 quasibound states, *J. Chem. Phys. 91*: 5302 (1989).

197. M. Zhao, D. G. Truhlar, D. W. Schwenke, and D. J. Kouri, Effect of rotational excitation on state-to-state differential cross sections: D + H_2 → HD + H, *J. Phys. Chem. 94*: 7074 (1990).

198. D. G. Truhlar, D. W. Schwenke, and D. J. Kouri, Quantum dynamics of chemical reactions by converged algebraic variational calculations, *J. Phys. Chem. 94*: 7346 (1990).

199. S. L. Mielke, G. J. Tawa, D. G. Truhlar, and D. W. Schwenke, Quantum photochemistry. Accurate quantum scattering calculations for an electronically nonadiabatic reaction, *Chem. Phys. Lett. 234*: 57 (1995).

200. G. C. Schatz, Quantum reactive scattering using hyperspherical coordinates: Results for H + H_2 and Cl + HCl, *Chem. Phys. Lett. 150*: 92 (1988).

201. W. H. Miller, Recent advances in quantum mechanical reactive scattering theory, Including comparison of recent experiments with rigorous calculations of state-to-state cross sections for the H/D + H_2 → H_2/HD + H reactions, *Annu. Rev. Phys. Chem. 41*: 245 (1990).

202. J. Z. H. Zhang, D. L. Yeager, and W. H. Miller, 3D quantum scattering calculations of the reaction He + H_2^+ → HeH^+ + H for total angular momentum $J = 0$, *Chem. Phys. Lett. 173*: 489 (1990).

203. J. Z. H. Zhang and W. H. Miller, Quantum reactive scattering via the S-matrix version of the Kohn variational principle: Differential and integral cross sections for D + H_2 → HD + H, *J. Chem. Phys. 91*: 1528 (1989).

204. U. Manthe, T. Seideman, and W. H. Miller, Full-dimensional quantum mechanical calculation of the rate constant for the H_2 + OH → H_2O + H reaction, *J. Chem. Phys. 99*: 10078 (1993).

205. U. Manthe, T. Seideman, and W. H. Miller, Quantum mechanical calculations of the rate constant for the H_2 + OH → H + H_2O reaction: Full-dimensional results and comparison to reduced dimensionality models, *J. Chem. Phys. 101*: 4759 (1994).

206. J. D. Kress, Z. Bačić, G. A. Parker, and R. T. Pack, Quantum effects in the F + H_2 → .HF + H reaction. Accurate 3D calculations with a realistic potential energy surface, *Chem. Phys. Lett. 157*: 484 (1989).

207. Y. S. M. Wu, A. Kuppermann, and B. Lepetit, Theoretical calculation of experimentally observable consequences of the geometric phase on chemical reaction cross sections, *Chem. Phys. Lett. 186*: 319 (1991).

208. Y. S. M. Wu and A. Kuppermann, Prediction of the effect of the geometric phase on product rotational state distributions and integral cross sections, *Chem. Phys. Lett. 201*: 178 (1993).

209. D. Neuhauser, M. Baer, R. S. Judson, and D. J. Kouri, Time dependent three-dimensional body frame quantal wave packet treatment of the H + H_2 exchange reaction on the Liu-Siegbahn-Truhlar-Horowitz (LSTH) surface, *J. Chem. Phys. 90*: 5882 (1989).

210. D. Neuhauser, R. S. Judson, R. L. Jaffe, M. Baer, and D. J. Kouri, Total integral reactive cross sections for F + H_2 → HF + H: Comparison of converged quantum, quasiclassical trajectory and experimental results, *Chem. Phys. Lett. 176*: 546 (1991).

211. M. Gilibert and M. Baer, Exchange processes via electronic nonadiabatic transitions: An accurate three-dimensional quantum mechanical study of the $F(^2P_{1/2}, {}^2P_{3/2})$ + H_2 reactive systems, *J. Phys. Chem. 98*: 12822 (1994).

212. D. E. Manolopoulos and D. C. Clary, Quantum calculations on reactive collisions, *Annu. Rep. Prog. Chem. 86*: 95 (1989).
213. D. E. Manolopoulos and R. E. Wyatt, H + H$_2$ (0, 0) → H$_2$(v', j') + H integral cross sections on the double many body expansion potential energy surface, *J. Chem. Phys. 92*: 810 (1990).
214. M. D'Mello, D. E. Manolopoulos, and R. E. Wyatt, Quantum dynamics of the H + D$_2$ → D + HD reaction: comparison with experiment, *J. Chem. Phys. 94*: 5985 (1991).
215. J. M. Launay, Computation of cross sections for the F + H$_2$($v = 0$, $j = 0$) → FH (v', j') + H reaction by the hyperspherical method, *Theor. Chim. Acta 79*: 183 (1991).
216. J. M. Launay and S. B. Padkjaer, Quantum-dynamical study of the Cl + H$_2$ → ClH + H reaction, *Chem. Phys. Lett. 181*: 95 (1991).
217. S. E. Branchett, S. B. Padkjaer, and J. M. Launay, Quantum dynamical study of the H + HCl → H$_2$ + Cl reaction, *Chem. Phys. Lett. 208*: 523 (1993).
218. G. A. Parker, R. T. Pack, and A. Laganà, Accurate 3D quantum reactive probabilities of Li + FH, *Chem. Phys. Lett. 202*: 75 (1993).
219. A. Laganà, R. T. Pack, and G. A. Parker, Li + FH reactive cross sections from $J = 0$ accurate quantum reactivity, *J. Chem. Phys. 99*: 2269 (1993).
220. G. C. Schatz, Influence of atomic fine structure on bimolecular rate constants: The Cl(^{2}P) + HCl reaction, *J. Phys. Chem. 99*: 7522 (1995).